Horizontal wind influence on satellite aerodynamics at the edge of space

Liv Mare Toonen

Horizontal wind influence on satellite aerodynamics at the edge of Space

by

Liv Mare Toonen

to obtain the degree of Master of Science
at the Delft University of Technology,
to be defended publicly on Friday, June 4th, 2021 at 10:00am

TUDelft

Preface

What a crazy year and a half it has been working on this subject. When I started, I was completly green on the subject of space weather. If I am being honest I did not exactly know what it was, but it fascinated me. The northern lights are a perfect example of the charm of space weather and the thermosphere. These colorful displays, behind which enormous amounts of energy are hidden, can be observed by our own eyes, standing with two feet on the ground. Even though they seem relatively close, at the same time they originate from a part of the atmosphere that is still so *unknown*? This, gave a whole new meaning to 'Space Exploration' for me, much closer to home than I ever imagined.

More things were suddenly much closer to home than I could have ever imagined, due to the global pandemic, COVID-19. One month in my internship at the Royal Netherlands Meteorological Institute (KNMI), I was not allowed to go anymore to the office. Full of good hope and disbelief, I remember telling my office roommate: "see you in 2 weeks!", not knowing that from that moment on, the remaining 4 months of my internship and the 9 months of my thesis would take place at home.

It was not always easy working at home alone on a subject, and for me, like for many others, it took a while until I had the hang of it. Luckily, I had three enthusiastic, committed and inspiring supervisors who I am extremely grateful for; Jose van den IJssel, Eelco Doornbos and Christian Siemes. Jose, thank you for all the good conversations, for keeping things realistic, your critical questions, feedback and of course for the necessary laughs and support. Christian, thank you for sharing your knowledge, always being critical, but enthusiastic and for really taking the time to help me when I was completely stuck. And finally Eelco, thank you for your endless enthusiasm, ideas and knowledge during my internship and thesis. The passion and motivation for your work, is, lucky for me, contagious. Also thanks to Günther March, who has helped me get started with SPARTA.

On a daily basis, I have been extremely lucky with my roommates. From thesis discussions and good conversations with Robijn, Sjohn and Aert, to study sessions, and cups of coffee and tea with Flip and Martin. Or when I needed some relaxation or motivational beers, also Poes, Kurk and Babs were there for me. During the day, our rooms took turns in becoming general BHStudy places. In addition, I would like to thank Daisy, who loyally studied next to me every Thursday, making sure I was not looking outside the window too much and who always made me feel good about myself by letting me win with tennis over and over again. In addition, thanks to Floris for the walks, ice creams and being a sounding board. Thanks to Toesh that we could 'lose our eggs' with each once in a while and to my other friends for the support, laughs and distractions. Finally, I would like to thank my parents, grandparents, Teo, Cia and Javier for their never ending support with food, messages, drinks, nice plans or just a listening ear. And when, in the week of handing in my thesis, I became ill, my parents were there for me, like old times, taking care of me to make sure I would get better as soon as possible.

With the completion of my thesis, I am also looking back on the 7 amazing years living in Delft (with periods in Tokyo, Lanzarote and Utrecht) and all the people that have made it so great. I am looking forward to a next adventure, whatever and wherever that may be.

Liv Mare Toonen,
Delft, May 21, 2021

Abstract

The thesis presented here shines a light on the influence of horizontal wind on satellite aerodynamics in the lower thermosphere at an altitude range of 100-150 km. The lower thermosphere is characterized by a composition and dynamics driven by space weather. The neutral lower thermosphere shares its region with the electrically charged particles, called ions, of the ionosphere. Space weather in the lower thermosphere and ionosphere (LTI), can impact electrical grids on the Earth and (manned) satellite missions in Space. The more humankind depends on electrical devices and space flight, the more important it is that space weather is well understood and can be predicted. However, there are huge data gaps in the global coverage of that region and the physical processes are hard to model precisely without observation data. As a solution, a satellite mission called Daedalus, is proposed to measure the key electrodynamic processes that occur in the LTI by measuring in-situ. To do this, Daedalus has a highly eccentric orbit with a nominal perigee altitude of 140 km, with dips to 120 km altitude.

The challenge of a mission like Daedalus is that space weather influences the satellite itself as well. In addition, the high densities of the LTI induce drag on the satellite and might result in orbital decay. The focus of this thesis is to investigate the impact of the horizontal winds caused by space weather in the lower thermosphere on the aerodynamic drag a satellite like Daedalus will encounter. In order to model the aerodynamics of the satellite, assumptions are made on the mission design and shape of the vehicle. The defined standard satellite shape consists of a slender body with solar array wings and long slender booms to measure in-situ the electric field (E-field) created in the ionosphere. Variations in terms of body size, wing thickness and wing size are tested. In addition, the influence of the satellite's apogee altitude and attitude on its drag are tested.

In terms of aerodynamics, the drag in the opposite direction of the orbital velocity has most influence on the mission, because it causes orbital decay. To get an idea of the orbital decay due to the drag, the decay of the semi-major axis is integrated over one orbit. It is shown that for an elliptical orbit like the one for Daedalus, 96% of the total orbital decay is caused by the drag the satellite encounters at altitudes lower than 150 km. To obtain the drag, the complex product of the drag coefficient times the affected area, $C_D * A_{ref}$, needs to be obtained. However, at this altitude the flow is in a Transitional Flow (TF) regime between Continuous Flow (CF) regime and Free Molecular Flow (FMF) regime. There are no analytical expressions available for the aerodynamic coefficients of the satellite for the TF regime.

A method is proposed to use Stochastic PArallel Rarefied-gas Time-accurate Analyzer, SPARTA, to obtain the aerodynamic forces on the satellite geometry variations. The satellite geometries are modeled by the software tool Blender. From these aerodynamic forces the aerodynamic coefficients are obtained. The results at a perigee altitude of 120 km in the TF regime are compared to a perigee altitude of 300 km in the FMF regime. Based on the analytical expressions of the FMF regime and the drag equation, it is shown that the drag is influenced by the thermospheric parameters, like gas temperature, composition and density, and gas-surface collision parameters. The thermospheric parameters are highly variable due to space weather. The range of values for these parameters are obtained from the model NLRMSISE-00 and literature. In addition, nominal values for these parameters are defined. The impact of the variability of these thermospheric parameters on the drag coefficient and total drag are tested. It is concluded, that at 120 km altitude, $C_D * A_{ref}$ is most influenced by the variability of the density. The

value for the $C_D * A_{ref}$ can differ 25% with respect the value obtained with the nominal density at that altitude. Density often increases together with temperature, resulting in a more molecular composition. It is found that $C_D * A_{ref}$ of the standard satellite geometry can vary 7.5% from the nominal value due to the variability of temperature. The change in composition between high and low geomagnetic activity decreases the drag coefficient with only 1%. The defined standard satellite shape is proven to be more sensitive to the thermospheric condition variations due to the large frictional component of drag exerted on the relatively large wings.

With the nominal values defined for the parameters, the influence of the horizontal wind on the satellite can be modeled. The magnitude of the horizontal winds are obtained from the Horizontal Wind Model 2014 (HWM14) and in-situ data in the form of chemical tracers measurements on board of sounding rockets and accelerometer measurements on board of the Gravity field and steady-state Ocean Circulation Explorer, GOCE. Generally, the magnitude of the winds from the models are found to be lower than the wind from the in-situ data. The maximum winds from the [model,data] are [200,370] m/s around an altitude of 120 km and [500, 1080] m/s around an altitude of 300 km. It is decided to look at the impact of the maximum winds on the satellite's aerodynamic drag to get an indication of the worst-case scenario. The proposed simulation is run for multiple values within the dynamic ranges of the wind obtained from both HWM14 as the in-situ data.

The horizontal wind can be decomposed in cross-track wind and in-track wind. It was proven that the cross-track wind has a negligible influence on the satellite when the satellite is rotated such that the wings are aligned with the relative velocity. When the satellite is rolled by 90°, the worst-case cross-track wind can increase the $C_D * A_{ref}$ of the standard shape from 8.2 to 8.9 ($\pm$ 8%). The in-track wind influence on the drag coefficients was found to be negligible at the TF altitude of 120 km. The influence of the in-track wind on the drag of the standard satellite shape, on the other hand, is significant due to the change in relative velocity of the satellite with respect to the gas flow. The total drag can be increased or decreased by 6-10%, depending if the worst-case wind comes from the front or from the back respectively.

In terms of mission design, it is found that the choice of apogee altitude between 2200 km and 2700 km influences the drag insignificantly. In terms of satellite geometry it is concluded that drag could be saved by making the satellite body part longer and thinner, while keeping the same volume. This would increase the sensitivity of the cross track wind on the satellite, however, this is not significant with respect to the reduction of the drag, which is 10%. The design choices of making thicker wings increases the drag almost linearly ($\pm$ 3% per 2 cm), but it does not increase the sensitivity of the satellite with respect to wind.

The size of the wing area is found to have a significant contribution to the drag. Increasing the wing size, mainly enforces the frictional component of the drag coefficient. In addition, when the satellite wings are orientated perpendicular to the cross-track wind, the size of the wings influences the sensitivity of the satellite aerodynamics with respect the cross-track wind. Depending on the one-sided wing area within the range of [6.6, 37.9] m^2, the worst-case horizontal wind obtained from the in-situ data, results in an increase of [5.2, 11.2]% of the $C_D * A_{ref}$ of the standard satellite shape. The contribution of the booms can be assumed to be constant, because the drag coefficient of the booms does not show sensitivity with respect to the thermospheric parameters, gas-surface collision parameters nor wind.

In conclusion, the worst-case cross-track wind that can be found at 120 km altitude can increase the drag of the satellite with 5-11% depending on the wing size, when the satellite rolls 90°. In the other cases, the worst-case cross-track wind has found to have a negligible influence on the $C_D * A_{ref}$. In most cases, the cross-track wind contribution can therefore be ignored, which will simplify the mission design. In addition, the influence of the in-track wind at 120 km altitude on the $C_D * A_{ref}$ is also found to be negligible, independent of the size and thickness of the wings and the body size. The in-track wind, however, has a significant influence on the drag due to the change in relative velocity in the drag equation. Therefore, the in-track wind only has to be taken into account in the relative velocity of the drag equation for the design of a mission with a perigee altitude of 120 km.

Contents

Chapter 1

Introduction

The Northern lights are a colorful dancing display that can be witnessed at the North Pole. In the past, the indigenous tribes believed that these so-called auroras were spirits from friends and family who had passed away and who were using the moving colors and shapes in the sky to communicate with their loved ones. Through the centuries, the auroras have inspired arts, religion and science.

Nowadays, scientists are much closer to the real cause behind the auroras. Even though the scientific truth is less romantic than the truth of the indigenous tribes, it is just as fascinating. The auroras are the result of huge quantities of energy that originate from the Sun and are transmitted to particles just at the edge of Space. To release this energy, these particles move and emit light, resulting in the auroras. What makes it even more fascinating, is that the altitude region at which all these energetic processes take place is extremely hard to monitor in-situ. The density is too low for airplanes to fly or balloons to reach, but too high for satellites to stay without decaying very fast. It is therefore called the 'most undiscovered part of the atmosphere'.

Auroras are just the tip of the iceberg, when it comes to this so-called space weather. The European Space Agency (ESA) defines space weather as: "The environmental conditions in the Earth's magneto-sphere, ionosphere and thermosphere due to the Sun and the solar wind". Solar wind can be seen as a high speed stream of energized and charged particles coming from the Sun, which carry the Sun's magnetic field. The auroras are the part of space weather we can see, however, it influences our lives in many more ways. Now that we are more and more depending on electrical devices and satellite systems like GPS, this influence is increasing. For example, space weather can damage satellites in space and power grids on the surface. No wonder that we would like to be able to predict space weather.

However, this is complicated. The main energy source of space weather, the Sun, is highly variable and the Sun-Earth connection is still not well understood. Furthermore, the most important region where the complex physical interactions between space weather and Earth weather take place, has earlier been defined as the most undiscovered part of the atmosphere. Due to a lack of in-situ data, this boundary region has not been modeled properly yet. This region is vital, for understanding, modeling and predicting global space weather.

A brand new mission of ESA: the Solar Orbiter, will give a deeper understanding of the Sun-Earth relation and space weather [Müller et al., 2013]. The next step is then to understand what kind of impact space weather exactly has on the Earth. The edge of space is generally defined at an altitude of 100 km. Around this altitude, particles coming from the Sun can enter at high latitudes and interact with the upper atmosphere, which has big influence on the composition, temperature, density and dynamics of the atmosphere. A mission was proposed, called Daedalus [Sarris et al., 2019] [ESA, 2020], with the objective to explore electrodynamic processes of the Lower thermosphere and Ionosphere (LTI) by

making in-situ measurements in the region at 120 - 200 km altitude.

A mission like Daedalus will not only measure the electrodynamic processes, but will also be affected by them. As part of the Daedalus science study it is important to map, predict and quantify the effects that space weather could have on the satellite. The focus of this thesis is the influence of the neutral dynamics, with other words the wind, on a satellite flying at an altitude of 120- 150 km altitude.

This introduction will start by giving a more thorough explanation of the Sun-Earth connection. Next, the region of interest, the thermosphere will be discussed in section 1.2. Since the flow in the lower thermosphere is in a so called Transitional Flow regime, a definition is given on what this entails in section 1.3. This is followed by section 1.4, that elaborates further on why the lower thermosphere is of interest. The mission Daedalus will be introduced in section 1.5. The challenges in our understanding of the thermosphere are explained in section 1.6. Furthermore in section 1.7, past research and missions of the lower thermosphere and satellite aerodynamics are reviewed. Finally, at the end of the introduction in section 1.8 the research objective with the structure of this thesis will be given.

1.1 Sun-Earth connection

As touched upon before, the Sun has a huge influence on the lower thermosphere. In this section, the connection between the Sun and the Earth in terms of energy is briefly explained. The energy coming from the Sun reaches the Earth in two ways: radiation and solar wind.

First of all, the main contribution to the total energy that arrives at Earth is solar Ultra Violet (UV) and Extreme Ultra Violet (EUV) radiation. The level of solar radiation arriving at the Earth in these wavelengths depend on the activity on the Earth facing side of the Sun [Forbes and Garrett, 1976] [Doornbos, 2012]. The solar activity undergoes various cycles. The most important cycle is the 11-year cycle of the Sun's magnetic field. At solar minimum there are no to few so-called sunspots. Sunspots are colder spots on the surface of the Sun due to very strong local magnetic fields. Solar flares, which can release a lot of radiation, originate from these sunspots. Over a timespan of 11 years, the number of sunspots rises, which increases the solar activity, until the solar radiation reaches a maximum and then the number of sunspots reduces again. Another cycle is the 27-day cycle which is the rotation cycle of the Sun, which influences what side of the Sun is facing the Earth. Since the spreading of the sunspots is not continuous over the Sun, this can influence if active areas face the Earth or not. The radiation dislodges molecules in the thermosphere and energizes them. The energy is lost by exposing heat. This heats up the thermosphere.
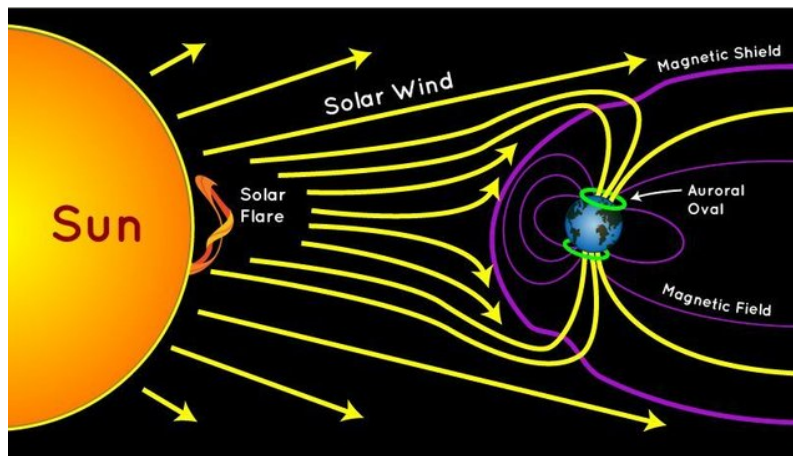

Figure 1.1: Illustration of the interaction between the solar magnetic field and the Earth magnetic field, credits: NASA.

Secondly, the energy of the Sun is transmitted due to a continuous stream of charged particles originating from the Solar magnetic field lines, called solar wind. The solar wind is not constant and exists of slower and faster moving plasma. The solar wind originates from coronal holes (regions of open magnetic field lines) and sunspots. When a solar flare occurs, large expulsions of plasma and magnetic field lines take place called a Coronal Mass Ejection. This plasma has a higher velocity than the plasma from coronal holes which results in shock waves.

The energized particles in the solar wind travel along the magnetic field lines of the Earth into the thermosphere. When the previously explained shock waves occur, the Earth's magnetosphere is disturbed, this is defined as geomagnetic activity. The geomagnetic power can be divided into two processes: Joule Heating that produces heat and particle precipitation that produces local ionization and excitation [Sinnhuber et al., 2012]. In both cases, high energy inputs in the thermosphere at high latitudes result in the heating up of that region and the movement of charged and neutral particles. In addition, some of the energy is transmitted as light, which results in the auroras that were mentioned before. An illustration of the connection of the Sun and the Earth is given in Figure 1.1.

1.2 The thermosphere

The thermosphere is one of the layers of the atmosphere surrounding the Earth. The thermosphere starts at the Mesopause, which can be seen as the 'edge of space'. The thermosphere reaches to about 500 -1000 km above our planet. This region is characterized by the large amounts of energy originating from the Sun that enters the Earth atmosphere there and the coupling with the lower atmosphere. In other words, its the region where Earth weather meets space weather. The energy coming from the Sun as explained in the previous section finds its way along the magnetic field lines into the thermosphere. Because of the absorption of EUV and UV radiation and because infra-red loss of energy is weak due to the fact that the dominant IR (infra-red) emitter at this altitude, CO 2, is dissociated, the temperature rises sharply. As explained before, the temperature of the thermosphere is greatly dependent on the solar and geomagnetic activity. The temperature in the upper thermosphere can range from 500 to 2000 degrees Celsius. The temperature can differ between night and daytime with 200 degrees.

The density of the gas in the thermosphere is extremely low. To illustrate this, at sea level, it will take a gas particle less than half the width of a human hair before colliding with another one. The fast collisions make sure that the air is well mixed. At 150 km altitude, it can take that same gas particle more than hundreds of meters before colliding with another particle. The gas particles collide so infrequently, that the gases are rather layered than well-mixed. This is also called a rarefied region.

In this extremely thin air, incoming high-energy solar photons dislodge electrons away from their atoms, resulting into a gas of negatively charged electrons and positively charged ions. This is called the Earth's Ionosphere. The ionosphere shares the same space as the electrically neutral thermosphere. Most Low Earth Orbit (LEO) satellites can be found in the LTI at altitudes higher than 250 km.

1.3 Flow regime

The region of interest of this study, at 100 - 150 km altitude, lies just above the edge of space. Below the edge of space, the particles collide and interact with each other which results in a Continuous Flow regime. Far above the edge of space the particles never collide, which is known as the Free Molecular Flow regime. In between there is a Transitional Flow regime. The flow regime describes the flow structure of a fluid or gas. Depending on the flow regime the physical processes are different. The flow regime influences the aerodynamics in three ways. First of all, it influences the composition of the particles and the density. Second of all, it influences the collisions of the particles on the surface. Thirdly, it influences the particle-particle interaction.

The region of interest of this study is signified by the change in flow regime. The two different flow

regimes can be characterized by the ratio of the number of collisions of a gas molecule with a body over the number of collisions with another gas molecule. This ratio is called the Knudsen Number (Kn) [Regan and Anandakrishnan, 1993]. It is defined by Equation 1.3.1

$$Kn = \frac{\lambda}{L} \qquad (1.3.1)$$

Where λ is the mean free path of the molecules and L is the characteristic length. λ is defined by [Regan and Anandakrishnan, 1993] as Equation 1.3.2

$$\lambda = \frac{1}{N\sigma_d^2\sqrt{2\pi}} \qquad (1.3.2)$$

Here σ_d is the collision diameter of the molecule and N is the number density. For the three different regimes that are interested in this study, the characteristics are given below Regan and Anandakrishnan [1993].

- **Free Molecular Flow (FMF):**
  A regime is characterized as FMF if *Kn >> 1*. This often happens for altitudes higher than 150 *km*. In the FMF, collisions mainly occur between gas particles and the satellite, due to the very large mean free path of the particles.

- **Continuum Flow (CF):**
  A regime can be considered CF if *Kn << 1*. This region is characterized by the continuous inter-molecular interactions. Often, the Kn is small enough under 90 *km* altitude.

- **Transitional Flow (TF):**
  The regime in between the former two regimes is the TF and is characterized by $10^{-3} \leq Kn \leq 10^{-1}$. There is no theoretical equation to express the pressure and shear on a satellite body in this regime. Often bridging functions are used that estimate the aerodynamic coefficients of a certain shape using boundary conditions in the CF and FMF.

From this it can be concluded that the altitude of the perigee of a satellite like Daedalus is in the TF regime. Whereas most satellites fly through FMF regime. The main difference between both regimes is the particle-particle interaction. In the FMF there is no interaction between the particles, whereas in the TF there is some. It can be expected that because of this, the aerodynamics of the satellite also differs. This difference between both regimes will be tested in this study by comparing the TF case with the FMF case. To do this, for both flow regimes a constant density, temperature, composition is chosen. This will be explained more elaborately in the upcoming chapters.

1.4 Why study the lower thermosphere?

The LTI, at an altitude of the 100-300 *km* altitude, has previously defined as one of the most undiscovered parts of the atmosphere. This is certainly not due to a lack of interest. On the contrary; for decades, scientists have tried to understand and investigate what physical processes are occurring in this region where Earth weather meets space weather. Now the specialized mission 'Daedalus' has been designed to investigate that area exactly. Why are we so interested in this part of space?

This section will answer that question. The importance of the lower thermosphere and its coupling with the ionosphere can be categorized in three categories, namely; its influence on applications in the Earth system, on the understanding of the complete Earth- Space system and on the design of space missions.

Applications in the Earth system

Nowadays we are highly dependent on electrical devices, electrical grids and satellite systems such as the Global Navigation Satellite System (GNSS). This means that now more than ever, space weather can

have a major influence on our day to day life.

In section 1.1, it was explained that components of the LTI interact with the incoming current along geomagnetic field lines. Solar wind interacts with the geomagnetic field lines. During certain solar events, the solar wind becomes stronger and geomagnetic storms can occur. This results in a sudden increase in ion current in the LTI. Large variations in the ionospheric currents can induce so-called Geomagnetically Induced Currents (GIC) in conductors operated on the Earth's surface. Examples of conductor systems are electrical transmission grids and underground pipelines. An example of a catastrophic event, is the collapse of the Hydro-Quebec electrical power grid in Canada during the geomagnetic storm of March 1989. About 9 million people were left without electricity [Pulkkinen et al., 2017] [Mac Manus et al., 2017].

Furthermore, space weather and waves propagating from the lower atmosphere upwards in the LTI are responsible for the forming of small-scale (in the order of tens of meters to tens of kilometers) structures in the ionospheric electron density. These changes in electron density can refract and/or diffract radio waves. This results in a rapid modification of the power and phase of radio signals, which is called ionospheric scintillation. Enforced scintillation can decrease the accuracy of GPS, Global Positioning System, measurements. Under severe conditions, scintillation can even make it impossible to determine position using GPS [Pi et al., 2017] [Xiong et al., 2016]. Ionospheric scintillation can also cause radio waves to diminish or get lost, which deteriorates radio communication [Ridley et al., 2006]. Understanding how these small-scale structures develop in the LTI, is important to be able to predict intense scintillation conditions and find a mitigation plan.

Lastly, solar events can increase the level of solar radiation that reaches the Earth system. High level of radiation can be a serious hazard for astronauts in space and satellites. For example, the degradation in the power capability of satellite solar panels is a result of high radiation levels [Hands et al., 2018]. This is a bigger problem than ever with the increasing number of small satellites, that generally lack shielding and therefore are more vulnerable to radiation. In order to protect the satellites and astronauts around the Earth from radiation it is important to be able to understand the Sun-Earth connection better to make better predictions possible.

Understanding of the complete Earth-space system

The LTI is an important part of the total energy balance of the atmosphere, because high levels of energy are inserted into the LTI and a lot of energy transport takes place. Understanding the processes in the LTI better, will give more insight in the total energy balance of the Earth and atmosphere.

In addition, thermospheric models are often used as boundary condition for other atmospheric models, like exospheric models. If the boundary conditions of a model contains errors, the model itself will contain errors as well. This means that the uncertainties in the thermosphere might influence the accuracy of the exospheric models. Therefore, more in-situ measurements in the thermopshere are essential for understanding the exosphere [Zoennchen et al., 2017].

Another point of interest is the response of the LTI to global warming. On the surface of the Earth the temperature levels are rising due to increasing CO_2 levels. However, model simulations predict that the thermosphere is cooling instead [Rishbeth and Roble, 1992] [Laštovička, 2013]. Cooling would result in decreasing density levels, which means that the thermosphere will shrink. This has influence on the complete atmosphere system, but also on everything that flies through the atmosphere, which brings us to the next point of interest.

Analysis of space missions

The decreasing density levels due to thermospheric cooling, would on the one hand mean that satellites experience less drag, which would increase the life-time of missions [Solomon et al., 2015]. On the other hand the ever increasing problem of space debris might also get worse, since it will take longer for space

debris in LEO to burn up into the atmosphere.

Not only the cooling trends are uncertain, but also the short-term heating processes of the atmosphere, like Joule heating, can not be accurately modeled yet. When the thermosphere heats up, the density and wind magnitude rises. This increases the drag that decays satellite orbits. To stay operational or to keep their accuracy requirement, maneuvers should be performed with the use of, for example, thrusters. With improved thermospheric models, these maneuvers can be planned and optimized, such that the satellite stay operational and less energy needs to be used.

Maneuvers are also important for collision avoidance. During the life-time of a LEO satellite there is chance that the satellite will encounter space debris and other satellites. Maneuver planning is therefore important to avoid catastrophic encounters. The biggest cause of uncertainty in the trajectory predictions of space debris and the satellites is due to changes in density and wind [Doornbos, 2012]. Therefore it is crucial to have improved wind and density models of the regions where they are flying. To update these models, more data is needed.

Besides the LEO satellites operational lifetime, the thermosphere is also an important factor in the end-of-life of a spacecraft. The end-of-life part of the mission of LEO satellites often involves decaying into the dense parts of the atmosphere to burn up or re-enter. Uncertainties in thermospheric densities can have a big impact on the accuracy of re-entry trajectory predictions. For big spacecraft with hazardous payloads, it is vital to be able to predict the re-entry trajectory [Klinkrad et al., 2006].

1.5 Daedalus

To obtain the data that is needed to update thermospheric models, a mission called Daedalus is proposed. Daedalus has been the direct motivation of this thesis. Daedalus was proposed for the Earth's Observation programme's 10th Earth explorer from the European Space Agency (ESA). In 2018, Daedalus had been selected as one of three candidates for the new mission. Last year Daedalus has undergone a Phase-0 feasibility study. The report that was made from this study, is often used in this thesis [ESA, 2020]. At the midterm of this thesis, it was announced that Daedalus was not selected to continue to the Phase A for further design consolidation and feasibility assessment. However, due to its unique objective, a mission like Daedalus will be likely to be designed in the future.

The objective of Daedalus is to quantify the key electrodynamic processes that determine the composition and structure of the LTI. In order to achieve this objective, Daedalus will need to be operational lower than any satellite ever before at an altitude range of 100-200 km. To make this feasible, a highly eccentric orbit has been designed with a perigee altitude of 140 km and apogee over 2000 km. With the use of propulsion, Daedalus will be able to make some perigee descents to 120 km. Since the strongest dynamic processes happen at high latitude, a large orbital inclination is preferred. Daedalus will be flying right through the LTI. To obtain all the desired measurements, the minimum mission duration is 1 year and the ideal mission duration is at least 3 years.

1.6 What are the challenges in this field?

The challenge of a mission like Daedalus is that the objective itself might also affect the satellite; The electrodynamic processes in the lower thermosphere cause a highly variable composition, temperature, density and wind. Changes in thermospheric density or wind influences the drag and torque on to Daedalus. Drag on a satellite can result in unacceptable orbit decay. To ensure that Daedalus will fulfill its mission requirements it is thus vital to have an accurate prediction of what drag and torques the satellite may encounter during its lifetime and how this influences the satellite. This thesis will answer part of that question.

In addition, models together with existing observations are often used for the instrumentation design. For the instrumentation design it is important to know the range in which the future measurements are

expected to be found and in what periods possible variations of the measured parameters take place, in order to design an instrument that is able to capture all measurements. Furthermore, the requirements for the cadence, precision and accuracy to capture these measurements can be obtained. For example, one of the measurement objectives for Daedalus is the neutral temperature of the thermosphere. From models it was found that the range of neutral temperature is 200 - 3000 K. In order to measure all variations, an instrument needs to be chosen that measures this range. In addition, the cadence is set to 1 Hz which corresponds to a spatial resolution of 16 km which is approximately the width of quiet discrete auroral arcs [ESA, 2020].

Uncertainties in the models can therefore result in under- or over- designing of the instruments and inaccuracies in the aerodynamic modeling of the satellite. Unfortunately, existing models still have big uncertainties in them. Physical models are difficult to design due to the complexity of the different processes in the thermosphere, the poor understanding of them and due to the lack of data it is difficult to validate them. The challenge for the empirical models is to obtain enough useful data to have a complete global coverage in location, solar activity and time.

In addition, even if the values for the thermospheric conditions were known and stable, only analytical expressions of the aerodynamic coefficients for the FMF exist and not for the TF. Therefore, the drag coefficients can not simply be calculated, but they need to be simulated. Simulations can be very time consuming and they are hard to validate if there is no verified observational data available.

1.7 Past research

Already a lot of research has been done in the lower part of the thermosphere and the interest seems to be increasing. However, in-situ measurements are still extremely scarce. In terms of data, one of the first important missions that was measuring the thermospheric winds from space was the WIND Imaging Interferometer (WINDII) [Shepherd, 1993]. WINDII was launched on 12 September 1991 and operated until 2003. Its objective was to measure vector winds at an altitude of 80-110 km with the use of a Doppler Michelson Interferometer. In the end, it extended its measurements until 300 km altitude [Shepherd et al., 2012]. The Ionospheric Connection Explorer Mission (ICON) has been sent last year to measure the winds in the lower thermosphere [Immel et al., 2018] and can be seen as the follow up of WINDII. ICON is orbiting in a circular orbit at 575 km altitude. It measures continuously and remotely the winds, temperatures and ion density profiles of the lower thermosphere.

From the Earth's surface the wind has been mainly observed by measuring the Doppler shifts with the use of Fabry-Perot Interferometer [Aruliah and Rees, 1995]. It is important to note, that these so-called remote sensing techniques bring all kind of errors, due to uncertainty in altitude precision and signal refraction of the atmosphere. The wind can be measured in-situ by using chemical tracers onboard of sounding rockets [Larsen et al., 2003] or by accelerometers on board of satellites. This will be further discussed in section 5.2.

In this thesis, the focus is on the influence of the horizontal wind on the satellite aerodynamics. In other words, the impact of the horizontal wind on the accelerations measured by accelerometers. A lot of research has been done on this topic in the reverse order; to obtain the wind from the accelerometer observations. The first technique to obtain the wind from satellite accelerations, was proposed by Marcos and Forbes [1985]. This was further developed by Doornbos et al. [2010]. Visser et al. [2019a] finished his PhD thesis last year where he also included the wind derived from angular accelerations of satellites. In addition, March et al. [2019] researched the influence of satellite geometry and gas-surface interaction parameters to improve the calculation of thermospheric density and wind from accelerometer observations. He performed computational simulations using Stochastic PArallel Rarefied-gas Time-accurate Analyzer (SPARTA) to model the aerodynamics of a satellite shape in a flow. This is a similar method as will be proposed in this thesis. The information of the theses of Visser et al. [2019a], March et al. [2019] and Doornbos et al. [2010] are extremely useful to understand the influence of density and wind on satellite (aero)dynamics better in terms of particle-surface interactions, drag, accelerations and

torques.

In terms of obtaining aerodynamic coefficients, Mehta et al. [2014] compared gas-surface interaction models with each other and with available analytical expressions for various thermospheric conditions. Finally, the science team of Daedalus has performed a lot of research to the feasibility and research constraints of flying Daedalus through the lower thermosphere. The phase-0 report is given in ESA [2020]. An internship has been performed prior to this thesis as part of this phase-0 report, to map the coverage of existing in-situ wind data and to see how the coverage of Daedalus could add to this. Furthermore, the wind data from GOCE and chemical tracers were compared to each other and to thermospheric wind models to find out what kind of wind a satellite like Daedalus can encounter during its lifetime. On the results of this internship will be further elaborated upon in chapter 5.

1.8   Research objective and scope

To conclude this introduction, the research objective and scope of this thesis are presented. The LTI is one of the most undiscovered parts of the atmosphere. At the same time it is an extremely important and interesting region due to the high energy inputs that arrive there from the Sun. The LTI is therefore a vital link to understand the connection with the Sun and Earth better. In addition, the understanding of this region is important for assessing the role of this region in the overall energy budget and to understand the dynamics, and chemistry of the Earth-atmosphere system. Finally, in-situ data of that region is needed for the analysis of low Earth space missions, and to predict hazards like Geomagnetic Induced Currents, high levels of radiations or ionospheric scintillation.

To obtain a global data coverage of this region, a satellite mission like Daedalus could provide the solution. The objective of Daedalus would be to perform in-situ data measurements around the altitude of 120-150 km, to map the the electrodynamics and neutral processes in that region.

The challenge of such a mission is that the objective (the dynamics and variability of the thermosphere) also influences the satellite itself. In addition, the relatively high density and wind can induce drag on the satellite. Drag in the opposite direction of the orbital velocity can slow down the spacecraft and result in orbital decay. If no extra thrust is used, orbital decay reduces the mission lifetime and can consequently endanger the scientific requirements of the mission.

Therefore, it is vital to make an estimation of the aerodynamic forces that the satellite can encounter during its lifetime in the mission design. The satellite design can be optimized in order to decrease the drag of the satellite. In addition, the propulsive system can be designed such that it can deliver enough thrust to counteract the decay due to the drag.

The equation for the drag is

$$D = \frac{1}{2}\rho V_r^2 C_D * A_{ref} \tag{1.8.1}$$

For LEO satellites the density, ρ, is often seen as the main contributor to the drag. However, the drag is also influenced by the satellite's relative velocity with respect to flow, V_r, and the drag coefficient times the affected or reference area, $C_D * A_{ref}$. The latter is effected by shape, attitude and atmospheric parameters like the wind, gas temperature, density and composition. Due to the unavailability of data, the variability of the thermosphere and the complexity of the TF regime, obtaining the drag coefficient to calculate the drag is a real challenge.

The purpose of this thesis is to shine light on this subject by providing an analysis for the following research objective:

To investigate the <mark>influence</mark> *of the* <mark>horizontal wind</mark> *and the* <mark>errors</mark> *in the horizontal wind models on* <mark>satellite</mark> <mark>aerodynamics</mark> *at an* <mark>altitude of 100 – 150 km</mark> .

This objective can be subdivided into the following research questions. Below each question, a more elaborate explanation of the research scope is given. The color coding is accordingly.

1) *What is the wind magnitude and direction that the satellite can encounter during its lifetime?*

To find the influence of the wind, the magnitude and direction of the wind that the satellite can encounter during its lifetime should be known. From ESA [2020], it was found that the range for the instrumentation of vertical wind is assumed to be $\pm$ 400 m/s and the range of horizontal wind is assumed to be $\pm$ 1500 m/s. It can therefore be concluded that the horizontal wind is of a much larger magnitude. This agrees with the statements of Visser et al. [2019a], where he explains that the vertical winds are generally in the order magnitude of 50 m/s. In addition, the wind in the direction of the orbital velocity is in the horizontal plane. Because of these arguments, it has been decided for this thesis to focus on the horizontal winds only. The wind can be obtained from models and from data.

2) *What are the errors and uncertainties in the wind models?*

Due to the unavailability of a global data coverage at low altitudes, the thermospheric models can contain large errors. A data analysis has been performed prior to this thesis to map the errors in the model by comparing it to in-situ wind data. The useful information in the scope of this thesis will be repeated. The influence of the difference between the data and models will be tested throughout the thesis.

3) *How do the thermospheric conditions in the region of 100-150 km and their variability affect the satellite's aerodynamics?*

Drag in the opposite direction of the orbital velocity is the biggest contributor to orbital decay. Due to the unavailability of analytical expressions for the TF, the most difficult parameter to obtain is the product of the drag coefficient with the reference area, $C_D * A_{ref}$, in the drag equation described above. Analytical expressions for the drag coefficients in the FMF, that will be discussed later in this thesis, show that the thermospheric temperature, wind and composition influences the drag coefficient. These parameters are interdependent with each other and with the density. The density was deemed one of the most important parameters when speaking about drag. Due to the interdependence of the wind with the other thermospheric parameters, it is important to not only understand the influence of the wind, but of the variability of the thermospheric condition parameters too.

4) *How does the wind influence the aerodynamics of a nominal satellite shape and orbital parameters?*

The wind will be decomposed into in-track wind and cross-track wind. The in-track wind only influences the magnitude of the relative velocity of the satellite, V_r, whereas the cross-track wind is mostly influences the attitude of the satellite with respect to the relative velocity, which is expected to impact $C_D * A_{ref}$.

Obtaining the relative velocity is straightforward by calculating the difference between the orbital velocity of the satellite and the velocity of the thermospheric gas particles. As mentioned before, the total $C_D * A_{ref}$ term is much harder to obtain due to the unavailability of analytical equations for the region of interest, which is in the TF regime. Because of this, in this thesis a method is proposed to use a computational model to obtain the aerodynamic forces on the satellite shape at various attitude angles, with the input of wind, thermospheric condition parameters and gas-surface collision parameters. From these aerodynamic forces the aerodynamic coefficient can be obtained. This is done for a nominal

satellite design case first.

5) *What are the influences of the design variables, like apogee altitude, attitude and satellite shape, on the aerodynamics of the satellite?*

The mission of Daedalus is still in an early design phase. Designing a satellite mission is a trade-off between many different factors, of which aerodynamics is one. The scientific requirements result in a minimum perigee altitude of 120 km and a high inclination. The apogee altitude and the attitude of the satellite during its orbit, on the other hand, are still to be determined. In addition, the exact satellite shape is not yet decided upon. The impact of general variations in the satellite shape and mission geometry on the aerodynamics in terms of drag and wind sensitivity need to be discussed.

The altitude region focus is between 100 -150 km. This is in the TF regime. The TF regime is still fairly unknown. That is why in this thesis a TF altitude case of 120 km is compared to a case in FMF at an altitude of 300 km. This altitude is better understood. It is interesting to see what the differences between the satellite aerodynamics in the regimes are.

This thesis starts by explaining the design choices that are still open for optimization, in terms of satellite shape variations in chapter 2 and in terms of orbital geometry and attitude of the satellite in chapter 3. In addition, in those chapters, the nominal satellite shape and orbit are stated. Next, to get a better understanding of the thermospheric wind and by what it is influenced in chapter 4, a theoretical background is given about the thermospheric wind. This is followed by a comparison of the Horizontal Wind Model 2014 (HWM14) and in-situ wind datasets in chapter 5. Here the errors and uncertainties in the wind models are analyzed. Now that the background of the satellite design and wind are given, the satellite (aero)dynamics are explained in chapter 6. Here it is found which thermospheric and gas-surface collision parameters influence the drag on the satellite. Consequently, these parameters and their range are discussed and a nominal value is chosen. Due to the unavailability of analytical equations for the aerodynamic coefficients for the TF, a computational method of obtaining the drag and the aerodynamic coefficients is proposed in chapter 7. The validation of this method is performed in chapter 8.

Now that the necessary background information and method are explained, the results can be obtained. The results for the sensitivity of the aerodynamic drag coefficients and the total drag to the thermospheric parameters and gas-surface collision parameters are given in chapter 9. Next the influence of the wind on the nominal satellite shape case is discussed in chapter 10. This is followed by the analysis of the impact of the mission design parameters in chapter 11 and the influence of the satellite shape variations in chapter 12 on the aerodynamics of the satellite. Finally, the conclusions of this thesis are presented that answer the questions stated earlier in this section. In addition, recommendations are given for the mission design and for future research based on findings of this project.

Part I
Mission design

Chapter 2

Satellite shapes

When designing a new satellite mission, one of the design choices is the shape of the satellite. For many satellites at higher altitudes, when designing the satellite shape, the aerodynamics do not have to be taken into account. However, for very LEO satellites, the aerodynamics start to play a role and the shape can effect the mission duration and stability. This is one of the variables that is important in this thesis and therefore needs to be tested.

It should be noted however, that the shape can not simply be optimized for the aerodynamics, since (the size and mass of) the payload of the satellite depends on the scientific purpose. Designing the satellite is always a trade-off between number and size of instruments, which are based on the mission requirements, mass of the satellite and the aerodynamics. For the design of a LEO satellite it is extremely beneficial to know what influence certain general choices on the satellite shape have on the aerodynamics of the satellite.

Daedalus will be one of the first missions that is designed to fly through the lower thermosphere. Its satellite shape is not fixed yet. In order to draw conclusions based on the influence of the satellite design on the aerodynamics, this research will use generalized shapes with variations in body and solar arrays.

The nominal model, which will be referred to in the rest of this thesis as the standard satellite shape, is explained in section 2.1 and the variations that will be tested in this thesis are explained in section 2.2. All satellite shapes used in this research are made in Blender, which is further explained in section 2.3.

2.1 Standard shape

At the start of this research there was no satellite model available for Daedalus. The size of the body of the satellite was therefore based on another scientific satellite flying through the lower thermosphere, namely the Gravity Field and Steady-State Ocean Circulation Explorer, (GOCE). Even though the satellite shape model was not available yet, a few differences with GOCE could already be pointed out. First of all, the scientific purpose of GOCE was different. One of the scientific requirements of the potential satellite Daedalus is to measure the electric field, also called the E-field, that exists within the ionospheric particles of the LTI, whereas GOCE did not have this as research objective. Therefore, the potential satellite will need booms to measure the E-field. Secondly, the orbital altitude of interest is much lower than the one for GOCE at a nominal perigee altitude of 140 km. In addition, to perform in-situ measurements in the LTI, low dips need to be performed to 120 km altitude. Due to this mission profile and the mission lifetime requirement of 3 years, electric propulsion is required with more manoeuvre capacity than was needed for GOCE. Therefore it was expected that Daedalus would need larger solar arrays to have sufficient energy available to operate the manoeuvres.

Since the body of GOCE has an approximate cross-section of 1 m^2 and a length of 5.3 m [Drinkwater et al., 2003], it was decided that these were the measurements for the body of the standard. The wings have a similar shape as the wings of GOCE, but they have a larger total area. An area per wing side of approximately 12 m^2 was chosen

During this thesis, ESA [2020] published the possible measurements of Daedalus. A body shape with a length of 4.5 m and a cross section of 0.49 m^2 has been proposed. This is smaller volume shape than assumed above. However, it is still a preliminary design as well, made by the science team of Daedalus. Therefore, the standard satellite shape is kept the same. Later on, the influence of this assumption is being tested by changing the measurements of the satellite as more thoroughly explained in subsection 2.2.1. From ESA [2020], it was found that it is expected that Daedalus would need a power generating area of approximately 15-23 m^2. The power generating area of the satellite is approximately twice the one-sided wing area. The wings of the standard satellite shape have a top area of 23.7 m^2. Due to structural parts, this area will not be completely used for power generation. This means that the wing area assumption for the standard satellite shape approximately corresponds to the upper boundary of the wing size estimation of ESA [2020]. Just as with the satellite body, the influence of larger or smaller wings is tested. The variations of the wings are explained in subsection 2.2.2. The size of the booms was based on [Turse et al., 2016] and the length of the booms agrees with ESA [2020].

The standard shape of the satellite consists of the following parts and measurements:

- **Body:**
  Length: 5.3 m, height: 1 m, width: 1 m, volume = 5.3 m^3

- **Boom (x6):**
  Length: 4 m, height: 0.05 m, width: 0.05 m

- **Wing like solar panel (x2):**
  Area: 11.85 m^2, span: 2.5 m, thickness : 0.02 m

The shape is given in Figure 2.1 and Figure 2.2. It should be noted that the satellite shape only consists of boxes. The reason for this is that the aerodynamics of a satellite model will be tested in an aerodynamic model. More about this can be read in chapter 7. Before it is inserted into the model, the shape is divided up into triangles. The more triangles the longer the computation time is. Round shapes introduce many more triangles than straight shapes. To minimize the computation time it is therefore assumed that the satellite is made out of boxes. This is a valid assumption, because at low altitudes a diffusive reflection of the particles can be assumed, as will be explained more thoroughly in chapter 6.
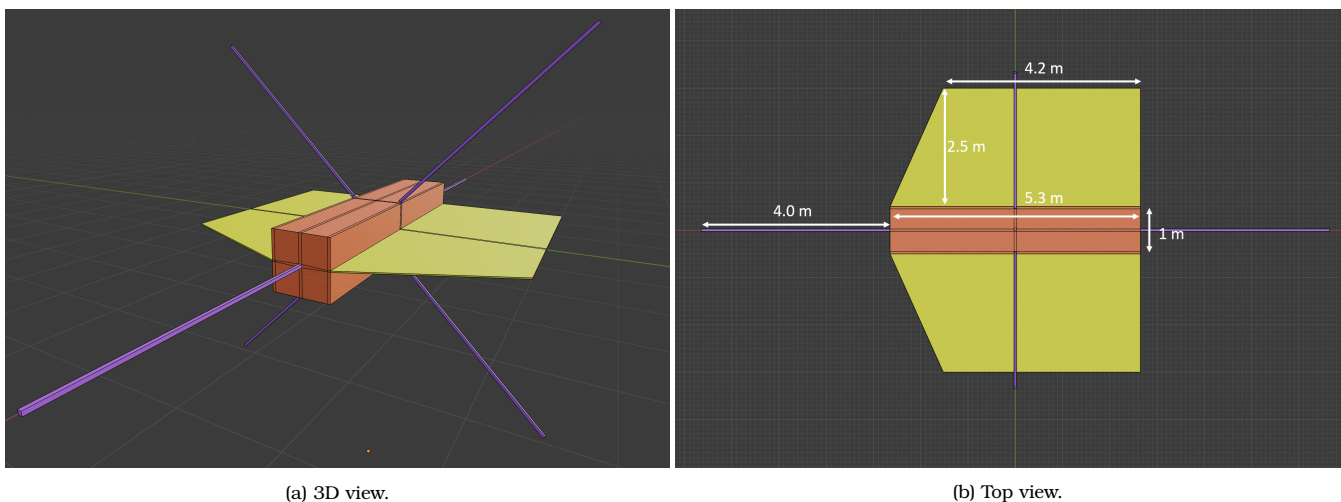

(a) 3D view.

(b) Top view.

Figure 2.1: Standard satellite shape configuration made in Blender with measurements.

(a) Front view in negative x-direction   (b) Side view in negative y-direction.
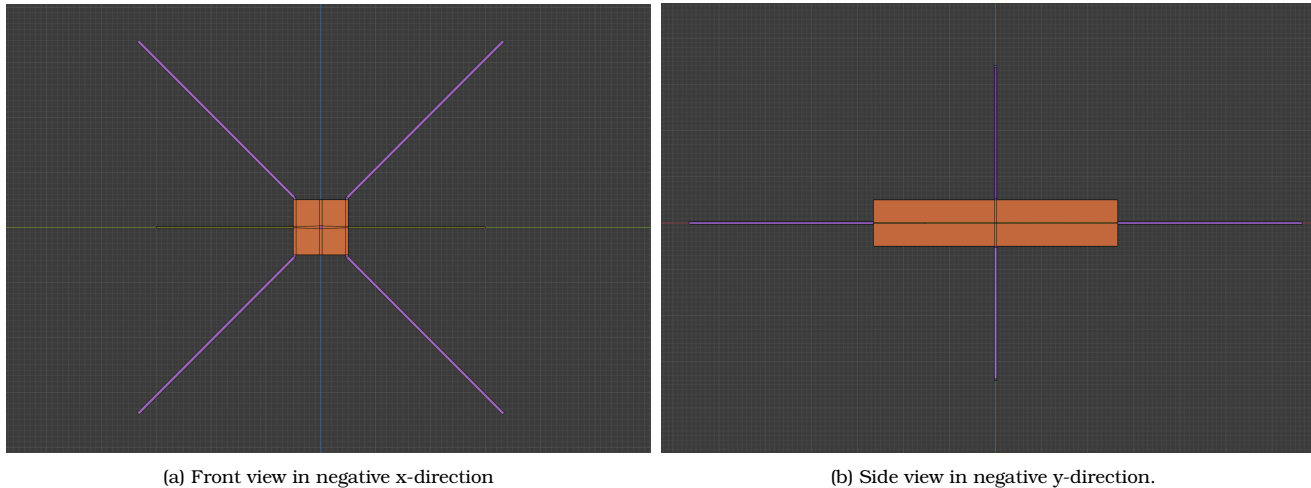
Figure 2.2: Front view and side view of standard satellite shape made in Blender.

2.2 Satellite shape variations

The influence of the geometry of the satellite on the drag and the wind sensitivity can be tested by varying the measurements of the different satellite parts one parameter at the time. In this section the variations of the body and the wings are discussed.

2.2.1 Body variations

To carry the necessary payload on board of the satellite a certain volume is needed. This volume can be obtained by either having a long and slender body or a smaller but thicker body. The influence of this choice will be tested by testing two more test cases apart from the standard satellite shape described above. The volume will stay equal to $5.3\ m^3$ in all cases. One way to do this is by making the satellite twice as long and twice as thin as illustrated in Figure 2.3a, defined as the slender body. Another possibility is to make the standard shape twice as thick and twice as short, defined as the compact body. This shape is shown in Figure 2.3b. Finally these two body variations and the body of the standard satellite shape itself are compared to the newly proposed body from ESA [2020], which has a different volume. The results for the aerodynamics of the various bodies will be given in chapter 12.

2.2.2 Solar panel variations

The area of the solar panels depends on the amount of energy that the satellite needs for propulsion and the instruments. Designing the area of the satellite's solar panels is a trade-off between the energy it supplies, the weight and aerodynamic drag that it induces. That is why it is interesting to quantify the influence of the size of the solar panels on the drag of a satellite and its sensitivity to wind. To change the area of the solar panel wing it has been chosen to change the span width. Four different wing spans are chosen: 0.7, 1.3, 1.9, 2.5 and 4 m, which result in the effective energy producing wing area, which is the area of both wings of either the top or the bottom of 6.6, 12.3, 18.0, 23.7 and 37.9 m^2. An example of the satellite with the minimum and maximum span width is shown in Figure 2.4a and Figure 2.4b respectively.
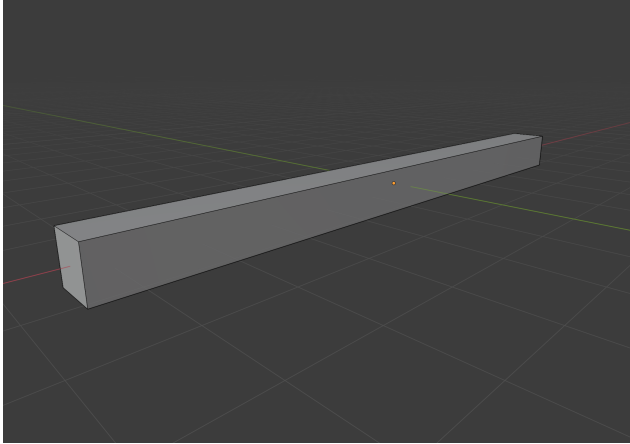
(a) Slender body: satellite body with twice the length (10.6 m) and half the cross section (0.5 m^2) of the standard satellite shape.
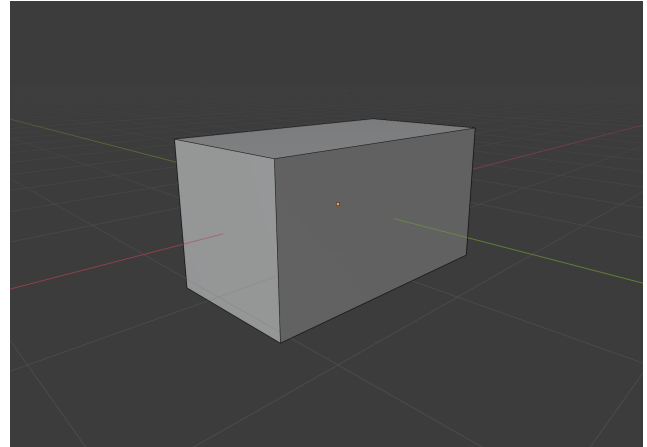
(b) Compact body: satellite body with half the length (2.65 m) and twice the cross section (2 m^2) of the standard satellite shape.

Figure 2.3: Body size variations made in Blender.
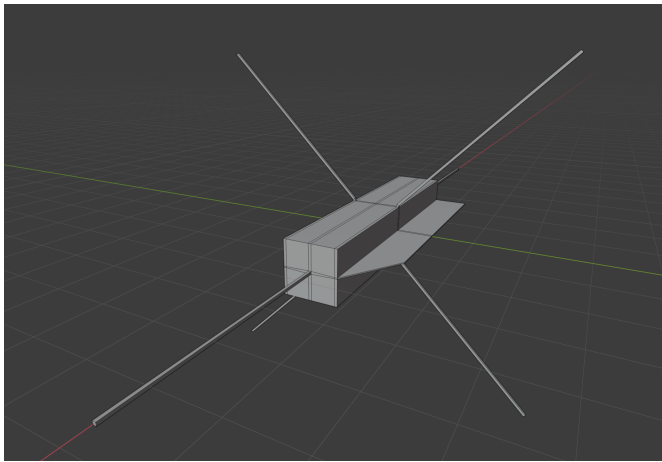
(a) Wingspan = 0.7 m and area = 6.6 m^2.
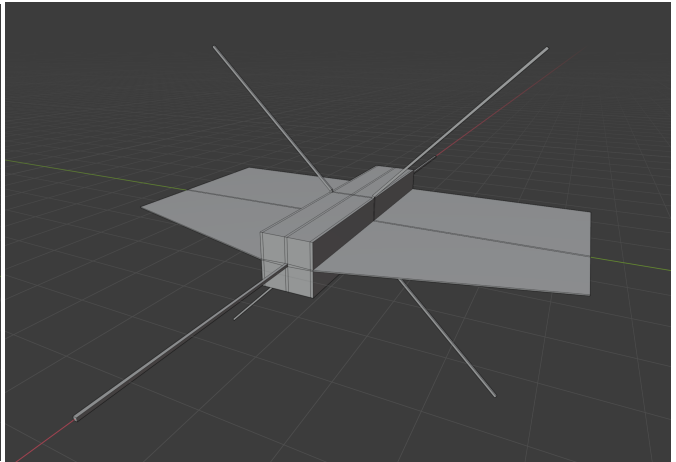
(b) Wingspan = 4 m and area = 37.9 m^2.

Figure 2.4: Wing size variations made in Blender.

Another property to describe the shape of the solar panel wings is the thickness. The choice of thickness depends on the type of solar panels and the rigidity that is needed for the panels. At extremely high altitudes, solar panels can be extremely thin (in the orders of millimeters). However since this satellite will fly through higher densities, it can be expected that larger moments and forces will be exerted upon the solar panels. Because of this more rigid and thicker panels can be expected. During the design process it is useful to see the direct influence of choosing thicker wings and if this design choice makes the satellite more or less subjective to wind and how much. To test this, four thickness variations are chosen: 0.01 m, 0.02 m, 0.04 m and 0.06 m. To illustrate, in Figure 2.5a and Figure 2.5b, the satellite models with the thinnest and thickest wings are shown. The results of the wing variations are given in chapter 12.

(a) Thickness = 0.01 m.　　　　　　　　　　　　　　(b) Thickness = 0.06 m.
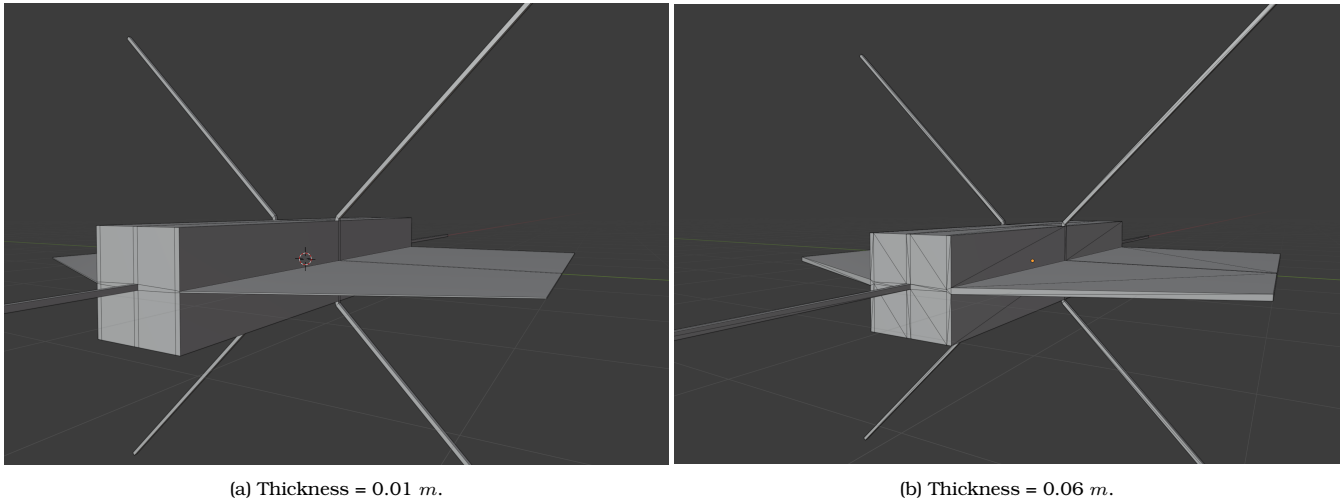
Figure 2.5: Thinnest and thickest solar wing variation made in Blender.

2.2.3 Boom measurements

The booms are instruments needed to fulfill the scientific requirements of measuring the E-field. The booms have a specific size and should be installed in such a way that they can measure in all directions. Therefore, there are not many variations possible. There are a few configuration possibilities of where to locate the booms on the satellite. However, due to the fixed size and direction of the booms and taking into account that the boom area is much smaller than the areas of other satellite parts, it is expected that the influence of the location is small. Especially with respect to the variations possible in the wings and body shape. It has therefore been chosen to keep the boom configuration constant and only examine the influence of booms for the standard case as described above.

2.3 Blender

All satellite shape variations as described above are modeled with Blender. Blender is an open-source 3D modeling tool that is, among other things, often used for 3D printing. Due to the popularity of Blender there are many tutorials to be found online and it is therefore easy to learn. Furthermore, it is possible to export the shape in an stl file. From a stl file the surface model file of the satellite can be obtained, which is needed as input in the aerodynamic modeling part. This is why it has been chosen to use Blender to model the satellite shapes.

It is not only possible to make the shapes with Blender, but also to assign certain materials to the shape. How the material influences the aerodynamics of a satellite, due to the properties that interact with the surrounding molecules, is out of the scope of this research. The material property function of Blender is used to assign a color to all different parts of the satellite: body, wings and booms. As a result, every triangle has a label describing to which part of the satellite it belongs. In this way, the contribution of all separate parts to the total aerodynamics can be investigated. Furthermore, in this thesis, the color coding of the satellite parts will be kept constant, such that the body is dark orange, the wings are yellow, the booms are purple and when speaking about the total shape, the color blue is used. When multiple parts of the body are plotted together in a graph, this color coding will also be used for the lines representing the respective parts.

Chapter 3

Orbit design

Next to the shape of the satellite, one of the design variables is the orbit of the satellite and the attitude during the orbit. Part of the orbit design results directly from scientific requirements. The most important mission requirements flowing from the scientific requirements for this research are the perigee altitude at an altitude of 120-140 km, the mission lifetime of three years and the need for a global coverage.

In addition, the satellite is expected to obtain enough solar energy to make the dips and perform orbit corrections. With these requirements the rest of the orbit can be designed. The orbit geometry is discussed in section 3.1. The attitude variation needed to obtain enough solar energy is discussed in section 3.2.

3.1 Orbit geometry

The orbit geometry of a mission needs to be optimized in order to fulfill the scientific mission requirements within a certain budget. In the case of a satellite like Daedalus, the science objective is to map the structure and physical processes happening in the LTI by performing in-situ measurements. Therefore, the satellite needs to fly through the lowest part of the thermosphere with a global coverage. To achieve this, a highly eccentric orbit is required at a near-polar inclination. A sketch is given of an eccentric orbit and its orbital parameters in Figure 3.1.
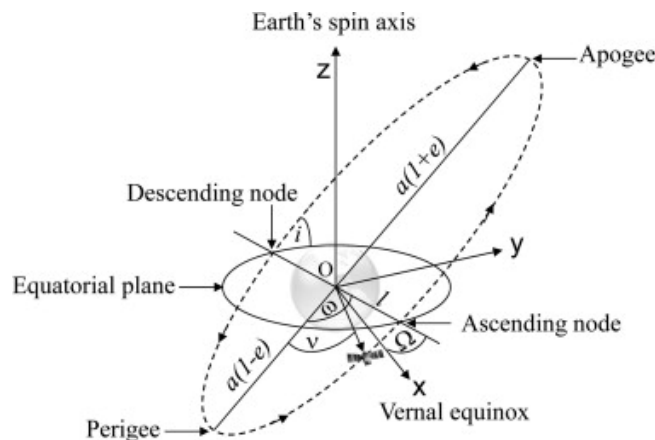

Figure 3.1: Eccentric orbit including orbital parameters, credits: Trichtchenko et al. [2014].

19

The velocity of the satellite in an eccentric orbit can be calculated by Equation 3.1.1, which is referred to the "vis-viva" equation by Newton [Wakker, 2015]. This equation is based on a two-body problem in an inertial reference frame, in which only the acceleration due to the gravitational force is taken into account.

$$V = \sqrt{\mu \left(\frac{2}{r} - \frac{1}{a} \right)} \qquad (3.1.1)$$

Equation 3.1.1 describes the velocity, V, of satellite at a distance, r, from the center of a celestial body following an orbit with a semi-major axis, a. μ is the gravitational parameter, which is obtained by multiplying the gravitational constant (G) and the mass (M_{Earth}) of the celestial body, in this case Earth. The semi-major axis (a) can be calculated by Equation 3.1.2.

$$a = \frac{r_p + r_a}{2} \qquad (3.1.2)$$

r_a is the distance of the apogee and r_p is the distance of the perigee to the center of the celestial body. The perigee of an orbit is the point at which the satellite is closest to Earth. For Daedalus this will be at a nominal altitude of 140 km with thrusted dips to 120 km altitude to fulfill its scientific requirements [ESA, 2020]. From Equation 3.1.1 it can be concluded that the velocity required to have such a low perigee altitude depends on the semi-major axis, which depends on the apogee altitude. The closer the apogee for a given perigee, the less velocity is required.

In ESA [2020], two apogee altitude cases are proposed. One with an apogee altitude of 2200 km and one with an apogee altitude of 2700 km. From Equation 3.1.1, it can be found that a satellite with a larger semi-major axis, and thus a higher apogee, has a higher velocity in the perigee. A higher velocity would mean that the satellite is less time in the perigee and therefore has less time to make observations. On the other hand, a larger semi-major axis, would mean that the satellite can loose more altitude before it decays and therefore the lifetime of the mission is prolonged. These trade-offs that should be performed in the mission design in terms of fulfilling the scientific requirements. In terms of aerodynamics, a higher velocity at the perigee induces more drag or lift. To test the worst case scenario, the case with the highest apogee altitude is chosen for the nominal run of this thesis. The other case is tested and the result is given in section 11.1.

3.2 Satellite attitude

In the previous chapter, various satellite geometries have been described to test the influence of certain satellite model design choices on its aerodynamics. However, not only the geometry is important, but also the attitude of the geometry with respect to the flow. For example, consider a flat plate. If the flat plate is faced perpendicular to the flow, like in the left figure of Figure 3.2, there is only a drag coefficient and no lift coefficient. However when the flat plates rotates by an angle, like in the right figure, the pressure which is performed on the shape works both in the drag and in the lift direction. This works similar for the satellite.
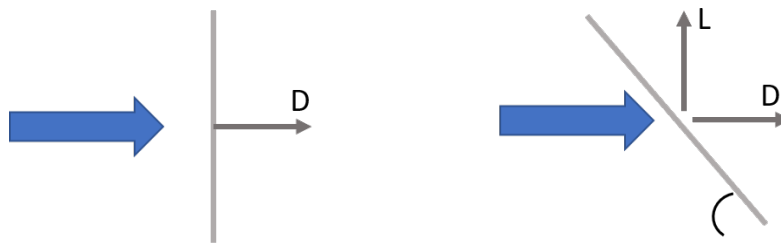
Figure 3.2: Drag and lift on a flat plate.

The angles used in this thesis to describe the attitude of the satellite with respect to the flow are the

angle of attack (α) and the side-slip angle (β). Furthermore the satellite can roll around its x-axis in order to position its solar array wings with respect to the Sun. By rotating itself, the satellite will also change the attitude angles with respect to the flow of thermospheric gas particles. To illustrate this, the three views from the axis system including the satellite are given in Figure 3.3. The aerodynamic reference frame is compared with the satellite body frame.

(a) X-Y frames with side-slip angle, β. Roll angle= $0°$

(b) X-Z frames with angle of attack, α.

(c) Y-Z frames with roll angle.
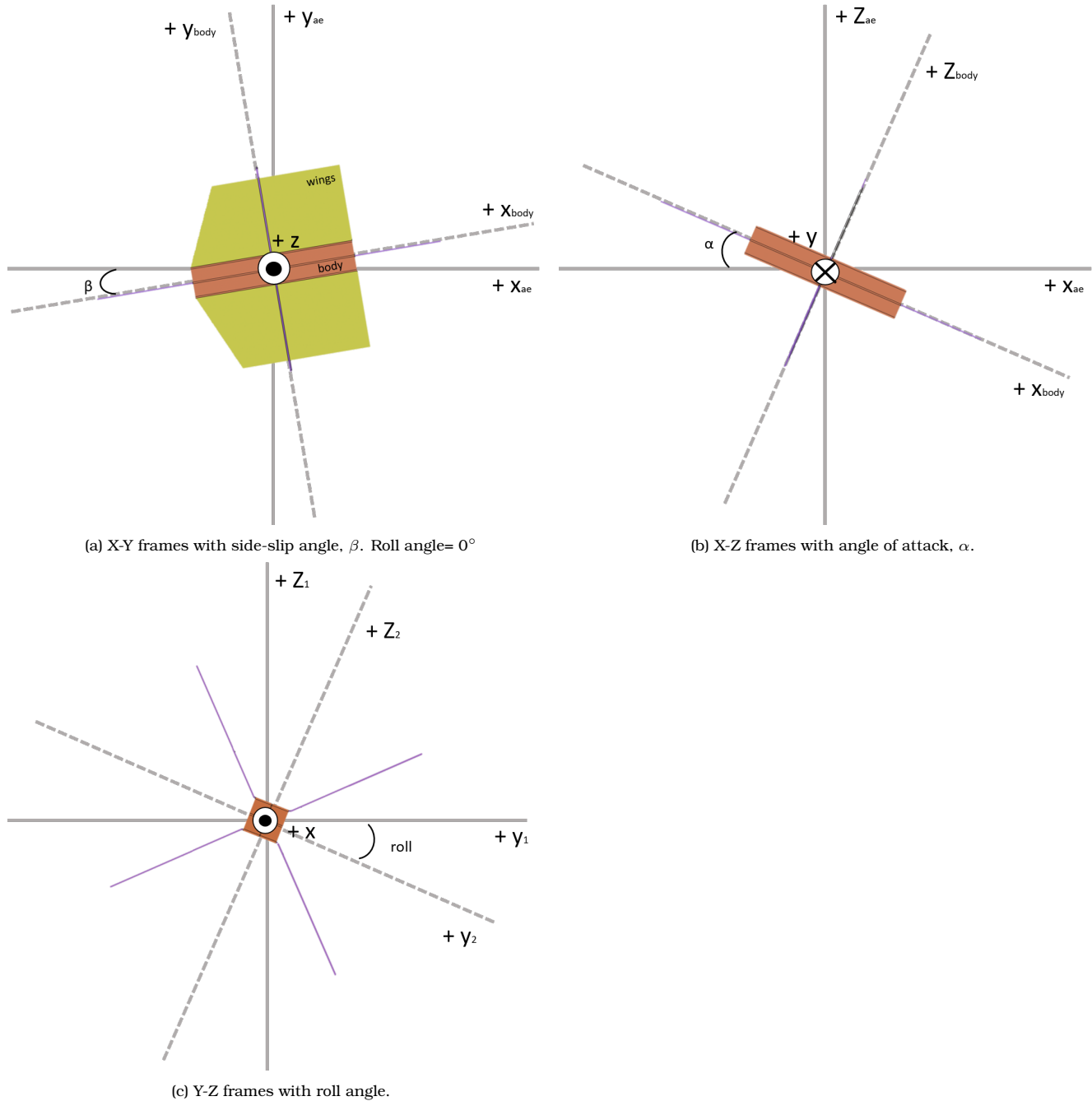
Figure 3.3: Aerodynamic reference frame and satellite body frame with attitude angles.

Throughout most of this thesis, a perfect attitude control is assumed, which means that the x-axis of the satellite body frame is always pointing exactly in the direction opposite of the orbital velocity.

It is therefore assumed that the angle of attack and the side-slip angle are only generated due to the movement of the atmosphere with respect to the satellite, also known as the wind. Since in this thesis the focus is on horizontal wind only, only the influence of the variation of the side-slip angle is examined. This is more thoroughly explained in chapter 10.

However, in reality, it would be possible for the satellite to have a few degrees of variation in the angle of attack as well, due to perturbations on the satellite or vertical wind. Therefore, the side-slip angle is examined when investigating the influence of the wind and the small perturbations in angle of attack are tested in section 11.2.

For the nominal satellite attitude of roll = 0°, it is assumed that the wings of the satellite are parallel to the X-Y frame described above. However, to obtain enough solar energy it is expected that the satellite can roll around its x-axis in order to optimize the energy obtained from the Sun. It should be noted that when the satellite is rolled 90°, the cross-track wind suddenly affects a bigger area, due to the relatively large wings of the standard satellite shape. It can therefore be expected that when the density is high, the roll rotation around the x-axis can have a huge influence on the drag that the satellite encounters. In this thesis, the impact of the maximum roll angle is tested and quantified such that an estimation can be made on how much drag can be saved by rolling the satellite to 0°, when density is high. When the wind is coming directly from the front, for $\beta = 0°$ and $\alpha = 0°$, the frontal area stays the same when roll = 90°. Consequently the influence of the roll angle only needs to be tested when there is also a side-slip angle or angle of attack induced.

Part II
Wind data analysis

Chapter 4

Thermospheric wind

One of the important factors that influences the aerodynamics of a body is the wind. At the surface of the Earth, the wind feels as a stream of air exerting a certain force on the people and objects it passes. In space, the density of the 'air' is much lower, therefore the wind works slightly differently. The wind is rather a motion of individual particles hitting a surface, which exerts a force on that surface.

Now that the possibilities for the geometry and orbit design are explained in the previous part, it is time to understand what the thermospheric wind is, where it comes from and how it acts. The conservation equations, discussed in section 4.1, are the basis of the general dynamics in the thermosphere. In addition, the magnitude and direction of the wind are influenced by the thermospheric conditions. In section 4.2, the measurable parameters of the thermospheric conditions, that influence the thermospheric wind are briefly discussed and an explanation is given for the motion of the wind for different thermospheric conditions. For a more thorough explanation, the reader can refer to the literature study belonging to this thesis [Toonen, 2020b]. Finally, to illustrate the dynamics of the thermosphere, a few cases are plotted for various thermospheric conditions in section 4.3.

4.1 Conservation equations

The basics of the thermospheric wind can be explained by the principles of conservation of mass, conservation of energy and conservation of momentum. The conservation of mass principle states that the mass of an object or a closed system remains the same, independent of how the constituents react with one another or rearrange. This is important to understand when constituents of the thermosphere react with one another or dissipate. However, since the thermosphere itself is not a closed system but reacts with the lower atmosphere and the exosphere, it does not mean that the mass in the thermosphere stays constant.

The conservation of energy principle states that all energy within a closed system of interacting objects or particles stays constant. This means that the energy is either conserved or transferred into a different energy form. For example, radiation coming from the Sun is absorbed by the thermosphere by exciting molecules. The excited molecule has a higher energy level than normal and can lose its energy in different ways: by transforming it to kinetic energy, by colliding with other molecules and by emitting heat and light. If an excited molecule collides with another molecule, the excited molecule looses some of its energy, while the other molecule gains energy. This results in a motion of the particles.

Another important fundamental concept of physics is the conservation of momentum. Momentum is the mass of an object multiplied by the velocity of an object. The conservation of momentum states, just like the other two conservation principles, that the momentum in a closed system is neither created nor destroyed. It should be noted that, unlike mass and energy, momentum is a vector quantity, which

makes the direction at which the momentum change takes place is important. The horizontal motion can be partly described by the conservation of momentum.

The conservation of momentum in the *lower atmosphere* takes into account the acceleration, non-linear advection terms, the pressure gradient, the Coriolis term and the viscosity effect. This is not yet complete, but the other momentum forces are much smaller and are often neglected. The biggest contribution to the momentum are the pressure gradient and the Coriolis force. The balance between the Coriolis force and the pressure gradient results in a flow, along isobars. Along isobars means that the flow is in the direction of the constant pressure lines.

In the thermosphere the momentum equation looks different. A simplified version of the horizontal momentum equation is given in Equation 4.1.1

$$\frac{\delta \bar{U}}{\delta t} + 2\bar{\Omega} \times \bar{U} = -\frac{1}{\rho}\bar{\nabla}P - v_{ni}\bar{U} + \frac{\mu}{\rho}\frac{\delta^2 \bar{U}}{\rho z^2} \qquad (4.1.1)$$

Here $\bar{U}$ is the horizontal wind vector, $\bar{\Omega}$ is the Earth's angular velocity, P is pressure, v_{ni} is the neutral-ion collision, or ion drag, frequency for momentum transfer, z is altitude and μ is the coefficient of molecular viscosity, ρ is density and t is time [Forbes, 2007]. Which of these momentum contributors has the biggest influence, depends on the altitude and on the solar activity.

Unlike in the lower atmosphere, the neutral-ion collision (ion drag force) term in Equation 4.1.1 is significantly higher than the Coriolis term [Forbes, 2007]. Consequently, in the thermosphere the pressure gradient and the ion-neutral collision terms have the greatest influence. This results in a cross-isobaric flow. This means that wind flows from the day-side with higher density and temperatures to the night-side with lower density. This flow occurs typical at altitudes higher than 150 km [Forbes, 2007]. In these kind of flows, on the day-side the magnitude of the wind speed is less than on the night side of Earth due to higher density of electrons and hence more ion drag.

It should be noted, that in the altitude range of approximately 100 km -150 km, the ion drag force is not so large yet. The pressure gradient and ion drag term are of a similar magnitude as the Coriolis force. This means, that without tidal forcing, the lower thermosphere appears to be in approximate gradient wind balance [Jones et al., 2019].

4.2 Fundamentals of the thermospheric wind

A division can be made between geomagnetic quiet time conditions and geomagnetic storm conditions. In conclusion of the previous section, the wind in the thermosphere (above 150 km) flows in a cross-isobaric flow. In general this means that the wind flows from a region with high pressure to a region with low pressure. There are multiple factors that influence a high or low pressure region.

When the geomagnetic activity is low, the main contributor to the high and low pressure areas, and therefore the thermospheric dynamics, is the solar radiation. From Marshall and Plumb [2008], page 24, it was found that the atoms and molecules (atomic Oxygen, molecular Nitrogen and atomic Nitrogen) in the thermosphere absorb UV and EUV radiation. Basically this means that the energy from the radiation excites, dissociates and ionizes the atoms and molecules present. The components become energized. To release this energy, heat is exerted and the thermosphere is heated up. The left-over energy is converted into kinetic energy of the reaction products [Doornbos, 2012], or is radiated back into space [Solomon et al., 2015].

Due to the the high temperatures and low pressure, the ideal gas law can be used to express the relation between temperature, pressure, number density and composition [Jacobson, 2005]. The ideal gas law is described by Equation 4.2.1.

$$pV = nR_{gas}T \qquad (4.2.1)$$

Here, p is the pressure, V is the volume, n is the number of molecules, T the temperature, R_{gas} is the universal gas constant, which equals 8.34472 $JK^{-1}mol^{-1}$.

When the temperature rises, due to heat exerted by the energized particles, the pressure rises. Since the solar radiation is only absorbed by the side of the thermosphere facing the Sun, the thermopshere is heated unevenly. This means that the wind generally flows from the day-summer side to the night-winter side. This can be expressed in Local Solar Time (LST), Day Of Year (DOY) and latitude.

Furthermore, even though the influence is much smaller, the dynamics of the thermosphere are also influenced by the dynamics of the lower atmosphere. In the troposphere, stratosphere and lower mesosphere, solar radiation is absorbed by water (H_2O) and ozone (O_3) molecules. This also creates locations of warm air. The warm air rises and tides are created. These so-called thermal migrating tides mostly propagate to an altitude of approximately 120 km-150 km [Forbes et al., 1993]. There are also non-migrating tides. These are tides that originate from a fixed location on the Earth and then propagate and grow upwards. A source for these tides could be for example, the latent heat that is released around tropical forests. Non-migrating does not mean that they do not move, it means that they do not move at the same speed as the Sun over the surface [Forbes et al., 2003]. The tides carry high density air up into the lower thermopsphere.

Finally, gravity waves can influence the dynamics of the lower thermosphere. The concept will not be explained here, but the interested reader can turn to page 24-25 of Toonen [2020b] or read about the parcel model explained in Cai et al. [2017]. The waves and tides generate new momentum in the lower thermosphere that accelerate the flow in the direction of the tide.

From section 1.1, it is known that the Sun does not only influence the thermosphere by its radiation, but also by the solar wind that can introduce geomagnetic storms. Geomagnetic storms have a big effect on the general circulation of the thermosphere. The solar wind interacts with the magnetic field lines of the Earth. Through the magnetic field cusps at high latitude, ionized and energized particles are carried along the conducting magnetic field lines into the thermosphere. The flow through the cusps is enhanced due to the increase in conductivity in this area. This increases Joule Heating, which results in a rise of temperature and density in the area [Forbes, 2007].

Furthermore, the energized particles react with the neutral gas of the thermopsphere due to ion-neutral collisions which puts the neutral thermosphere into motion. Now, the particles flow with a big velocity from high to low latitudes. This circulation system interacts with the global day-summer to night-winter circulation. Both processes can enhance or diminish each other. During a large storm, the magnitude of the neutral wind resulting exceeds the magnitude of the quiet-time circulation wind. Depending on the strength of the storm, the disturbance in the general thermospheric circulation can reach also to lower latitudes.

In conclusion, the wind is influenced by latitude, LST, DOY, altitude and geomagnetic activity, which is measured in this thesis with the ap-index [Fraser-Smith, 1972]. The horizontal wind can be decomposed in zonal and meridional direction. The positive zonal direction is the wind component along latitudinal parallel lines from West to East. The meridional component of the wind is positive if it blows from the South to the North along the local meridian.

4.3 Horizontal wind field examples

To get a deeper understanding of what is explained in the previous section a few horizontal and vertical wind fields are plotted by using the Horizontal Wind Model 2014 (HWM14) [Drob et al., 2015] at different altitudes and moments in time to illustrate the circulations. Often the term equinox is used. The equinox is the date at which the Sun crosses the celestial equator. This happens twice per year; once in March and once in September. The solstice is the moment that the Sun reaches its most Northern or Southern latitude.

In the background of the horizontal wind fields the zonal wind is plotted in color. In front, arrows are plotted that show the magnitude and direction of the total horizontal wind.

First of all, the change in the horizontal wind structure with increasing altitude with respect to latitude and LST is investigated. The variation of the horizontal wind field with respect to altitude is shown in Figure 4.1. In this figure, five different altitudes are plotted for low geomagnetic activity and around March equinox.

From literature, it is known that under $100\ km$, due to to the high density the pressure gradient and the Coriolis force have the biggest contribution in the conservation of momentum equation. The balance between the Coriolis force and the pressure gradient results in a flow along isobars. This can be seen in the first image on the upper left of Figure 4.1. Even the Coriolis effect can still be observed.

When moving up, the density drops and the number of ions increases. This induces neutral-ion collisions rise. The so-called ion drag force overcomes the Coriolis force and pressure gradient. This results for altitudes higher than $200\ km$ in an cross-isobaric flow. This means that the flow goes from summer-day-time to winter-night-time. This can be seen in the two plots on the bottom, where the flow goes from right (late afternoon) to left (early morning). Furthermore it should be noted, that above $200\ km$ the horizontal wind structure changes less with altitude. In between, there is a so-called balance between across and along isobars and that results in the structures as seen in Figure 4.1.
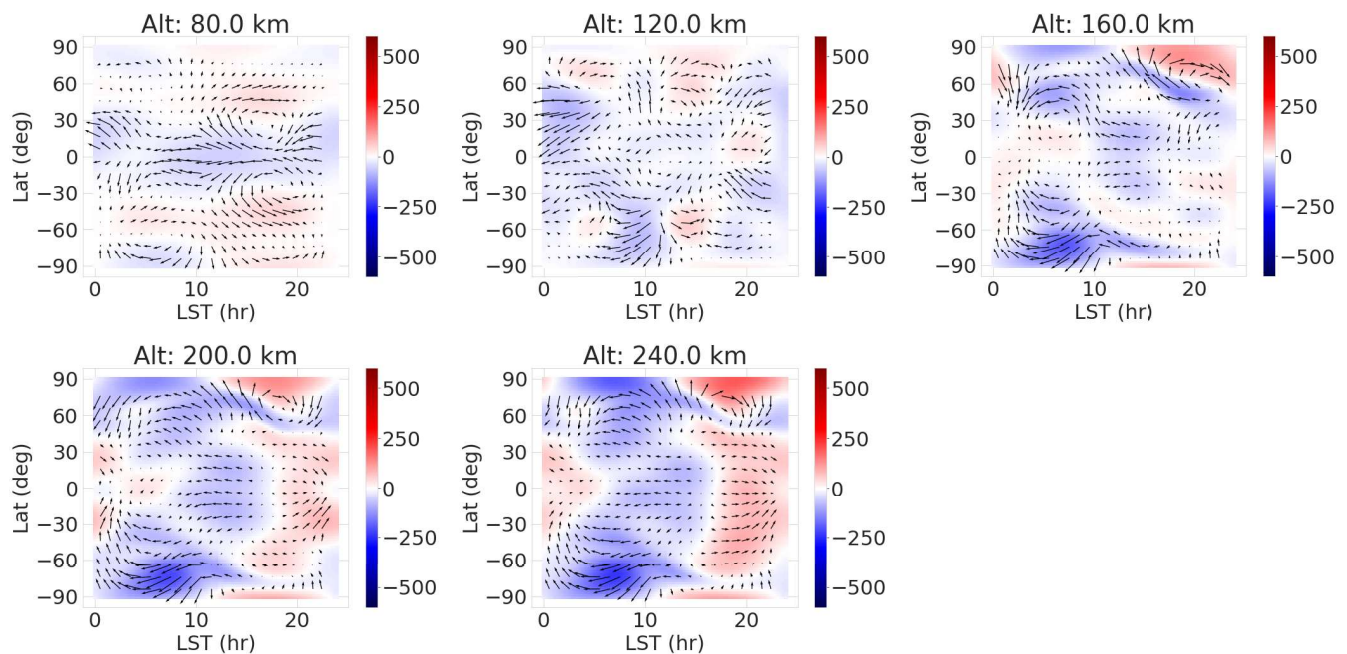
Figure 4.1: Horizontal wind variation with altitude generated by HWM14, at March equinox with low geomagnetic activity.

Secondly, the seasonal variations of the wind field are of interest. The seasonal variations at $100\ km$ and $200\ km$ altitude are visible in Figure 4.2 and Figure 4.3 respectively. As mentioned before, at $200\ km$ the neutral particles move following a cross-isobaric flow. This can be observed when looking at Figure 4.3. At June solstice, it is summer in the Northern Hemisphere. The wind flows from high pressure (afternoon in the North) to low pressure (early morning in the South). During the December solstice the wind flows from the South to the North. In addition, the magnitude of the wind is found to be larger at higher altitudes.
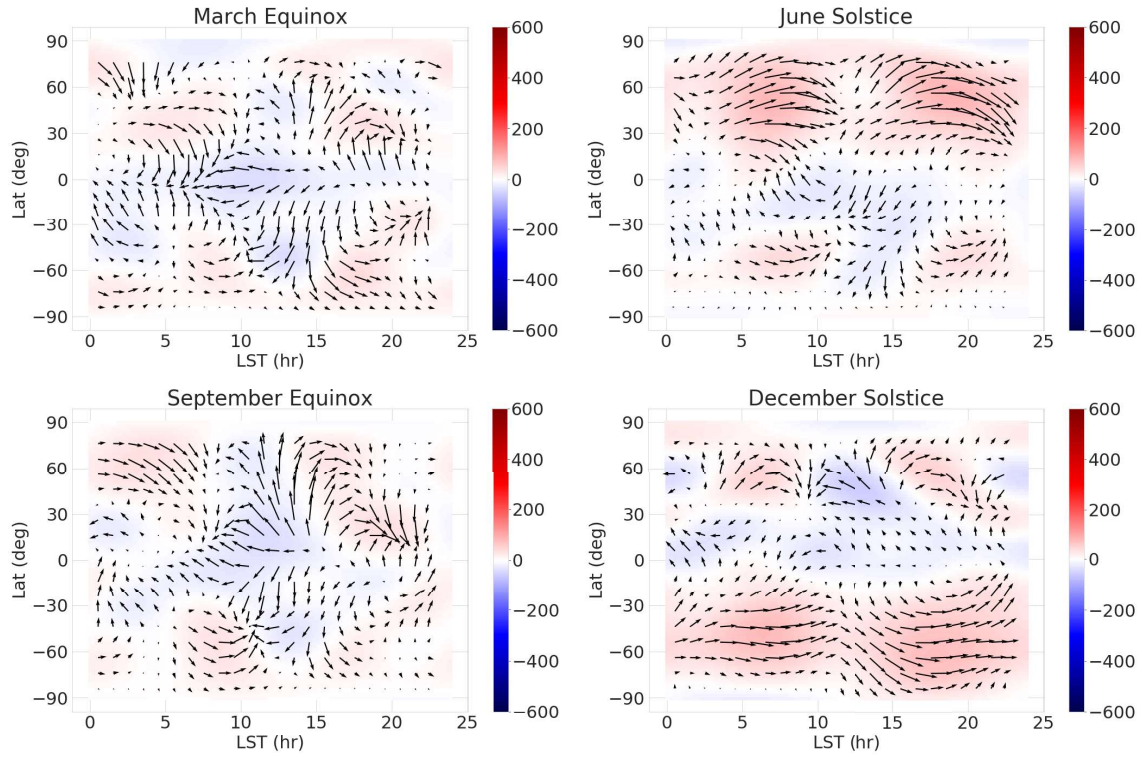
Figure 4.2: Seasonal variation of horizontal wind at $100\ km$ altitude and low geomagnetic activity generated by HWM14.
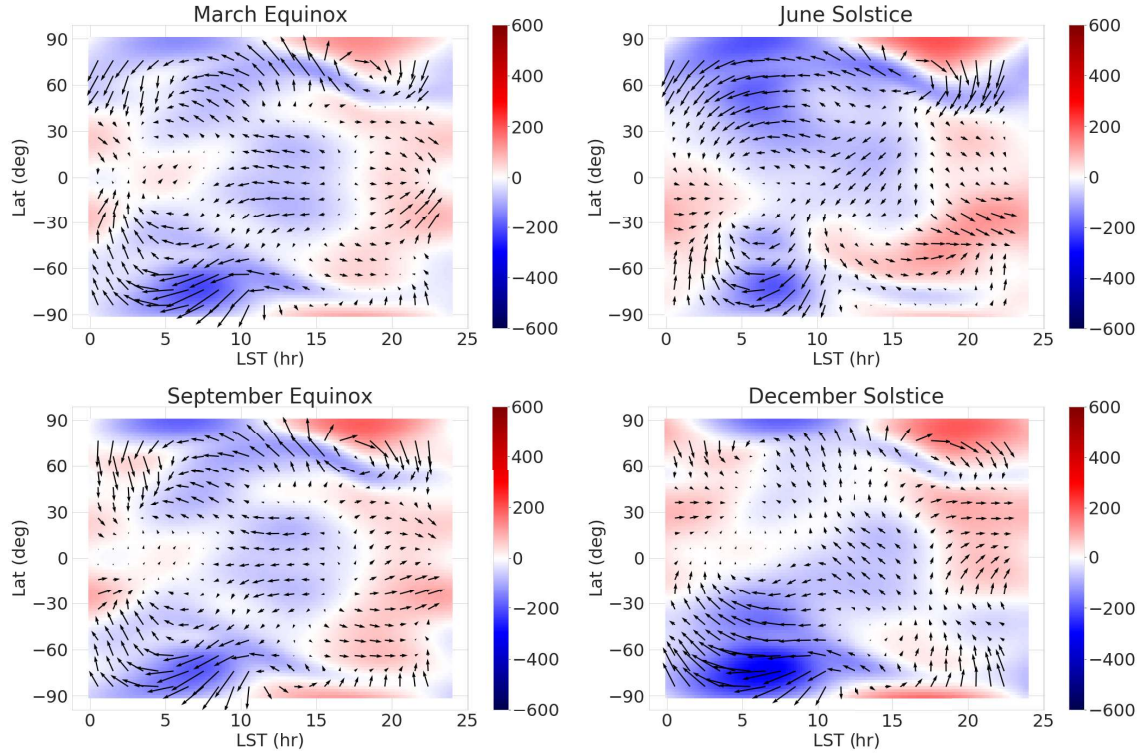
Figure 4.3: Seasonal variation of horizontal wind at $200\ km$ altitude and low geomagnetic activity generated by HWM14.

Next, the horizontal wind fields are shown as a function of altitude. There are two ways to do this. First of al the meridional wind can be plotted as a function of altitude and latitude, as in Figure 4.4. Secondly, the zonal wind can plotted with respect to altitude and LST, as given in Figure 4.5. In Figure 4.4, the two different plots represent the wind during geomagnetic quiet time conditions (left) and during geomagnetic storm conditions (right). It can be concluded from HWM14 that at high altitudes the largest winds are at the poles and these flow down to the latitude where it is night at that moment in time. For the March equinox as depicted in Figure 4.4, this is around a latitude of 0 degrees. Furthermore it should be noted that the wind has a larger magnitude and more constant with altitude at higher altitudes.

When the geomagnetic activity increases, the wind increases at the poles, and influences the wind higher than ± 140 km. At lower altitudes, there is a lot of variation visible in the wind. Especially around altitudes between 100- 150 km altitude. These kind of variations can only be measured by an in-situ, continuous data set.
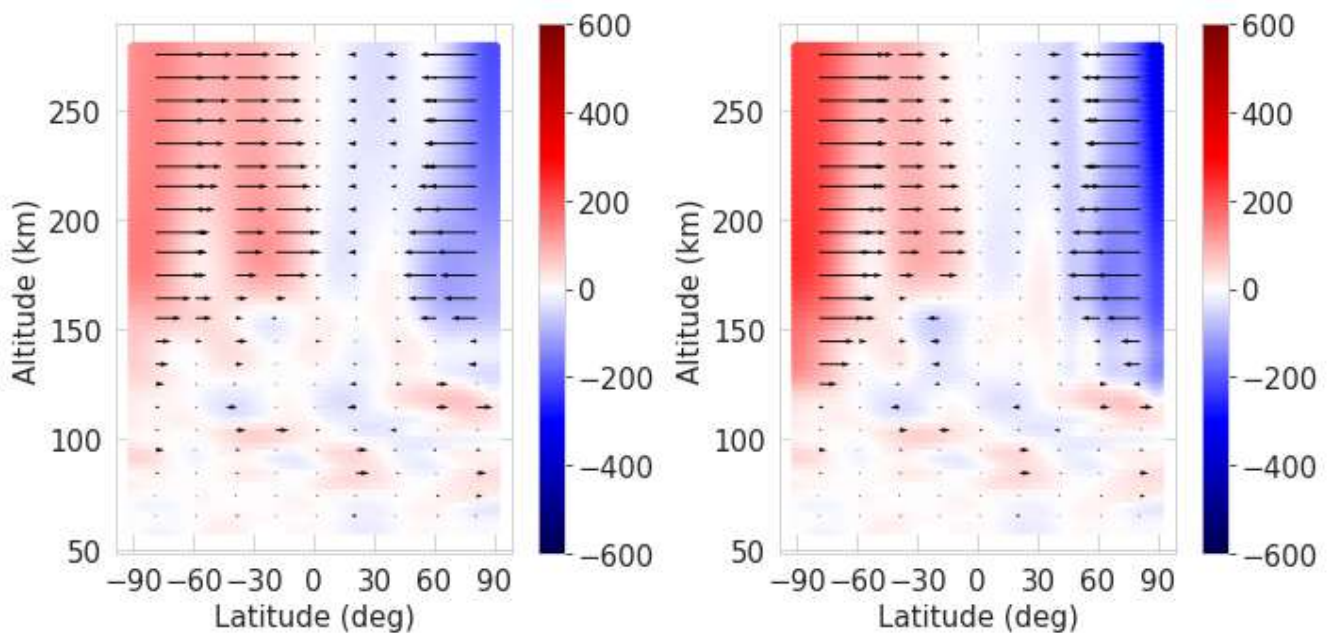
Figure 4.4: Vertical wind field of meridional wind at March equinox at midnight during low (left) and high (right) geomagnetic activity.

In Figure 4.5, the zonal wind is plotted as a function of altitude and LST. The wind seems to be flowing mainly from day to night. Again, the wind seems to be fairly constant with altitude above ± 180/200 km. Below 100 km, a mostly eastern wind can be found. In between, the wind is variable with altitude. The largest winds seem to be during the morning. Here the winds from the day part of the thermosphere flow to the night part of the Earth. In the afternoon there are more ions present in the ionosphere and thermosphere than in the morning, due to the interaction of the solar radiation and the neutrals. Because of this the ion-neutral drag is lower in the morning and the wind is larger. In addition, it can again be seen that when the geomagnetic activity increases the wind at altitudes higher than ± 140 km increases as well. Now the largest winds can be found in the late-afternoon.
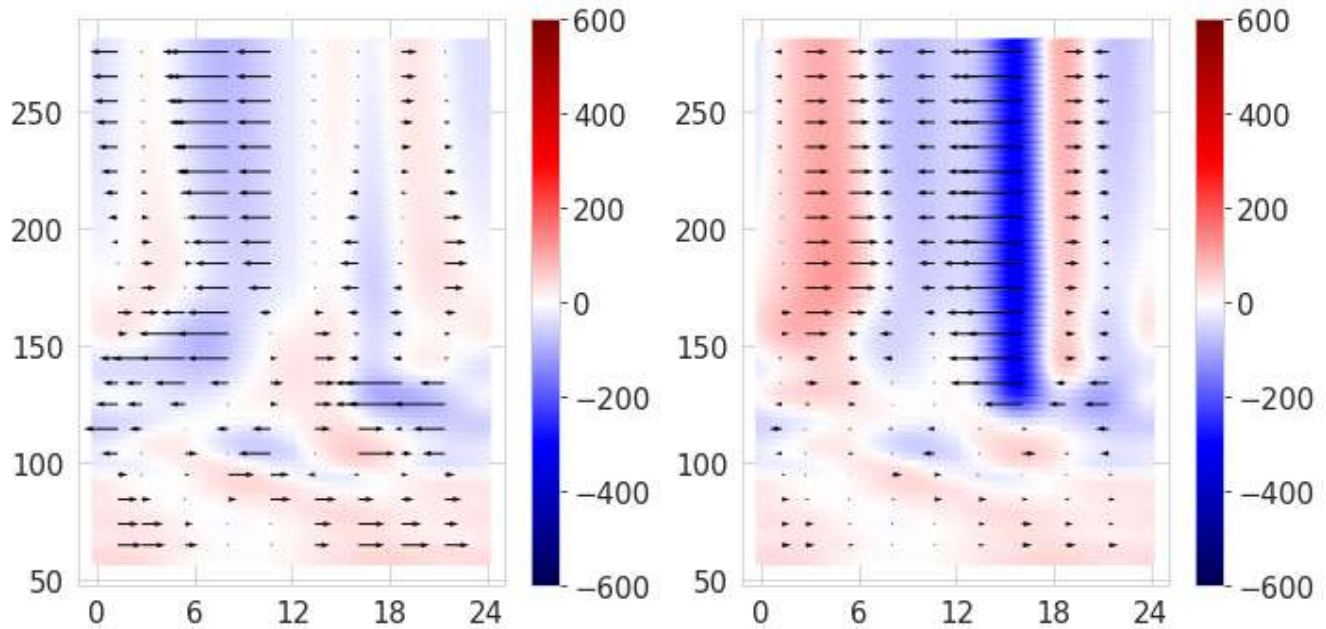
Figure 4.5: Vertical wind field of zonal wind at March equinox at 60 deg Latitude at low (left) and high (right) geomagnetic activity.

To summarize, most variations in horizontal wind with altitude can be found in HWM14 below $\pm\,200\ km$. The geomagnetic activity mostly influences wind at an altitude around and higher than $\pm\,140\ km$. To fully understand this region, high altitude precision of the measurements is needed. Often in-situ wind data has a better altitude precision than remote data, therefore for this region in-situ measurements are preferred. This substantiates the choice of using in-situ data when comparing thermospheric wind data to thermospheric wind models in the data analysis in the next chapter.

Chapter 5

Thermospheric wind analysis

To know what the influence of wind on satellite dynamics is, naturally it is important to know what kind of wind the satellite can encounter during its lifetime. In a design process, often models, like HWM14 of the previous chapter, are used to make an estimation of the wind that the satellite will encounter during its lifetime. However, the models of the lower thermosphere are known to be uncertain due to the lack of observation data. The purpose of this chapter is to compare a thermospheric wind model to in-situ data in order to find the errors of the models.

Most of this analysis has been performed during the internship prior to this thesis. The complete analysis can therefore be found back in Toonen [2020a]. In section 5.1, the HWM14 is further introduced and in section 5.2, the in-situ data sets that are used are explained. In section 5.3, the wind from the model and datasets are compared and the choice of the wind magnitude that will be used as wind input in the aerodynamic modeling is substantiated.

5.1   Horizontal Wind Model 2014

The model that is being used in this research is the HWM14. This model is a so-called empirical model. This means that it is based on a collection of data from different sources. More information can be found in the paper of Drob et al. [2015]. HWM14 includes the GOCE measurements and some of the chemical tracer data. Other data that is included in HWM14 is Fabry-Perot Interferometer (FPI) [Aruliah and Rees, 1995], WINDII [Shepherd, 1993] and Incoherent Scatter Radar (ISR) [Salah and Holt, 1974] and Neutral Atmosphere Temperature (NATE) [Spencer et al., 1973]. HWM14 interpolates and averages all the data in order to get a global coverage in time and space. Because of this, the data will be averaged out and it can be expected that the model will underestimate some of the highest winds.

The reason for choosing HWM14 as wind model is that HWM14 is open source and easy to use. The model is used to give an indication in the difference of dynamic range of a model with respect to the data. In this thesis, the aerodynamics of the satellite will be tested for multiple wind inputs within that range. Therefore, the interested reader, can based on dynamic range of their respective model, find the influence of the dynamic range on the aerodynamic coefficients in the plots presented later in this thesis. Another often used model is the Thermosphere-Ionosphere- Electrodynamics General Circulation Model (TIE-GCM) [Richmond et al., 1992]. TIE-GCM is a physical model, which means that the model is based on complicated equations that describe the processes in the thermosphere and the relation to the different outputs. TIE-GCM is therefore more complicated to run and takes much more computation time. This is why it has been chosen not to use TIE-GCM.

5.2   In-situ wind data

Two different types of in-situ data are used. The first type is chemical tracer (CT) data on board of sounding rockets. The second type is accelerometer data from the GOCE. GOCE normally orbited at an altitude of approximately 270 km. The data that is obtained during the deorbit phase, is in the range of 160-250 km approximately, and is therefore used to compare to the CT on the sounding rockets. In the following subsections the characteristics of both data sources are explained.

5.2.1   Chemical tracers onboard of sounding rockets

The CT data originates from Miguel Larssen [Larsen, 2000] [Larsen et al., 2003]. Chemical tracers are carried on sounding rockets. With the use of triangulation the motion of the chemical tracers is tracked and the wind is modeled. The wind measurements that are performed will result in vertical profiles of horizontal winds. The altitude range at which the measurements are performed, can be controlled. Due to the high speed and short lifetime, only a single profile measurement at a single location over a time period of a few minutes can be obtained with one rocket. This means that statistical comparisons are difficult and that it has been impossible to get a global coverage with only sounding rocket observations. The CT data that has been used consists of 565 runs performed between 1955-2009 at 35 different locations. These locations are given in Figure 5.1.
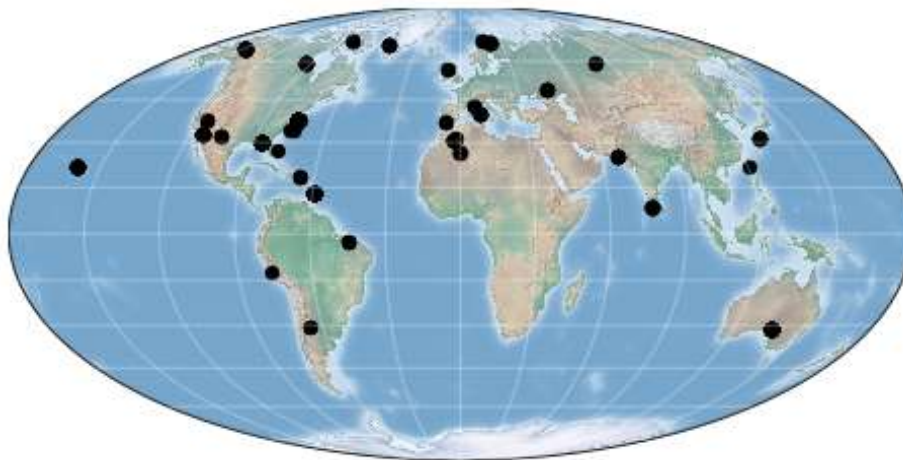
Figure 5.1: Chemical tracer rocket launch locations.

The spatial resolution in altitude of most runs is 0.5 km. In [Larsen et al., 1997], [Larsen et al., 1998] and [Larsen, 2000] estimates were made for the uncertainty of chemical release measurements. The estimates are in line with the errors that were found by Larsen [2002], in which a literature search had been performed to this matter. The errors found are around 5-10 m/s or less. These errors exist of instrumentation errors, triangulation errors and fluctuation in the medium. The biggest uncertainties for the chemical tracer technique is in the altitude ranges when large vertical shears occur [Larsen et al., 2003].

To give some insight in the data, a few example runs are shown, both for zonal and meridional wind. This example is given in Figure 5.2. The vertical profiles show small and big variations in horizontal wind.
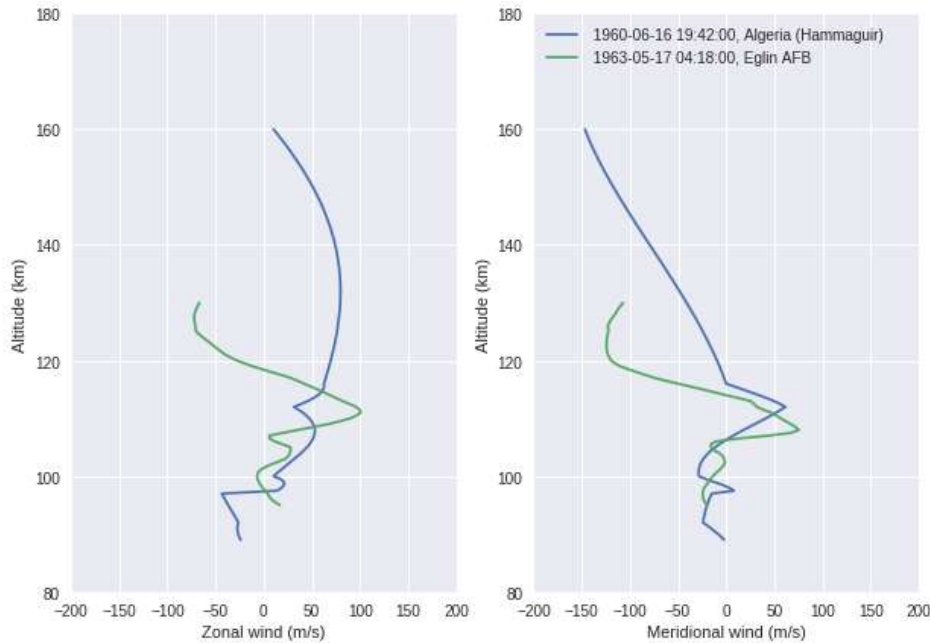
Figure 5.2: Two examples of vertical wind profiles measured by CT on board of sounding rockets.

5.2.2   Accelerometer onboard of GOCE

The GOCE dataset on the other hand is a much more continuous data set, with measurements every 1 or 10 seconds. GOCE orbited at around 270 km altitude. GOCE was operational between November 2009 till November 2013. The last month was signified as the deorbit phase, in which some measurements at lower altitudes were obtained. The deorbit data measured the wind between 22-10-2013 and 10-11-2013 at an altitude range of 164.59 - 254.70 km.

Originally the accelerometer onboard of GOCE was not meant to be used to measure the wind velocity or gas density. However, since many years, accelerometer data coming from orbiting satellites has been used for measuring density in the thermosphere. Examples of papers in this topic are from Guo et al. [2007], Müller et al. [2009], Liu and Lühr [2005], Sutton et al. [2005]. Later on, accelerometer data was also used to obtain thermospheric wind data. One of the first thermospheric measurement techniques that can measure in the cross-track, along-track and radial direction of the satellite is the Satellite Electrostatic Triaxial Accelerometer (SETA) system, proposed by Marcos and Forbes [1985]. It has been flown by the Air Force Geophysics Laboratory on on eight satellites since 1968, including the atmosphere explorers C, D and E. SETA measured cross-track wind derived from the accelerations of the satellite between the altitude range of 170 and 210 km. The uncertainties are in the order of 200 m/s in the in-track direction and 60-160 m/s in the cross-track direction. Through the years this method has been adapted and improved.

Accelerometer observations are often band limited and require calibration. These calibration parameters can not be determined from ground test, due to the difference in the gravitational environment. Therefore, it is necessary to have an iterative derivation for these parameters. Doornbos et al. [2010] presents an iterative density and wind derivation algorithm using data from the multiaxis accelerometer onboard of CHAMP. The magnitude of the errors for this algorithm depends on the external errors. Without external errors the Root Mean Square (RMS) density errors are only 0.03% and the rms wind errors only 1 m/s. However, the errors due to the instrument calibration and the uncertainties in the external models are dominant. The errors can have a maximum of 915 m/s when calculated in an iterative way [Doornbos et al., 2010]. An improved version of the calculation of the thermospheric cross-wind is performed by Visser [2019]. He uses both linear and angular satellite dynamics to calculate the cross-track

wind. It was found that the errors in the vertical wind are less than 50 m/s and less than 100 m/s for the horizontal winds.

Furthermore it was found that the calculations for the horizontal wind are the most accurate in cross-track wind direction. For most of GOCE's orbit, due to its high inclination, the cross-track wind is in the direction of the zonal wind. At the poles, GOCE measures both zonal and meridional winds, but only in the cross-track direction. This means that the total wind vector is not complete. In Figure 5.3, a few hours of the GOCE wind is plotted. The letters in the top signify when GOCE was at the highest (N) or lowest latitude (S) of its orbit. The wind seems to be stronger at the poles. The altitude of GOCE follows a recurrent pattern around an altitude of approximately 270 km. GOCE is highest at the South pole and lowest at the North pole.
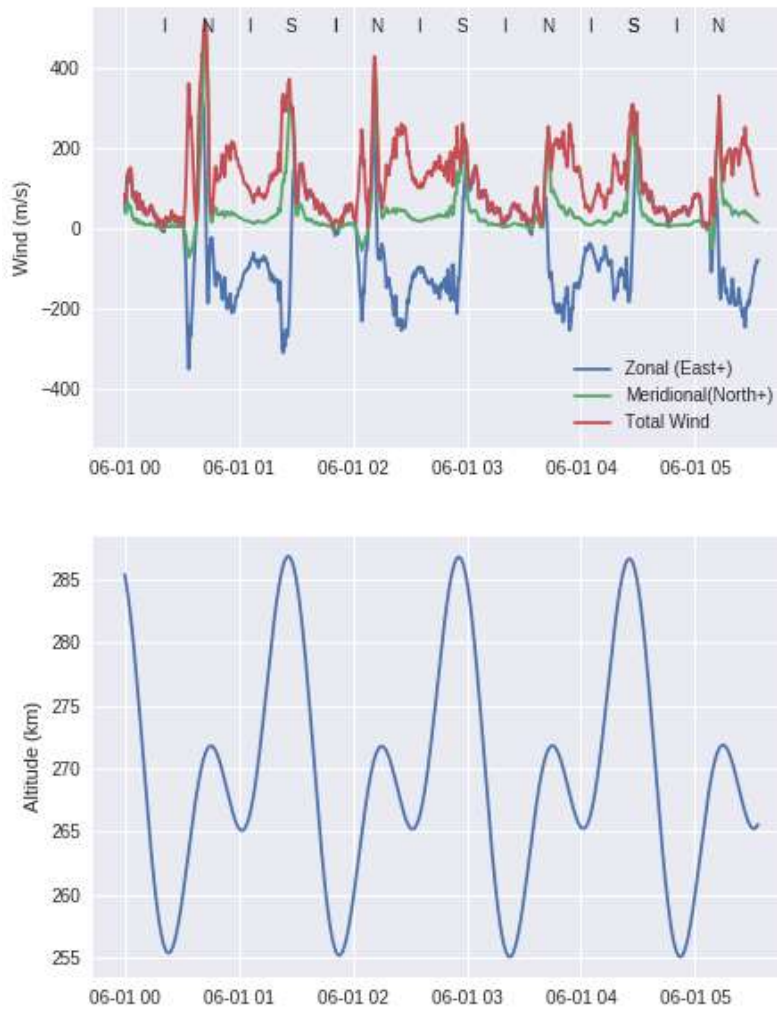
Figure 5.3: Horizontal wind measured by GOCE during the first five hours of 01-06-2010. North (N), South (S) and Equator (I) are indicated on top of the top figure. The bottom figure signifies the altitude of GOCE for the same time period.

5.3   Comparison and uncertainties

The extended analysis and comparison of the wind from the CT, GOCE and HWM14 can be found in the report made for the internship prior to this thesis that researched in-situ wind in the lower thermosphere for the purpose of providing information for the science study of Daedalus [ESA, 2020] [Toonen, 2020a].

Part of that information is useful for this thesis as well and is summarized here.

There are differences between the GOCE data, the CT data and HWM14. It is not possible to compare the GOCE data to the CT data directly due to the unavailability of data from both data sets that overlap in location and moment of time. However, it is possible to bin all the data based on the thermospheric conditions that influences the wind, as explained in the previous chapter. In this way, data from different moments in time can be compared with each other. In Figure 5.4 an example is shown where GOCE and CT zonal wind is plotted with respect to altitude and local solar time. The data is selected based on geomagnetic activity (A_p), latitude and day of year.

Here it can be seen, that the structures in the lower thermosphere (around 100 km) seem to be captured both in the CT data as well as in the HWM14 results. However, the colors of the data often seems to be more intense, which means that the wind measured by the CT is higher. Something else that should be noted is that the wind measured by GOCE has a larger magnitude than the wind obtained from the CT and from HWM14 with the same thermospheric conditions.
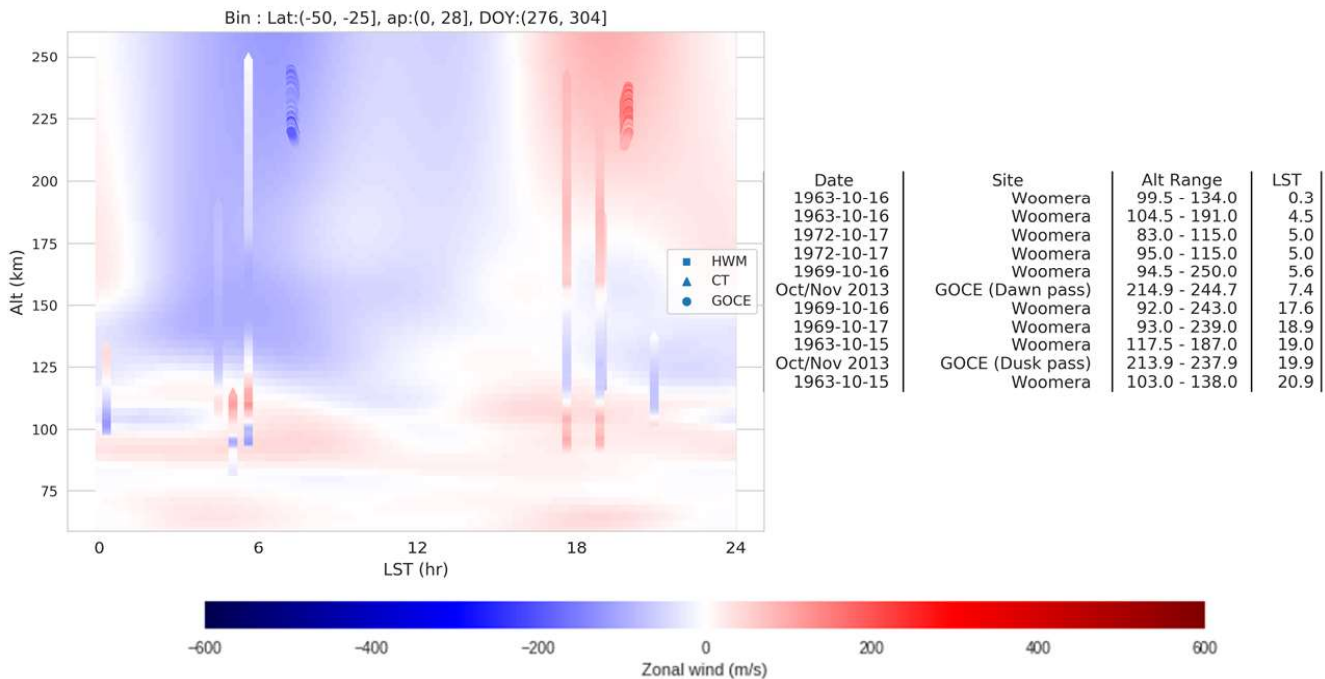
Figure 5.4: Vertical profiles of zonal wind from chemical tracer data and GOCE data, with HWM14 in the background at mid-latitude, low geomagnetic activity in October.

To investigate this more thoroughly, all the chemical tracer horizontal wind data and the GOCE horizontal wind data are plotted with respect to altitude in Figure 5.5. It is important to note that there are only a few chemical tracer profiles that are in the altitude range of GOCE. Due to the under-sampling of the chemical tracers in that region, it is not possible draw strong conclusions from the comparison of chemical tracers and GOCE. Therefore, both data sets are only compared to the data obtained from HWM14.

To do this, the thermospheric conditions of every data point are used as input for HWM14 to model the wind. The pink line signifies the maximum HWM14 per altitude, whereas the purple line is the maximum wind found in the data. Here it can clearly be seen that HWM14 does not capture the maximum winds as measured by GOCE and the chemical tracers. The difference between the data and the model,

can not be explained by solely the errors of the data, since these were found to be in the order of 5-10 m/s [Larsen, 2002] for the chemical tracers (most data below $\pm$ 165 km altitude), or in the order of 100 m/s for the GOCE accelerometer data [Visser, 2019].

The difference can be explained, however, by the fact that HWM14 contains data from many different sources. To include all the sources, the data sets are averaged. Because of this, high peaks are filtered out. On the other hand, it was found in the data that HWM14 also overestimates the wind sometimes. One example can be seen in Figure 5.4. On the left side of the graph a chemical tracer profile is shown with a light color blue till white. While in the background, a darker color blue is visible. In a design process, the satellite mission design can be over designed when the wind (and drag), is overestimated. This will result in a too heavy or expensive design. However, when the wind is underestimated in the design process, it could decrease the mission's lifetime and could therefore endanger the mission's science objectives. That is why it is of vital interest to know what kind of influence the underestimation of the wind has on the satellite dynamics. It has been decided to focus in this thesis on the underestimation of the wind only.
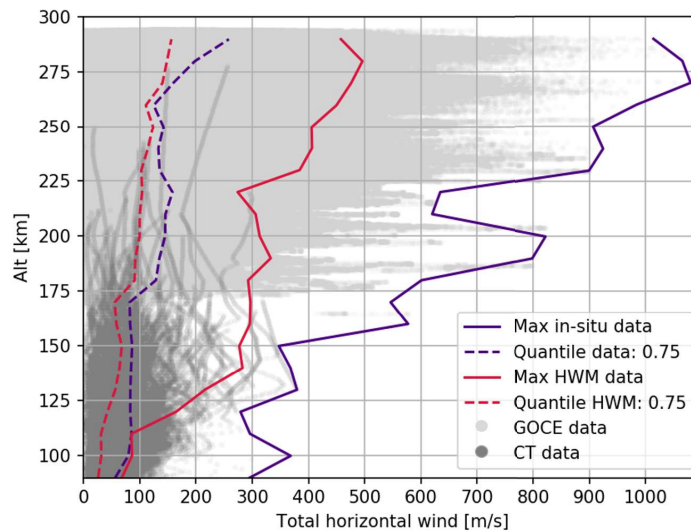
Figure 5.5: The total horizontal data from in-situ data, GOCE (light grey) and chemical tracers (dark grey), with the maximum winds per altitude marked for the data (purple) and model (pink). The 0.75 quantiles of the respective wind data sources are shown with striped lines.

In addition, the dotted lines signify the 0.75 quantiles for both the HWM14 and in-situ data. From this it can be concluded that 75% of the wind found in the data is below 100 m/s for an altitude of 120 km and below a magnitude of 280 m/s for an altitude around 300 km. The 0.75 quantiles of the data and HWM14 are much closer together. For HWM14, 75% of the wind found in the data is below 50 m/s at 120 km and below a magnitude of 150 m/s at 300 km. As explained about the orbit design in section 3.1, a mission like Daedalus is most valuable if it covers all local solar times, and many latitudes at its perigee altitude to get the global coverage of the LTI. Consequently, it is expected that the satellite encounters all kinds of winds from all different sides. It is highly probable that the satellite will also encounter the worst case scenario during its lifetime. That is why it is chosen to see what the influence is of the underestimation for the worst case scenario, with other words, the maximum dynamic range of the data compared to the maximum dynamic range of the model. The aerodynamics of the satellite will be computed for multiple wind inputs within those ranges.

At both the TF altitude of 120 km and FMF altitude of 300 km, the dynamics of the satellite is analyzed for three cases:

- No wind

- Wind from model

- Wind from in-situ data

For the two cases that include wind, the maximum wind of the respective data source and model at that altitude is taken to test for the worst-case scenario. From Figure 5.5, it can be seen that the maximum wind is quite variable depending on the altitude. From the theoretical background in chapter 4, it was found that the largest wind can be expected at the highest altitudes. However, in Figure 5.5, the maximum wind can be found around 270 km instead of 290 km as was expected. This can be explained by the fact that GOCE was orbiting around an altitude of approximately 270 km. Therefore, most measurements were taken at that altitude over a longer period of time and there is more chances to encounter large winds. That is why, to be sure that the worst-case scenario is obtained, the maximum winds within a range around the respective perigee altitudes of 120 km and 300 km are chosen. From Figure 5.5, the following wind magnitudes are obtained for the respective ranges.

Table 5.1: Maximum wind magnitudes in m/s for HWM14 and GOCE & CT.

Altitude Range	**120 km** 110-130 km	**300 km** 270-300 km
HWM 14	200	500
In-situ data	370	1080

Part III
Aerodynamic modeling

Chapter 6

Satellite aerodynamics

Even though the density in space is low, due to the velocity of the satellite and the particles itself, collisions occur. These collisions induce a certain drag, lift and moment on the satellite. The drag, lift and moments are dependent on the aerodynamic coefficients. The aerodynamic coefficients are influenced by the way that particles hit the satellite surface and are reflected. Next to the wind, there are other variables that influence how these collisions take place and therefore that influence the aerodynamic coefficients. In this chapter, the theoretical background is given for the satellite (aero)dynamics.

First in section 6.1, the equations of motion of a satellite around the Earth is given. The largest contribution, apart from to the gravitational forces, to the equations of motion in the x and z direction for a LEO satellite are the drag and lift. Drag causes the orbit of the satellite to decay. This is more thoroughly explained and quantified for this specific case in section 6.2. To obtain the drag and lift, the drag and lift coefficient needs to be known. Therefore, in section 6.3, analytical expressions are given for the drag coefficient (C_D) and the lift coefficient (C_L) for for simple satellite geometries in the FMF to understand what variables influence the coefficients. These variables can be divided into thermospheric conditions and satellite wall properties. In section 6.4, the variability of the thermospheric conditions are explained and a nominal value is chosen as well as a range that is tested in the sensitivity study. In section 6.5, the satellite wall collision parameters are explained. These are not influenced by the variability of the thermosphere, but they do contain uncertainties due to lack of observational data of these parameters.

6.1 Equations of Motion

Many books have been written about satellite dynamics, for example the books from Wakker [2015] and Curtis [2013] have often been used during the master of Space Exploration at the TU Delft. The first hand estimation of a satellite's orbit around the Earth, is obtained by solving the two-body problem, in which only the constant gravitational force of the planet on the satellite is taken in to account. The two-body problem is based on Newton's law of gravitation given in Equation 6.1.1

$$F_G = G\frac{mM_{Earth}}{r^2} \tag{6.1.1}$$

In Equation 6.1.1, F_G is the gravitational force, G is the gravitational constant, m is the mass of the satellite, M_{Earth} is the mass of the Earth and r is the distance between the centers of mass of both bodies. Combining this with the second law of Newton $F_G = m \cdot a_G$ results in the acceleration given in Equation 6.1.2.

$$a_G = -\frac{\mu}{r^2} \tag{6.1.2}$$

μ is the Earth's gravitational parameter and is equal to the gravitational constant times the mass of the

Earth, GM_{Earth}. r depends on location of the satellite in its orbit. The equation for r is the following:

$$r = \frac{a(1-e^2)}{1+ecos(\nu)} \tag{6.1.3}$$

a is the semi-major axis, e is the eccentricity and ν is the true anomaly. This approach assumes that the only force on the satellite is the gravitational force assuming a spherical symmetric gravity field. This is the biggest force acting on the satellite [Montenbruck and Gill, 2002].

Next to the gravitational acceleration, in this research the focus will be on the accelerations due to aerodynamic forces. The accelerations in the along-track direction, like drag, have more influence on the orbit geometry than the cross-track component, like lift [Montenbruck and Gill, 2002]. In addition, the aerodynamic forces act mainly in the direction of the relative velocity of the flow with respect to the satellite. From before, it was found that in this case only the drag (including wind) needs to be taken into account when speaking about aerodynamic forces. It should be noted however, that the accelerations in the other directions, even though not discussed in this thesis, could be measured by accelerometers on-board of a satellite. The acceleration due to drag, slows down the spacecraft. If no additional propulsion is used, the satellite will start to decay. An example of this, will be given in the next section. The primary equation for drag, D, is Equation 6.1.4

$$D = \frac{1}{2}C_D\rho A_{ref}V_r^2 \tag{6.1.4}$$

ρ is the density of the medium, A_{ref} is the reference area or affected surface area and V_r is the relative velocity of the satellite with respect to the medium [Clark et al., 1996]. C_D is the drag coefficient, that describes the interaction between the atmospheric particles and the satellite surfaces [Doornbos and Klinkrad, 2006]. The acceleration due to the drag force is based on Newton's second law as explained before. The result is given in Equation 6.1.5.

$$\bar{a_D} = -\frac{1}{2}C_D\rho\frac{A_{ref}}{m}\bar{V}_r^2\bar{u_D} \tag{6.1.5}$$

All characters are explained in the previous paragraphs, except for $\bar{u_D}$. $\bar{u_D}$ is the unit vector of the drag acceleration. The complexity of this equation lies with the fact that almost all parameters of Equation 6.1.5, except for the mass [Doornbos and Klinkrad, 2006], are changing due to the variability of the thermospheric parameters influenced by space weather. First of all, space weather influences the density of the thermosphere. Secondly, the velocity vector $\bar{V}$ of the satellite changes when the magnitude and direction of the thermospheric wind changes. These changes in the equation are rather straight forward. However, the total $C_D * A_{ref}$ of the satellite is much more difficult to obtain. It depends on the shape of the satellite, the gas properties, which depend on space weather too, and the attitude of the satellite with respect to the flow which is dependent on the wind and the satellite's attitude control. The analytical expressions for C_D will be given in this chapter and a computational method of obtaining $C_D * A_{ref}$ will be proposed in the next chapter.

6.2 Orbital decay due to drag

As mentioned before, the acceleration due to the drag exerted on a satellite can decay the orbit. This can either reduce the operational life-time and therefore endanger the satellite's scientific requirements, or can increase the propulsion power requirement to keep the satellite in orbit. Both options are unfavorable. That is why in this section, a first-order approximation of the influence of the drag due to density, wind and other thermospheric parameters on the decay of a satellite like Daedalus is given. To do this, an expression is used that describes the decay due to the influence of atmospheric drag alone in terms of the change in semi-major axis, a [Picone et al., 2005] [King-Hele and Walker, 1987]. This expression is given in Equation 6.2.1.

$$\frac{d}{dt}a = \frac{2a^2v}{\mu}\bar{a_D}\bar{u_v} \tag{6.2.1}$$

$\bar{u}_v$ is the unit vector in the direction of the satellite's velocity in Earth-centered inertial coordinates, v. To get from the relative velocity, V_r, in Equation 6.1.5, to the Earth-centered inertial velocity, v, the dimensionless wind factor F is used.

$$\bar{V}_r^2 = F * \bar{v}^2 \tag{6.2.2}$$

Inserting Equation 6.1.5 and Equation 6.2.2 in Equation 6.2.1 results in Equation 6.2.3.

$$\frac{d}{dt}a = -\frac{a^2 \rho C_D A_{ref} v^3 F}{m\mu} \tag{6.2.3}$$

King-Hele and Walker [1987] gives an approximation to F as stated in Equation 6.2.4.

$$F \cong \left(1 - \frac{rw}{v}cosi\right)^2 \tag{6.2.4}$$

w is the angular velocity of the Earth's rotation and v is the inertial velocity of the satellite at that point in the orbit. The inclination for Daedalus, i, is obtained from ESA [2020] and equals 85°. To obtain the total decay for the complete orbit, this expression is integrated over a single Kepler orbit. To do this, a function is used that calculates a Kepler orbit, for a given semi-major axis, a, eccentricity, e, inclination, longitude of the ascending node, Ω, and argument of perigee, ω. Furthermore, the location of the Kepler orbit at t_0 is specified by the mean anomaly for t_0. The Kepler elements were shown in the explanation of the orbit geometry in section 3.1. The function starts by calculating the mean motion, n, of a satellite in the orbit by

$$n = \sqrt{\mu}a^3 \tag{6.2.5}$$

With the mean motion and the timestep, the mean anomaly at t_0 can be updated to the new mean anomaly after timestep, dt. The mean anomaly after dt is then converted into the eccentric anomaly. From the eccentric anomaly, the inertial coordinates and velocities can be calculated with the use of i, ω and Ω. The inertial position and velocity after each timestep can then be used as input for the equation of F in Equation 6.2.4. The inertial velocity can be directly inserted in Equation 6.2.3 as well.

In addition to F and v, the drag coefficient times the reference area, $C_D * A_{ref}$ is needed. Further on in this thesis the method of obtaining the drag coefficients is extensively explained. In section 9.3, $C_D * A_{ref}$ for five different altitudes in the range of 120 - 300 km altitude have been calculated. These values correspond to the standard satellite shape, assuming no thermospheric wind and no side-slip angle, roll nor angle of attack at the respective altitudes. From these 5 values, the $C_D * A_{ref}$ for every altitude will be linearly interpolated. Finally, the density, ρ, is obtained by NRLMSISE-00 at every timestep Picone et al. [2002]. The input conditions for NRLMSISE-00 are expressed in longitude, latitude and altitude. These can be obtained by transforming the inertial coordinates, from before, to Earth-fixed coordinates. From the Earth-fixed frame, the geodetic latitude, longitude and altitude can be obtained as input for the NRLMSISE-00. The mass, m, is assumed to stay constant and equal to 1200 kg [ESA, 2020].

The resulting change of the semi-major axis can in turn be used to update the semi-major axis and eccentricity. The updated semi-major axis, eccentricity and mean anomaly will in turn be used again as input for the Kepler orbit function. This integration is performed each timestep until the period of one orbit is reached. The timestep taken is $dt = 1$ s. Because for this timestep the value for the change in semi-major axis has converged. By further decreasing dt, the running time will be increased, but the value for the decay does not change.

These simplified computations show the change of the semi-major axis solely due to the drag influence. It should be noted however, that in reality, periodic variations, due to for example gravitational perturbations can also be found in the semi-major axis variations.

The results are given in Figure 6.1. First of all, in Figure 6.1a the cumulative decay for one orbit with respect to the altitude of the satellite is shown. This shows which part of the orbit mainly influences the decay of semi-major axis. It can be concluded that for a satellite like Daedalus, the orbital decay of

the semi-major axis is due to the drag at altitudes lower than 200 km altitude. 96% of the decay is due to the drag at altitudes lower than 150 km.
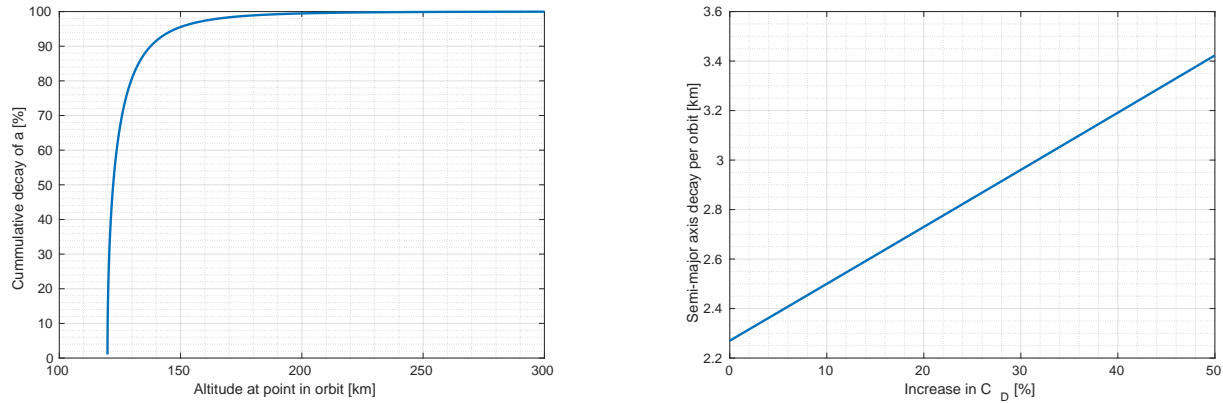
(a) The contribution to the total decay per altitude for one orbit.

(b) Decay of the semi-major axis per orbit for increase in C_D.

Figure 6.1: Decay of the semi-major axis for one orbit based on the theory of King-Hele and Walker [1987], explained in Picone et al. [2005].

It is expected that the $C_D * A_{ref}$ will change over the course of the satellite's mission duration, due to the change in thermospheric conditions. Based on the previously made conclusion, the biggest influence on the satellite decay is at altitudes lower than 150-200 km. It is interesting to get an idea of the decay of a satellite due to a change in the drag coefficient at the lowest altitudes. To show this, a simplified estimation is made where the value for the $C_D * A_{ref}$ values have been multiplied by a factor increase. The previously described computations have been run for multiple factorial increments in $C_D * A_{ref}$ integrated over one orbit. The result is given in Figure 6.1b. It is found that for a 10% increase in $C_D * A_{ref}$, the decay per orbit also increases by 10%.

The remainder of this chapter will investigate further on what influences the drag and especially the drag coefficients. Due to the complexity of the aerodynamic coefficients, the focus will be on understanding what influences them. With this information, in chapter 7, a method is proposed to obtain the aerodynamic coefficients for a satellite flying low through the thermosphere.

6.3 Analytical expressions of aerodynamic coefficients

In the FMF regime, analytical expressions exist that express the aerodynamic coefficients of simple geometries. Unfortunately, there is no analytical expression available for the TF regime and for complex geometries. Therefore, in this thesis, a computational method of obtaining the aerodynamic coefficients is proposed in chapter 7. The below explained analytical expression will be used to show what influences the aerodynamic coefficients and to validate the proposed method.

The aerodynamic coefficients for a flat plate in FMF can be described following Sentman's formulas [Sentman, 1961], given in Equation 6.3.1 and Equation 6.3.2. The j-index signifies the j-th constituent.

$$C_{D,i,j} = \left[\frac{P_{i,j}}{\sqrt{\pi}} + \gamma_i Q_j Z_{i,j} + \frac{\gamma_i}{2} \frac{v_{re}}{v_{inc}} \left(\gamma_i \sqrt{\pi} Z_{i,j} + P_{i,j} \right) \right] \frac{A_i}{A_{ref}} \tag{6.3.1}$$

$$C_{L,i,j} = \left[l_i G_j Z_{i,j} + \frac{l_i}{2} \frac{v_{re}}{v_{inc}} \left(\gamma_i \sqrt{\pi} Z_{i,j} + P_{i,j} \right) \right] \frac{A_i}{A_{ref}} \tag{6.3.2}$$

with

$$G_j = \frac{1}{2s^2}, \quad P_{i,j} = \frac{1}{s}\exp\left(-\gamma_i^2 s^2\right), \quad Q_j = 1 + G_j, \quad Z_{i,j} = 1 + \mathrm{erf}\left(\gamma_i s\right) \tag{6.3.3}$$

s is the speed ratio. The speed ratio is the ratio of the total relative velocity of the atmosphere with respect to the satellite (V_r) over the most probable (thermal) speed of the gas particles. V_r can be assumed equal to the incoming velocity of the particles V_{inc} [Doornbos, 2012]. The equation for the speed ratio is given in Equation 6.3.4.

$$s = \frac{V_{inc}}{V_{prob}} = \frac{V_{inc}}{\sqrt{2R_{gas}T_{inf}}} \tag{6.3.4}$$

Where R_{gas} is the specific gas constant, T_{inf} is the background gas temperature in Kelvin. The relative velocity consists of the satellite velocity and the relative velocity due to the wind. The specific gas constant is calculated by Equation 6.3.5

$$R_{gas} = \frac{Na * kb}{M} \tag{6.3.5}$$

Here Na is Avogadros number, kb is the Boltzmann constant and M is the molar mass. The molar mass is different for the various constituents of the gas and is thus dependent on the mixture. If the gas mixture consists of more than one type of constituent, the aerodynamic coefficients needs to be calculated separately per constituents using the right speed ratio. The total aerodynamic coefficient is then obtained by calculated the weighted mean based on the mass concentrations. The mixture is highly dependent on geomagnetic activity, location and altitude.

In conclusion, the speed ratio is dependent on the satellite velocity, wind, gas temperature and composition. These four are considered in the next sections.

Figure 6.2: Angle between incoming flow and normal of the plate, θ.

erf() is the error function and is defined as:

$$\mathrm{erf}(x) = \frac{2}{\sqrt{\pi}}\int_0^x \exp\left(-y^2\right) dy \tag{6.3.6}$$

In these equations, γ_i is the cosine of the angle between the plates normal and the incoming flow direction (drag vector) (θ). l_i is the cosine of the normal and the lift vector, or the sine of the normal and the drag vector. The angle is visualized in Figure 6.2.

$$\gamma_i = \cos\left(\theta_i\right) = -\hat{u}_{\mathrm{D}} \cdot \hat{n}_i, \tag{6.3.7}$$

$$l_i = -\hat{u}_{\mathrm{L}} \cdot \hat{n}_i = -sin(\theta) \tag{6.3.8}$$

Finally, the term $\frac{v_{re}}{v_{inc}}$ is left. This is the ratio of the velocity of the re-emitted particles from the satellite surface to the velocity of the incoming particles. This ratio can be described in terms of the energy accommodation coefficient (α_E), the gas constant (R_{gas}), the wall temperature (T_{wall}) and the satellite speed (v_{inc}), by Equation 6.3.9 from Koppenwallner [2009].

$$\frac{v_{\mathrm{re}}}{v_{inc}} = \sqrt{\frac{1}{2}\left[1 + \alpha_E\left(\frac{4R_{gas}T_{\mathrm{wall}}}{v_{\mathrm{inc}}^2} - 1\right)\right]} \tag{6.3.9}$$

6.4 Thermospheric conditions

Now that the analytical expressions for a flat plate in FMF are explained, it is important to understand the variability of the parameters in the expressions and what influences them. Most variables are

parameters describing the thermospheric conditions. The thermospheric conditions are highly variable. To be able to draw general conclusions nominal values for the thermospheric conditions are chosen. The influence of the variability of the thermosphere is tested later on in the results chapter by measuring the sensitivity to all thermospheric parameters. For the nominal thermospheric input conditions, a value is chosen which is most probable. It is expected that the satellite will mostly fly through geomagnetic quiet time conditions. The nominal values will be based on July 15th 2006 during the day above Delft. The vertical temperature, density, mass concentration and number density profiles for that day are obtained by NRLMISE-00 and plotted in Figure 6.3.
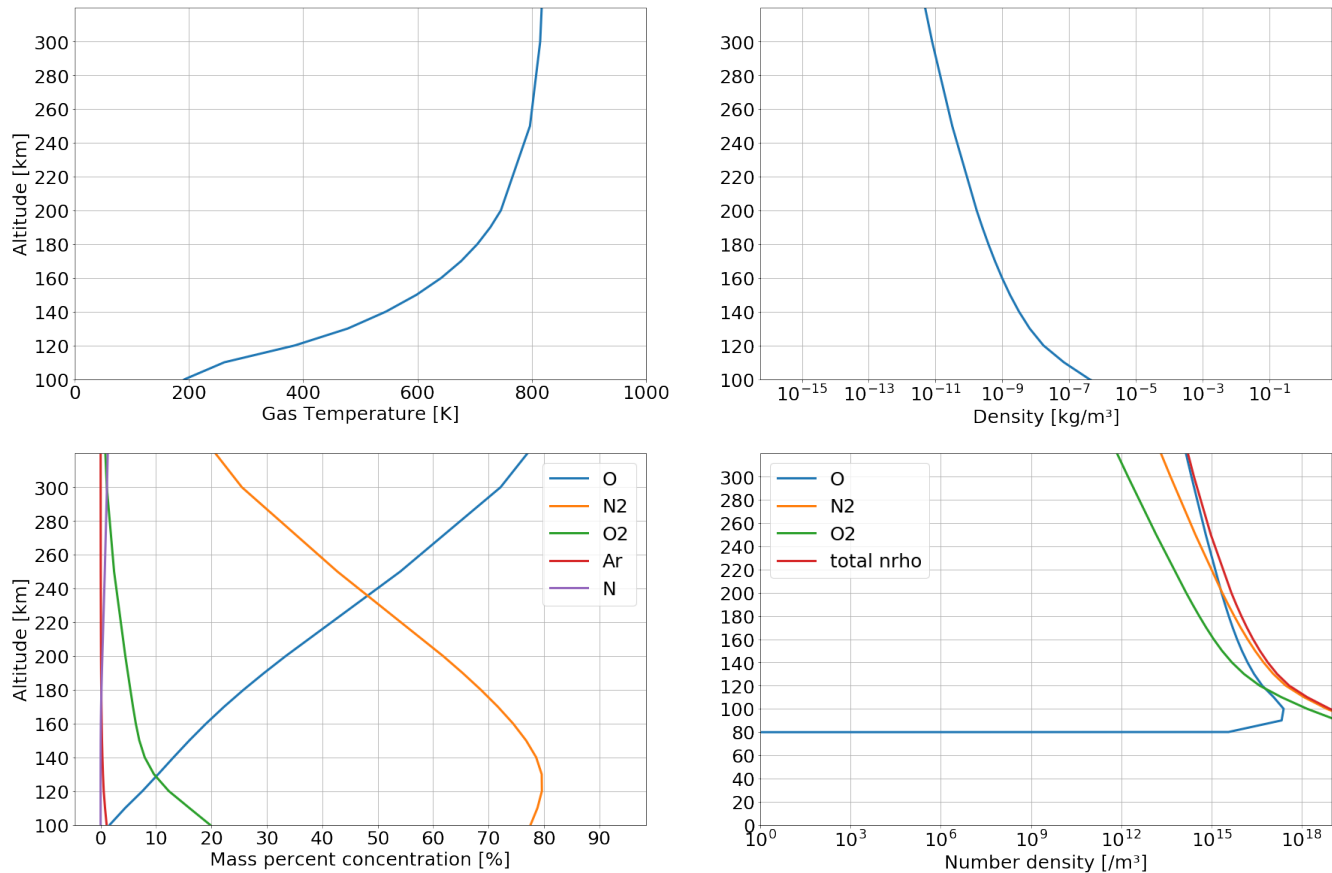
Figure 6.3: NRLMSISE-00 result for neutral temperature, density, composition mass concentrations and number densities for 15-07-2006 18:00 above Delft.

6.4.1   Gas density

Density cannot be found in the closed-form solutions given in section 6.3 for the FMF. This is because the density at high altitudes is extremely low, which means no intermolecular collisions take place and it consequently does not influence the aerodynamic coefficients. Therefore, it can be expected that for high altitudes, changes in terms of density within the FMF regime do not have an influence on the drag coefficient. It is important to note, however, that the density does have a direct influence on the drag in the drag equation.

For lower altitudes, the density is one of the most important variables when speaking about aerodynamics [Mehta et al., 2014]. It is due to the higher density that the satellite undergoes aerodynamic forces like drag and lift. Furthermore, higher density also results in more intermolecular collisions. This in turn influences the density distribution around the satellite and therefore influences the aerodynamic coefficients. The intermolecular collisions also have an influence on the composition which is explained

in the next section.

The density at a certain location in the thermosphere depends on the altitude, season, local solar time, and geomagnetic activity. Often, the total density is expressed in the number density. The number density of atomic Oxygen can, for example, be calculated by Equation 6.4.1.

$$nrho = \frac{\rho_{tot}}{M_O} * Na \tag{6.4.1}$$

Where ρ_{tot} is the total density, M_O is the atomic mass of Oxygen and Na is the Avogadro's number. From Figure 6.3, it is found that for 120 km altitude the number density expressed in atomic Oxygen is approximately equal to 1e18 and at 300 km equal to 1e14 molecules per m^3, which is the same as a density of 2.7e-8 kg/m^3 and 2.7e-12 kg/m^3 respectively.

Due to lack of data for thermospheric density models, there are often uncertainties in the model results. Furthermore, there are uncertainties due to the variability of the thermosphere and its density. Therefore, the sensitivity of the aerodynamic coefficients with respect to changes in the density is checked. The sensitivity range for the density at 120 km altitude is based on Figure 6.4 from ESA [2020] and is approximately equal to 0.5e-8 kg/m^3 to 5e-8 kg/m^3.

6.4.2 Gas temperature

Due to the collisions of the molecules with the satellite surface, energy is transmitted. Temperature is one of the most important energy forms, next to kinetic energy. The gas temperature T_{inf} therefore influences the aerodynamic coefficients. As can be seen in Equation 6.3.4, T_{inf} influences the speed ratio. With increasing T_{inf}, the most probable speed of the gas molecules increases, and the speed ratio, s, goes down. Later it shall be shown that when T_{inf} goes up and therefore s goes down, that the C_D will increase.

When looking at Figure 6.3, it can be seen that the gas temperature increases with altitude in the thermosphere. This is due to large amount of energy that is stored in the coupling between the thermosphere and ionosphere. The energy arrives there from the Solar wind via Joule Heating and Particle Precipitation. In addition, the solar radiation is absorbed by the constituents of the thermosphere. This can result into extremely high temperatures which would never occur on the surface of the Earth. In conclusion, just like the density, the temperature of a location in the thermosphere is influenced by the energy coming from solar radiation and the geomagnetic energy arriving at the geomagnetic poles. Therefore the temperature expected to be dependent on local solar time, the season, or day of year, geomagnetic activity, latitude and altitude.

The nominal value for the low altitude is based on Figure 6.3. This is equal to 400 K at 120 km altitude. The gas temperature at 300 km altitude was set at an early stage on 1000 K. This does not agree with the value of 820 K that is shown in Figure 6.3, however it is still well within the range that is given in Figure 6.4 from ESA [2020]. This is why it is has been chosen not to change this value to limit the number of extra computations.

Just like for the density there is an uncertainty in the temperature due to model uncertainties and due to the thermospheric variability. The range for which the sensitivity analysis is performed is based on Figure 6.4 and equal to 300 K to 600 K for an altitude of 120 km and 500 K to 1600 K for an altitude of 300 km. It has been chosen not to go until 2500 K, since these values are just model predictions and have not been measured yet.
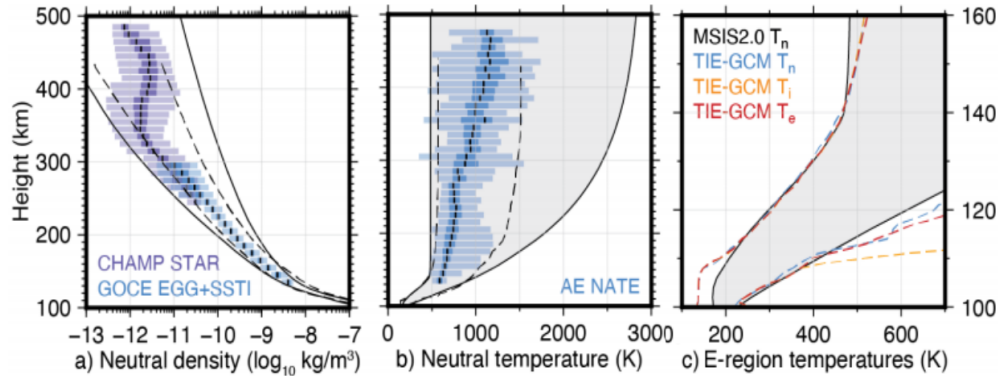
Figure 6.4: Ranges of neutral temperatures and density as a function of altitude Shaded bars reflect percentile distributions of past measurements (1, 25, 50, 75 and 99%), in 10-km altitude bins. Solid lines indicate global long-term minimum and maximum conditions from empirical models (MSIS2.0, IRI-16), credits: ESA [2020].

6.4.3 Gas composition

Not only the gas density and temperature are important, but the composition as well. As mentioned before, the speed ratio includes the specific gas constant which depends on the molecular mass of the constituent. To get the total aerodynamic coefficient, the aerodynamic coefficient per constituent should be calculated and then the weighted average based on the mass concentration should be derived Doornbos [2012].

The mass concentration of all the constituents can be found by running NRLMSISE-00 Picone et al. [2002]. From Doornbos [2012], it was found that the main constituents at low altitudes are atomic oxygen (O), molecular oxygen (O_2), atomic Nitrogen (N), molecular Nitrogen (N_2) and Argon (Ar). For these constituents, the mass concentrations are calculated per altitude. The results are shown in the bottom left graph of Figure 6.3. First of all, it should be noted that the contribution of Ar and N is relatively small. To simplify the simulations later on in this thesis, it has been decided to focus on the three gas constituents with the largest mass concentration; O, N_2 and O_2. Secondly, the mass concentration graph clearly shows that at low altitudes the concentration of molecular Oxygen and Nitrogen is higher than atomic Oxygen. The mass concentration of atomic Oxygen increases with altitude, whereas molecular Oxygen decreases with altitude. This agrees with the knowledge that at low altitudes particle collision exists due to the higher density which results in a more molecular atmosphere than atomic atmosphere. With increasing altitude the density is decreasing and the molecules split into atoms due to gaseous diffusion and dissociation due to radiation. At high altitudes, the largest mass concentration belongs to atomic oxygen. The values for the mass concentrations at 120 km and 300 km altitude is based on geomagnetic quiet time conditions, as presented in Table 6.1.

The composition is highly variable. The variation of the composition at a certain altitude is hard to define. Often in the thermosphere 100% atomic Oxygen is assumed for the thermosphere [March et al., 2019] [Mehta et al., 2014]. The impact of that assumption will be examined in subsection 9.1.3. Furthermore, the composition that is chosen in Table 6.1 was based on geomagnetic quiet time conditions. This will be compared with the composition during geomagnetic storm conditions. The mass concentrations for both thermospheric conditions are given in Figure 6.5.

From this it can be concluded that especially at low altitudes there is not a big difference between the composition of the thermosphere in terms of mass concentrations. This agrees with the findings of the previously discussed variability of the density, temperature and wind. In conclusion, the thermospheric variability is mostly visible at higher altitudes. Due to the higher density at higher altitudes during geomagnetic storm conditions, there are more intermolecular collisions, which results in a more molecular atmosphere than during quiet time conditions. The mass concentrations for geomagnetic

storm conditions is given in Table 6.2.
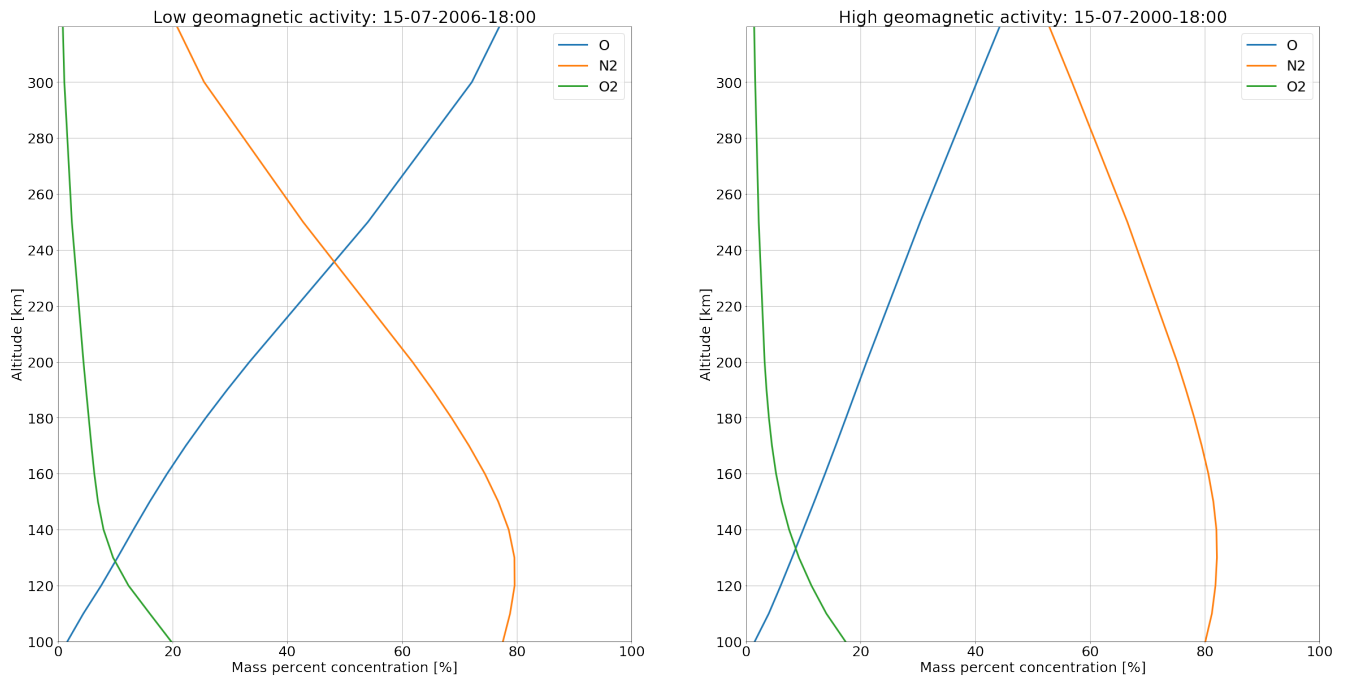
Figure 6.5: Mass concentrations geomagnetic quiet time (left) and during geomagnetic storm (right) of constituents with the highest mass concentrations obtained from NRLMSISE-00 [Picone et al., 2002].

Table 6.1: Mass concentrations of the main constituents of the thermosphere at 120 km altitude and 300 km altitude during geomagnetic quiet time.

Altitude	120 km	300 km
Atomic Oxygen	0.08	0.73
Molecular Nitrogen	0.80	0.26
Molecular Oxygen	0.12	0.01

Table 6.2: Mass concentrations of the main constituents of the thermosphere at 120 km altitude and 300 km altitude during geomagnetic storm conditions.

Altitude	120 km	300 km
Atomic Oxygen	0.08	0.41
Molecular Nitrogen	0.82	0.57
Molecular Oxygen	0.09	0.02

6.5   Wall collision parameters

Next to the thermospheric conditions, satellite wall parameters and the relative velocity of the satellite also influence the aerodynamic coefficients of the satellite. For these parameters the uncertainty does not depend on the variability of the thermosphere, but rather depends on the lack of data for these parameters or mission design.

6.5.1 Energy accommodation coefficient

As explained before, the aerodynamic coefficients depend on the the way that the incoming particles hit the satellite surface and get re-emitted. The equation that describes the ratio of the velocity of re-emitted particles over the incoming particles is given in Equation 6.3.9. One of most important variables for this ratio is the the energy accommodation coefficient, α_E [March et al., 2019]. The energy accommodation coefficient contains information about the energy exchange of a particle with a satellite surface during collision [Pilinski et al., 2010].

α_E can be expressed by Equation 6.5.1.

$$\alpha_E = \frac{T_{inc} - T_{re}}{T_{inc} - T_{wall}}. \tag{6.5.1}$$

Where T_{inc} is the temperature of the particle before the collision with the satellite surface. T_{re} is the temperature of the particle after the collision with the surface and T_{wall} is the wall temperature of the satellite.

If α_E is close to zero it means that there is no kinetic energy lost during the collision. If the coefficient reaches one, it means that kinetic energy is lost due to the adjustment of the particle's temperature to the satellite surface temperature, which can also be referred to as "complete accommodation" [Moe and Moe, 2005]

The value of α_E depends on different factors, ranging from solar activity to gas composition Pilinski et al. [2010]. It is hard to know the exact value for α_E. However, it does have play a significant role in the aerodynamic acceleration modeling. This is why researchers like March et al. [2019] and Pilinski et al. [2016] are improving the estimations of this parameter by comparing it to experimental data or in-orbit data.

Moe and Moe [1969], Moe and Moe [2005], Hedin et al. [1973] and Offermann and Grossmann [1973] discovered, by analyzing data from orbiting pressure gauges and mass spectrometers, that at altitudes of 150-300 km the satellite surfaces are coated with absorbed atomic oxygen and its reaction products. Due to the coat of absorbed molecules, the incoming particles are adjusted by the thermal energy of the surface and re-emitted in a diffuse direction [Moe and Moe, 2005] [Saltsburg et al., 1967]. In this process they loose a lot of kinetic energy. On the other hand, if the incoming particles collide with a clean surface, they are re-emitted near a specular angle. The gas-surface model in between diffuse and specular is called quasi specular reflection. All three gas-surface models are represented in Figure 6.6
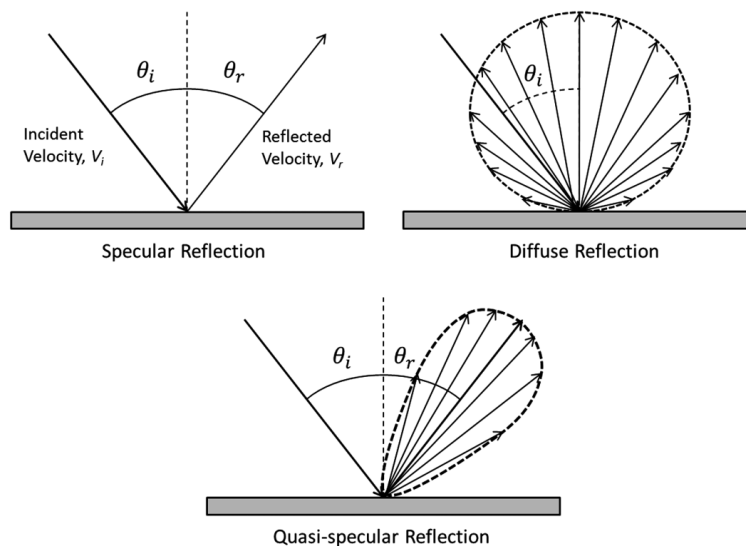

Figure 6.6: Illustration of different gas-surface interaction models, credits: Mehta et al. [2014].

It was found that for altitudes lower than 200 km $\alpha_E = 1$. For higher altitudes the accommodation coefficient would decrease, due to the reduction of absorbed atomic oxygen to the surface of the satellite. It is concluded that for this thesis, due to the low altitudes, $\alpha_E = 1$ and a diffuse gas-surface interaction model is chosen. The impact of this assumption will be tested in subsection 9.2.1.

6.5.2 Wall temperature

If a molecules collides with the surface of a satellite the molecule can acquire the wall temperature of the satellite. This influences the energy accommodation coefficient as described above and therefore the re-emittance of the particles. However, there is often no data available on the temperature of the satellite wall. This introduces an extra uncertainty in the calculation of the aerodynamic coefficients. Doornbos [2012] states that the sensitivity to T_{wall} is quite low in FMF. This can be substantiated by looking at the equation for the energy accommodation coefficient given in Equation 6.5.1, T_{wall} only has an influence if it is in the same order of magnitude as the incoming kinetic temperature, T_{inc}. However, $T_{wall} << T_{inc}$ [March et al., 2019], so it is expected that the sensitivity to this parameter is low in FMF.

Nevertheless, for Continuum Flow, CF, this difference can have a significant influence on the aerodynamic coefficients. In this case, the gas surrounding the wall is often assumed to be equal to the temperature of the wall. The difference between the temperature next to the wall and the temperature of the gas creates a thermal boundary layer [E. Mooij, 2019]. It can be expected that the sensitivity of the aerodynamic coefficients with respect the wall temperature for the transitional region between the FMF and CF, is somewhere in between aswell. In addition, it was found that the gas temperature of the lower thermosphere in the TF region, is much lower than at high altitudes. Therefore, T_{wall} is closer to T_{inc} and is expected to have more influence.

In chapter 9, the sensitivity to T_{wall} will be tested. For this study a nominal value of T_{wall} of 400 K will be assumed in agreement with March et al. [2019].

6.5.3 Satellite velocity

The relative velocity, V_r, of the satellite with respect to the thermospheric particles was assumed to be equal to the velocity of the incoming particles V_{inc}, as described in section 6.3. Equation 6.3.4 showed that V_r is used to calculate the speed ratio.

The satellite velocity depends on the orbit of the satellite. It is assumed that the location for which the aerodynamic coefficients are determined is the perigee of the satellite's orbit. Here the satellite is at its lowest altitude and thus encounters the highest density. For this thesis an apogee altitude of 2700 km is assumed and perigee altitudes of 120 and 300 km for the TF and FMF respectively, as was more thoroughly explained in chapter 3. This will result in a V_p at 120 km of 8455.9 m/s and a V_p at 300 km altitude of 8293.4 m/s. In section 11.1, the impact of the choice in apogee altitude is tested.

The rest of the incoming velocity of the particles, or the relative speed, V_{inc}, is due to he motion of the particles with respect to the satellite. Therefore, V_{inc} contains also the wind. The wind was analyzed in chapter 5. If the wind is in the same plane as the orbital velocity of the satellite, the total relative velocity is obtained by adding or subtracting the two together.

Chapter 7

Method

Due to the complexity of the lower thermosphere and the unavailability of theoretical expressions of this region, it is chosen to use a computational model to obtain the aerodynamic coefficients. The process of obtaining the aerodynamic coefficients of a satellite shape consists of two parts. First of all, the aerodynamic pressures and shears on the shape need to be modeled. This is done by PArallel Rarefied-gas Time-accurate Analyzer (SPARTA), more about this program can be found in section 7.1. Afterwards, from the pressures and the shape file the Aerodynamic coefficients can be calculated. This is further explained in section 7.2.

7.1 SPARTA

SPARTA was developed at Sandia National Laboratories, a laboratory from the Us Department of Energy (DOE). All information used for this section is found at `https://SPARTA.sandia.gov/`. The purpose of the program is to perform simulations of low-density gases in 2d or 3d by using a Direct simulation Monte Carlo (DSMC) code. It is possible to insert a 2d or 3d model into the simulation to calculate the pressures and shears on the surface. The code does not only include particle-particle collisions, but also surface-particle collisions. Since it is an open source tool and has been tested on other spacecraft, it is a good option to use for this thesis [Marín et al., 2019]. SPARTA is run on the student server of the faculty of Aerospace Engineering at the TU Delft. This section will explain the reference axis system that is embedded in SPARTA and the input script that is used to run simulations.

Reference system definition

The reference system used in SPARTA is the Aerodynamic reference frame (airspeed based). This means that the X-axis is defined along the velocity vector of the vehicle relative to the atmosphere. The stream is flowing with a velocity in the positive x direction. This means that if the satellite encounters the wind directly from upfront (α = 0° and β = 0°), the front of the satellite is directed in the negative x direction. Due to the wind directions and uncertainties in the attitude control, the satellite can encounter the stream of particles on an angle. This is simulated by turning the satellite by an angle of α or β with respect to the x axis. The angles were given in the explanation of the attitude of the satellite in section 3.2.

Input script

SPARTA can be run for many different options and simulation settings. To assign the right settings for the simulations that are of interest to this study, an input script is used. In this section the structure of the input script will be explained.

1. **Variable & loop definition:**
   In the beginning of the script the values for variables like T_{inf}, T_{sat}, ρ and the rotation angles that will be considered are defined. Since the shapes will be tested for various thermospheric conditions and flight angles, it is easy to make use of loops. In the beginning of the script the loops are labeled.

2. **Simulation parameter definition:**
   Next, the general settings (global and numerical) are given. Afterwards, the simulation box and grid are defined and generated.

3. **Insertion of the satellite model:**
   The geometry of the satellite shape (3D) is placed into the simulation box and rotated if necessary. The satellite shape is divided into triangles before inserting it as a mesh in SPARTA.

4. **Insertion of the gas mixture:**
   The properties of the gas mixture inside the simulation box are defined. First of all, the gas species and their properties are imported from an external file. Next, the total number density is given, as well as the relative velocity of the gas with respect to the satellite shape mesh and the gas temperature. In case of a mixture of multiple gas constituents the number density fractions need to be added as well. Finally an operation is added to the system that defines the flow of the gas.

5. **Collision model definition:**
   Then, the collision model is defined. In section 6.5, it was decided to assume completely diffuse collision between the surface and the gas particles. As an input of the diffuse collision model the satellite temperature and energy accommodation coefficient are given. In addition, since the focus of this study are the aerodynamic coefficients in the TF, the intermolecular collisions need to be turned on. There are two possibilities for the intermolecular collision models. Namely the variable hard sphere (vhs) model and the variable soft sphere (vss) model. The vss model is the updated version of the vhs model, in which the viscosity coefficients of the air species are taken into account [Koura and Matsumoto, 1992]. Among others, Morokoff and Kersch [1998] showed that the vss model is a better representation of the intermolecular collisions. Therefore in this thesis, vss is chosen. To specify the vss model, the vss model parameters of the species are loaded in from an external file.

6. **Output generation:**
   The outputs are generated by performing a certain number of runs and taking the average of the outcomes. The simulations of SPARTA use Monte-Carlo code. Which means that the gas particles are inserted in the simulation box in a random way. During every run new particles are added to the simulation box. When there are too little runs performed or the run time of every run is very short, the outcome of the simulation can change per simulation due to the randomness of the Monte Carlo. With increasing number of runs the randomness of the result decreases until convergence is met. The convergence can be checked in different ways. During the simulation, for every n runs, the number of particle-particle collisions and particle surface-collisions is printed. Convergence is met when these values stay almost constant with increasing runs. Another way of checking convergence is checking the results. If, after performing the exact same simulation, the results have big differences, the simulation has not converged yet. In order to get the most accurate results, the outcomes of the runs before convergence are not saved. After multiple trials, it was found that after 2000 runs it was certain that the results for all runs performed in this thesis have been converged with the simulation settings as proposed in section 8.4. After those 2000 runs, 3000 runs are performed for which the results are saved and the average is calculated.

   There are three types of outputs: surface, grid and figure. The surface output contains the pressures and shears per triangle of the satellite shape mesh in three directions. These outputs are given in a .txt file. Secondly, the grid output contains the number density per grid cell. This can be used to visualize the interaction of the surface and the flow. Finally, the figure shows the simulation box including the particles and the satellite model at the last time step.

7.2 Post-processing

From the pressure and shear per surface triangle, the aerodynamic coefficients can be calculated. This can be done for every satellite shape, every rotation angle and every speed ratio. To do this a post-processing Matlab script is written which uses the results of SPARTA as input.

The main aerodynamic coefficients for linear motion are the drag coefficient (C_D) and the lift coefficient (C_L). Both can be decomposed by a fraction and a pressure coefficient. For example, C_D can be decomposed in the pressure drag coefficient (C_{D_p}) and the friction drag coefficient (C_{D_f}). These coefficients can be calculated by Equation 7.2.1 and Equation 7.2.2

$$C_{D_p} = \frac{2p_{x_{overall}}}{A_{ref}\rho V_r^2} \tag{7.2.1}$$

$$C_{D_f} = \frac{2\sigma_{x_{overall}}}{A_{ref}\rho V_r^2} \tag{7.2.2}$$

Where ρ is the density of the gas around the satellite and V_r is the velocity of the satellite with respect to the gas. A_{ref} has been discussed before and is the reference area or affected area. Often this is assumed to be equal to the cross-sectional area of the satellite shape with respect to the flow. In this thesis, instead of assuming a value for A_{ref}, the total term of $C_D * A_{ref}$ is analyzed. $p_{x_{overall}}$ and $\sigma_{x_{overall}}$ are the total pressure in the x direction and the total shear in the x direction respectively. $p_{x_{overall}}$ is obtained by multiplying the pressure in the x direction onto every surface panel by the area of that panel and then summing all of them together. $\sigma_{x_{overall}}$ is calculated in a similar fashion. The equations are given in Equation 7.2.3 and Equation 7.2.4

$$p_{x_{overall}} = \sum_{i=m}^{n} p_{x_i} * A_i \tag{7.2.3}$$

$$\sigma_{x_{overall}} = \sum_{i=m}^{n} \sigma_{x_i} * A_i \tag{7.2.4}$$

Finally C_D is obtained by adding the pressure drag coefficient and shear drag coefficient together.

$$C_D = (C_{D_p} + C_{D_f}) \tag{7.2.5}$$

The lift coefficient is obtained in a similar way. This time the pressure and the shear components in the z direction are used as can be seen in the equations below.

$$C_{L_p} = \frac{2p_{z_{overall}}}{A_{ref}\rho V^2} \tag{7.2.6}$$

$$C_{L_f} = \frac{2\sigma_{z_{overall}}}{A_{ref}\rho V^2} \tag{7.2.7}$$

$$C_L = (C_{L_p} + C_{L_f}) \tag{7.2.8}$$

To investigate the influence of the various parts of the satellite: booms, body and wings, separately, every triangle needs to be labelled with the respective part to which it corresponds. This is done with the help of a collada file. The collada file includes the material information of every triangle. So when assigning three different materials for the three different satellite parts in Blender, the distinction can be made between the triangles. The surface mesh that is used as input for SPARTA do not contain material properties. The material properties are therefore not taken into account while generating the pressures and shears onto the satellite via SPARTA.

Chapter 8

Validation

To validate the previously explained method, in this chapter, the results obtained by this method will be compared to analytical solutions. As previously mentioned, analytical solutions exist for simple geometries in FMF. In section 8.1 the result of a flat plate will be compared to the closed-form solutions of Sentman with various angles of attack. In section 8.2 the results of a cylinder with different sizes will be compared to the results of Mehta et al. [2015] for a range of densities to validate for higher densities at lower altitudes as well. These validations are performed with the assumption of a gas composition consisting only of atomic Oxygen. In section 8.3, the program is validated for inserting a mixed gas of various constituents into the simulation. Next, in section 8.4, a sensitivity analysis of the simulation settings is performed. Finally in section 8.5, the choices for the focus of this thesis are further discussed.

8.1 Comparison with Sentman equations

The Sentman equations have been explained in section 6.3. To get the total aerodynamic coefficient, the weighted sum of the aerodynamic coefficients corresponding to the major constituents of the local atmosphere should be calculated. At high altitudes (>300 km) the main constituent (80% mass concentration) of the atmosphere is atomic Oxygen. To simplify, for this validation it is therefore assumed that atomic Oxygen is the only constituent in the gas surrounding the flat plate. The flat plate as described in Figure 6.2, starts with an orientation perpendicular to the stream of particles and to the drag vector at $\theta = 0°$. It is expected that the drag at this moment is the highest. θ is then increased until the the flat plate is aligned to the stream at $\theta = 90°$.

The analytical solution is compared to the SPARTA input. Since it is not possible to input an infinitely thin plate into SPARTA, the plate created in Blender is given a thickness of $0.1\ mm$. The plate is a perfect square of 1 by 1 meter. The other input parameters are:

Table 8.1: Input parameters for Sentman validation.

Parameter	Nominal value	unit
T_{wall}	300	K
T_{inf}	1000	K
s	7.45	$-$
α	1	$-$
m	16e-3	kg/mol
R_{gas}	519.65	$J/(K*kg)$
V_r	7600	m/s

In Figure 8.1, the drag coefficient (C_D) and the lift coefficient (C_L) are given as a function of θ. The continuous lines are the analytical solutions of the respective aerodynamic coefficient. The dots are the computed aerodynamic coefficient by SPARTA with the same settings as the analytical solution. As can be seen, the analytical solution matches with the computation from SPARTA until 90°. At that point, the simulation by SPARTA results in a higher value. The explanation of this is that the analytical solution assumes a flat plate, whereas the SPARTA simulation is run for a flat plate with a certain thickness. Because of this, the drag coefficient is slightly higher for the result of SPARTA compared to the analytical solution at 90°. Another conclusion that can be drawn from this figure is that the drag coefficient is much higher than the lift coefficient.
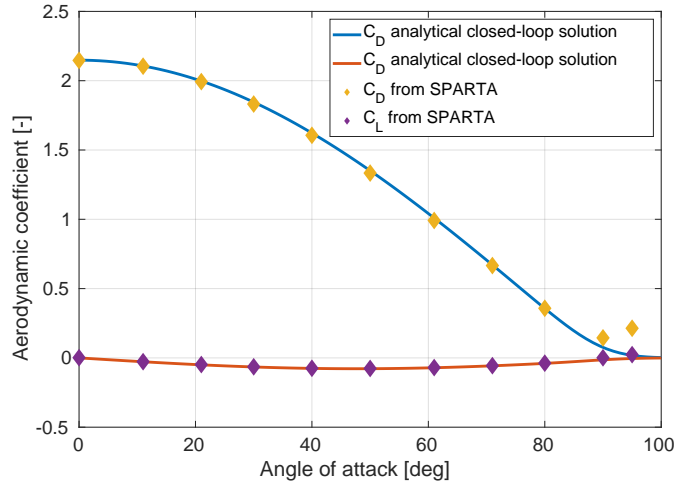

Figure 8.1: Comparison between SPARTA results of a flat plate and closed-form equations from Sentman [1961] with respect to angle of attack.

8.2 Result comparison with Mehta et al. [2014]

Now that the program is validated for the FMF regime, it still needs to be validated for higher densities as can be found in the TF regime. Another validation is performed by comparing the results with results by Mehta et al. [2014]. This paper computed drag coefficients with DSMC simulations and compared these to closed-form solutions to study the effects of different gas-surface interaction models. The DSMC results are compared with the closed-form solutions for different densities. It should be noted that in the DSMC results, the intermolecular collisions are taken into account, whereas this is not included in the theoretical model. The simulation is performed for a flat plate from 1 by 1 meter and for two cylinders. The equations used by Mehta et al. [2014] are a variation on the Sentman equation described above [Sentman, 1961] [Pilinski et al., 2010]. The closed-form solution for the flat plate and the cylinder are given in Equation 8.2.1 and Equation 8.2.2 respectively.

$$C_{D,fp} = (2 + \frac{1}{s^2})erf(s) + \frac{2}{\sqrt{\pi}s}e^{-s^2} + \frac{\sqrt{\pi}}{s}\sqrt{\frac{T_{re}}{T_{inf}}} \tag{8.2.1}$$

$$C_{D,cy} = (2 + \frac{1}{s^2})erf(s) + \frac{2}{\sqrt{\pi}s}e^{-s^2} + \frac{\sqrt{\pi}}{s}\sqrt{\frac{T_{re}}{T_{inf}}} + \frac{4}{\sqrt{\pi}}\frac{L}{D} \tag{8.2.2}$$

Since α_E is assumed to be equal to 1, following Equation 6.5.1, the temperature of the reflected particle, T_{re} can be assumed equal to the wall temperature of the satellite, T_{wall}.

The length/diameter (L/D) ratio of the cylinders are 1 and 3 respectively. The simulation input parameters are given in Table 8.2.

Table 8.2: Input parameters for Mehta validation.

Parameter	Nominal value	unit
T_{wall}	300	K
T_{inf}	1100	K
α	1	$-$
m	16e-3	kg/mol
R_{gas}	519.65	$J/(K*kg)$
V_r	7500	m/s

The results are given in Figure 8.2. Here it can be seen that the results of SPARTA agree with the closed-form solutions for number densities of atomic Oxygen lower than 1e16 $/m^3$. With increasing density beyond this point the C_D decreases. This agrees with Mehta et al. [2014]. Due to the increased density the particle-particle collisions start to play a role. With other words, the TF has begun. These collisions are not taken into account in the closed-form solutions. In this case, due to the mutual particle collisions, the number density close to the surface is lower such that the pressure on the surface is lower. The results of the SPARTA simulations seem to agree with the DSMC simulations of Mehta et al. [2014] until 1e18 $/m^3$ for the two cylinder models. Afterwards the results are significantly different. A number density of atomic Oxygen equal to 1e18 $/m^3$ corresponds to a total density of 2.7e-8 kg/m^3, which corresponds to 120 km, which was the altitude of interest of this thesis. The qualitative behaviour of the drag coefficient is for both simulations the same up until 1e18 $/m^3$.
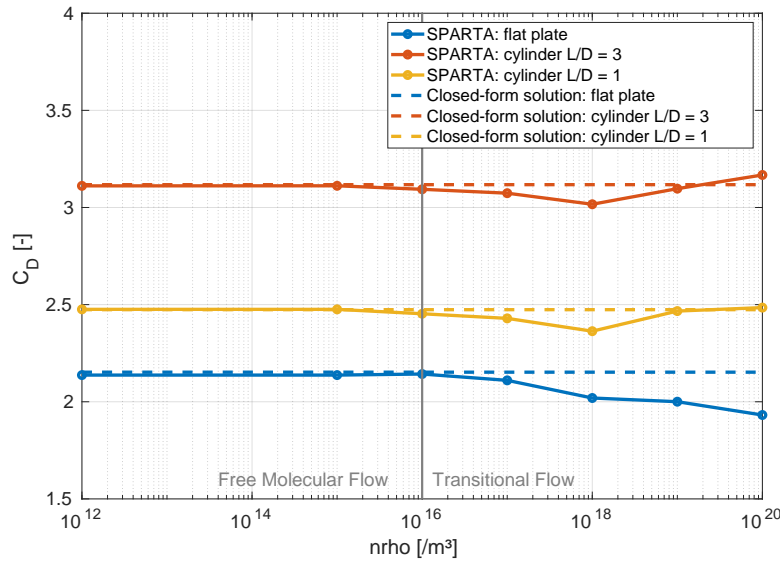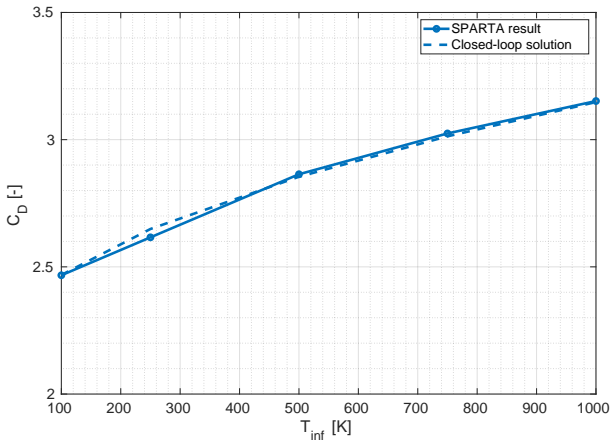

Figure 8.2: SPARTA results for C_D compared to closed-form solutions at various number densities. Around the number density of atomic Oxygen of 1e16 $/m^3$ the Free Molecular becomes the Transitional Flow.

(a) With respect to T_{inf}.
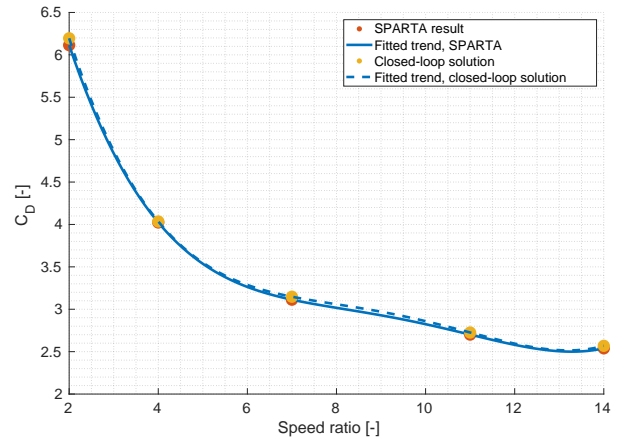
(b) With respect to speed ratio.
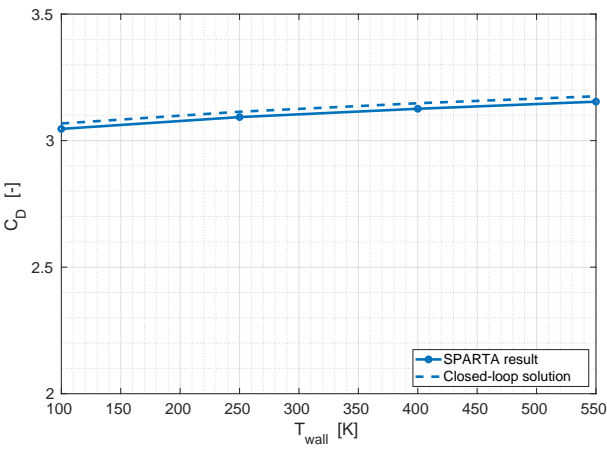
(c) With respect to T_{wall}.

Figure 8.3: Comparison of the SPARTA results with closed-form solution of C_D for the cylinder model l/D = 3 and nrho = $1e12/m^3$.

Mehta et al. [2014] does not only validate for density but also uses the closed-form solution to validate the program for T_{inf}, T_{wall} and s at a low number density (nrho = 1e12 $/m^3$). In Figure 8.3a and Figure 8.3b the comparison between SPARTA and the closed-form solution with respect to T_{inf} and s can be found respectively. In Figure 8.3c the comparison with respect to the wall temperature of the satellite can be found. The maximum deviation between the closed-form solutions and the SPARTA outcomes is equal to 0.038. since this around a 1% uncertainty it is deemed negligible.

8.3   Validation for composition existing of multiple constituents

The above described validations are performed assuming atomic Oxygen as the only constituent present in the atmospheric composition. However, in reality this is not the case. There are two possibilities of modeling the aerodynamic coefficients for a mixed thermosphere. First of all, it is possible to define the mixture by defining the number density fraction of all the constituents in the SPARTA input script as explained in section 7.1. Secondly, when looking at the analytical expression in section 6.3, it can

be found that the composition of the gas mixture only influences the aerodynamic coefficients via the speed ratio. Following the analytical method, it would therefore be possible to "trick" the speed ratio. To do this, the speed ratios for the main constituents of the gas mixture are calculated. Then, instead of changing the speed ratio in SPARTA by changing the composition, the relative satellite velocity is changed. The composition input in SPARTA is kept constant on 100% atomic Oxygen, throughout the various simulations. This way, the aerodynamic coefficient are calculated separately for every constituents of the gas mixture while keeping the total density the same. The total $C_D * A_{ref}$ is calculated by taking the weighted average based on the mass concentrations in the gas.

This method can be used to save many runs when for example testing the sensitivity to the composition fractions. However, for runs where the composition is kept constant, it is faster to input the mixture fractions in the SPARTA input script, since then only one run has to be performed.

The two methods are compared with respect to density and the attitude angles: side-slip angle (β) and angle of attack (α). First of all, multiple runs are performed with varying densities. The rest of the variables (T_{sat}, T_{inf}, V_{sat} and the composition) are kept constant throughout the cases. The result is given in Figure 8.4, where *mix* stands for the mixed gas input in SPARTA and *s trick* stands for the method where 100% atomic Oxygen is used as input for the gas composition in SPARTA and the speed ratio is changed by V_{sat}. It can be concluded that for the FMF densities, up until a density of 2.7e-10 kg/m^3, (corresponding to a number density of 1e16 $/m^3$ atomic Oxygen) there is a negligible difference ($< 1\%$). With increasing density the difference between the total $C_D * A_{ref}$ of the two methods is increasing. When looking carefully, the uncertainty is mainly present in the frictional component. The maximum uncertainty is 2.8%.
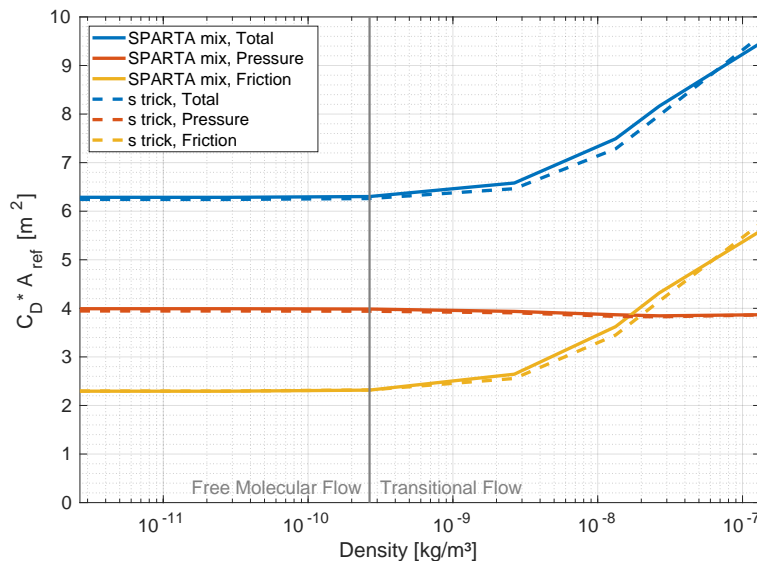
Figure 8.4: $C_D * A_{ref}$ of the standard satellite shape in m^2 with respect to gas density. The result of the speed ratio "trick" (dotted line) is compared to the result of inserting the number density concentrations in SPARTA (continuous line). The composition for which both methods are compared is equal to the composition at 120 km altitude as described in subsection 6.4.3 and is constant with density.

Next, the runs are performed with respect to the α and β. The drag coefficient is decomposed in the frictional and pressure component. In Figure 8.5a and Figure 8.5b the results are given for the FMF. The results overlap completely for all angles and therefore is this method verified for the FMF. It can be noted that the value of $C_D * A_{ref}$ at $\alpha = \beta = 0°$ in Figure 8.5 does not agree with the value found in

Figure 8.4, for the FMF densities. This is due to the different composition inputs. In Figure 8.5 the FMF mass concentrations are used and in Figure 8.4 the TF mass concentrations are used for all densities.

In Figure 8.6, the TF mass concentrations are used as well. Here it can be seen that for $\beta = \alpha = 0°$, the value for $C_D * A_{ref}$ approximately agrees with the value shown in Figure 8.4 for a number density of $1e18$ $/m^3$. The difference between the results of of using the speed ratio "trick" or inserting the values for the number density concentration directly in SPARTA, is larger for the TF as for the FMF. This agrees with the conclusions based on Figure 8.4. The induced error does not increase significantly with angle of attack or side-slip angle.

(a) With respect to angle of attack.

(b) With respect to side-slip angle.

Figure 8.5: Comparison of $C_D * A_{ref}$ of the standard satellite shape obtained by using s 'trick': Inserting atomic Oxygen in SPARTA and performing a speed ratio correction, and $C_D * A_{ref}$ obtained by inserting all constituents of gas mixture for Free Molecular Flow regime in SPARTA. Note the difference in the y-axis of (b) with respect to (a).

(a) With respect to angle of attack.
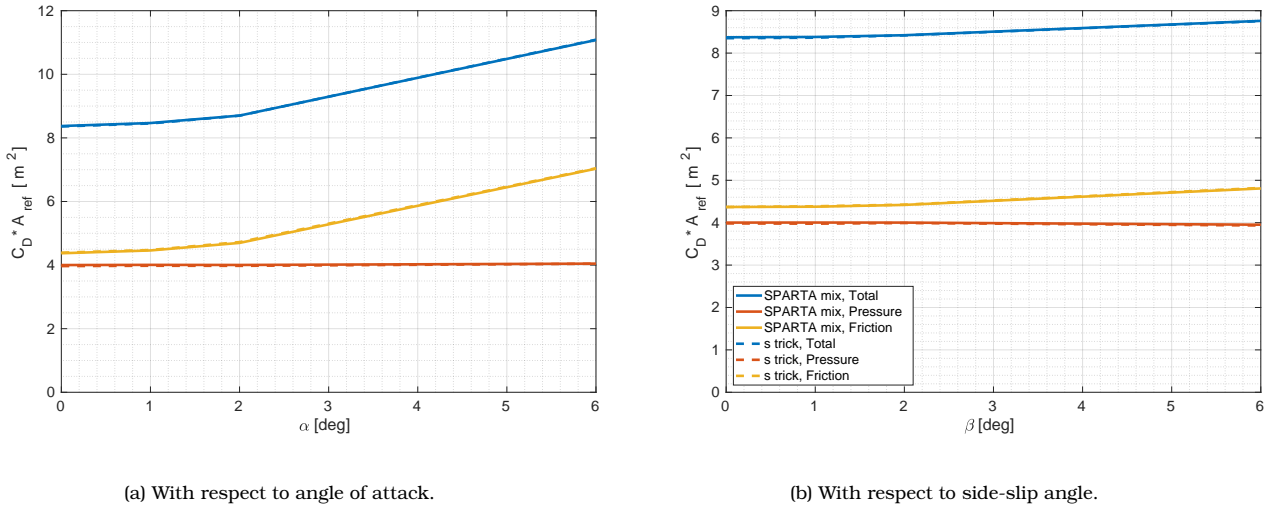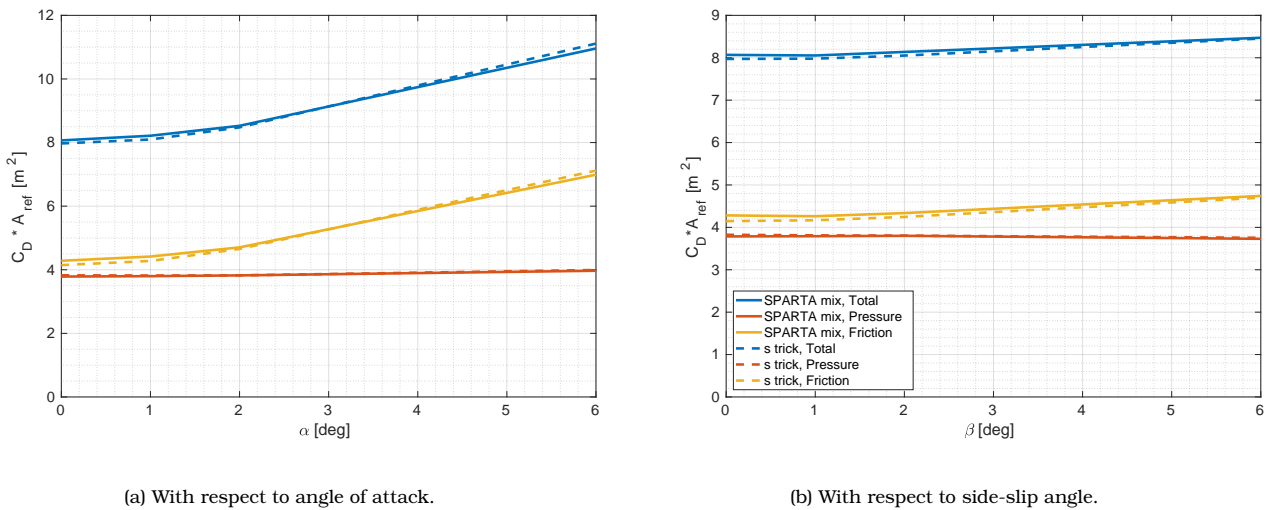
(b) With respect to side-slip angle.

Figure 8.6: Comparison of $C_D * A_{ref}$ of the standard satellite shape obtained by using s 'trick': Inserting atomic Oxygen in SPARTA and performing a speed ratio correction, and $C_D * A_{ref}$ obtained by inserting all constituents of gas mixture for Transitional Flow regime in SPARTA. Note the difference in the y-axis of (b) with respect to (a).

8.4   Sensitivity analysis of the simulation settings

The computations performed by SPARTA can be very time consuming. To decrease the computation time, some simulation settings can be tweaked. The runtime is mostly affected by the ratio of physical particles to simulation particles (fnum) and the timestep. The domain size and gridsize also need to be defined. The simulation parameters need to be changed carefully, because they also have an influence on the convergence of the result. In general, the more simulation particles the longer it takes. At the same time, the threshold of particles that is needed to converge should be kept in mind. This is why a sensitivity analysis is performed in the previously mentioned order. The input shape of the sensitivity analysis is the standard satellite shape, the input parameters are given in the table below. These values are the nominal values of the input parameters as decided upon in chapter 6.

Table 8.3: Nominal values for input parameters.

Parameter	Nominal value		unit
	FMF	TF	
Altitude	300	120	km
T_{wall}	400	400	K
T_{inf}	1000	400	K
α	1	1	$-$
m	16e-3	16e-3	kg/mol
R_{gas}	519.65	519.65	$J/(K*kg)$
V_r	8293.4	8455.9	m/s
$nrho$	1e14	1e18	$/m^3$

The C_L value is close to zero and therefore extremely sensitive. This will be further elaborated upon in section 8.5. The focus of this section will be on the drag coefficient. For all simulation settings, a table is given with a summary of the result of the sensitivity analysis. For simplicity a complete atomic Oxygen atmosphere is assumed for this sensitivity analysis.

Fnum sensitivity analysis

fnum is the ratio physical particles to simulation particles. By increasing the value of fnum, the number of simulation particles is decreased, therefore the computation will run faster. However, when reducing the number of simulation particles too much, the result might not converge. Various runs are performed with varying the value for fnum. The results for $C_D * A_{ref}$ for various fnum values are shown in Figure 8.7a for the TF regime and the FMF regime.

As can be seen from the two different x-axes, the orders of magnitude for fnum are different for the FMF regime and the TF regime. This is due to the difference in number density. When fnum is kept constant and the number density increases that means that the simulation particles decrease. When the simulation particles are reduced too much, the result is not able to converge anymore. That is why the value for fnum increases linearly with the number density. Since the number density generally increases with approximately 4 orders of magnitude when going from the FMF regime to the TF regime, fnum also increases by 4 orders of magnitude. For the nominally chosen density at 300 km, the fnum chosen is equal to 0.5e12. For fnum values lower than 1e12, the maximum uncertainty was found to be equal to 0.11%, which can be deemed negligible. For the nominal defined value of density in the TF regime at 120 km altitude, a value of 0.3e16 is chosen for fnum. The maximum variation below 0.5e16 is 0.23%. When, in this thesis, a different value than the nominal density is used for the simulation, the fnum is changed accordingly. In general, the FMF simulations run faster due to the simplification of not having any intermolecular collisions.
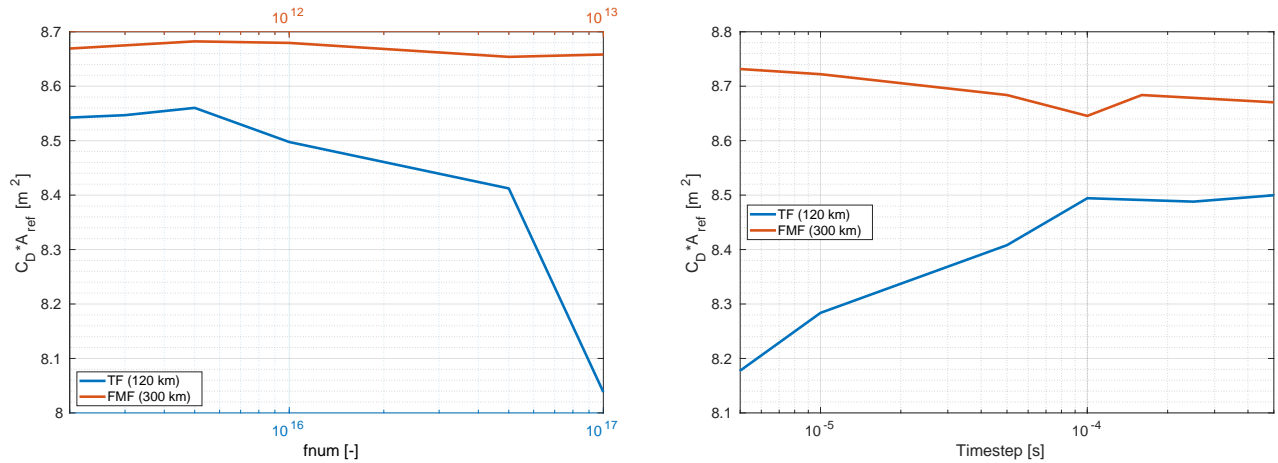
(a) fnum sensitivity of $C_D * A_{ref}$ of the standard satellite shape in TF (blue axis) and FMF (red axis).

(b) Timestep sensitivity of $C_D * A_{ref}$ of the standard satellite shape in TF and FMF.

Timestep sensitivity analysis

Because the results are saved every timestep, the timestep should be large enough in order for enough particles to hit the surface. In addition, the timestep together with the number of runs determine the total run time of the simulation. When making the timestep too small, the total run time of the simulation is too short, such that too little amount of particles have entered the simulation and collided with the satellite mesh, to converge. Making the timestep larger will therefore also increase the total run time. $C_D * A_{ref}$ of the satellite has been tested for multiple timesteps and the results are given in Figure 8.7b for both the FMF and the TF regime.

It can be seen that between a timestep of 1e-4 s and 0.5e-3 s, the value for $C_D * A_{ref}$ is nearly constant. The largest deviation for $C_D * A_{ref}$ in that range is 0.03 m^2 for the FMF and 0.01 m^2 for the TF, this is less than 1% difference for both regimes. In addition, the values for the gas-surface collisions and the intermolecular collisions that is printed in the output file of the program has converged as well. It can therefore be concluded that the timestep should be within this region. It has been decided to use a timestep equal to 0.16e-3 s for both the TF simulations at 120 km as the FMF simulations at 300 km altitude.

Domain sensitivity analysis

The domain describes the size of the box in which the simulation takes place. The domain needs to be big enough in order for the shape to fit in. Very large domains on the other hand could increase the simulation time. However, when testing the simulation for various domain sizes the difference in the simulation time was found to be insignificant. Nevertheless, the domain sizes are tested on convergence. The results of the sensitivity analysis, given in Table 8.4, show that the value for $C_D * A_{ref}$ changes slightly when increasing the domain size. The change is still below 1% which can be subscribed to simulation errors. For the remaining simulations of this thesis, nominally the domain size of 10 m in all directions is used. When variations of the satellite shape are tested that are larger than the domain size of 10, the domain size of 12 is used.

Table 8.4: Domain sensitivity results.

	Domain size in x,y,z [m]			Max variation	% difference
FMF	8	10	20		
$C_D * A_{ref}$ [m^2]	8.67	8.65	8.70	0.05	**0.58**
TF	8	10	12		
$C_D * A_{ref}$ [m^2]	8.50	8.55	8.56	0.06	**0.71**

Gridsize sensitivity analysis

The gridsize determines the number of points that are in the domain. The results of $C_D * A_{ref}$ in the TF regime and the FMF regime are given in Table 8.5. It can be found that the gridsize does not matter within the range given in the table. There is a zero percent difference. In addition, the running time did not change significantly depending on the gridsize. Therefore it was chosen to use 100 as gridsize in all directions. It should be noted however, that the results of $C_D * A_{ref}$ for the various gridsize inputs are slightly different from the results of $C_D * A_{ref}$ stated in the results of previous sensitivity analyses. The difference in $C_D * A_{ref}$ is 0.12 which is a bit more than 1%. This is can be deemed negligible.

Table 8.5: Gridsize sensitivity results.

	Gridsize [#]			Max variation	% difference
FMF	50	100	150		
$C_D * A_{ref}$ [m^2]	8.66	8.66	8.66	0.00	**0.00**
TF	100	150	200		
$C_D * A_{ref}$ [m^2]	8.62	8.62	8.62	0.00	**0.00**

8.5 Explanation of the research focus

The focus of this research is on the C_D times the reference area, $C_D * A_{ref}$. The reason for this is that the drag equation contains this product. In addition, parameters often influence both C_D and A_{ref}. To obtain the affected area, also shadowing should be taken into account. This makes it complicated. In some studies A_{ref} is chosen to equal to 1 as simplification, even though the affected area is bigger or smaller. Then, when calculating the drag, $A_{ref} = 1$ is used again. This approach has also been taken in this thesis. However instead of stating the reference area as 1, the reference area stays in the term. An example, of the real C_D without A_{ref} is given in Figure 8.8. It can be seen that the values are smaller due to the division by the total reference area equal to $1.858 \ m^2$. These values are closer to the expected values of a satellite, for example GOCE was found to have a drag coefficient of approximately 3.15 for $\alpha = \beta = 0°$ [Geul et al., 2017].
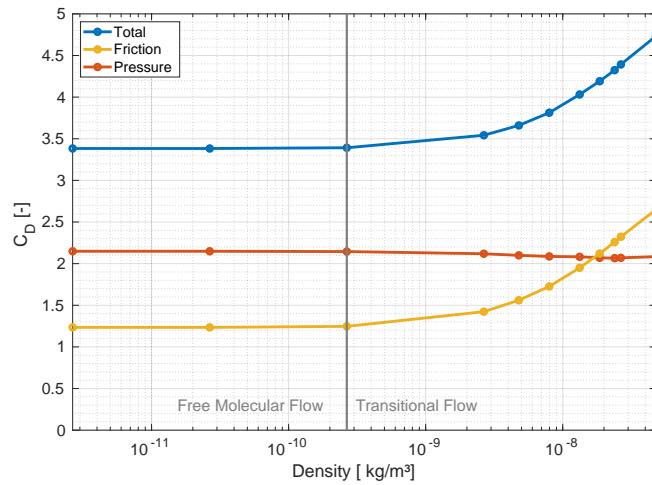
Figure 8.8: Drag coefficient [-] with respect to density for a affected area equal to 1.858 m^2 for the standard satellite shape, including wings and booms, at $\alpha = \beta = 0$.

In addition, in this thesis the focus lies on the drag coefficient, and not on the lift coefficient. The reason for this is that the standard satellite shape and its variations are tested for an angle of attack of zero and for a roll angle of either $0°$ or $90°$. In these cases, hardly any lift is generated. Therefore, no conclusions can be drawn on the influence of the thermospheric variability or wind on the lift. An example is given in Figure 8.9, where the lift coefficient (times the reference area) is given for various densities. The lift coefficient is so small that it is subjected to simulation errors, especially at higher densities. No clear conclusions could be drawn from this. Similar results were found for the lift coefficient during the sensitivity studies with respect to the thermospheric parameters and the wind. Therefore, in the remainder of this thesis only the drag coefficient will be analyzed.

Figure 8.9: $C_L * A_{ref}$ for different densities for the standard satellite model at $\alpha = 0°$, $\beta = 0°$.

Part IV
Results

Chapter 9

Sensitivity study results of the input parameters

From the theoretical background in chapter 6, it was found that the input parameters that determine the thermospheric conditions are extremely variable. In order to analyze the satellite aerodynamics in the TF at 120 km altitude, and compare it to the FMF at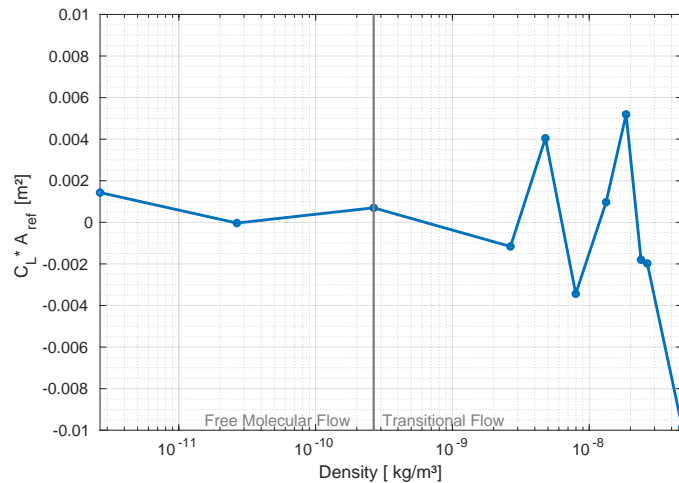 300 km altitude, nominal values for the thermospheric parameters for both altitudes were chosen. The nominal values for the parameters and the range found in chapter 6 are summarized in Table 9.1 and Table 9.2 for the TF and FMF respectively.

In this section the sensitivities of $C_D * A_{ref}$ to the parameters describing the thermospheric conditions and the gas-wall interaction are tested in section 9.1 and section 9.2 respectively. The thermospheric conditions vary with altitude. The gas-wall interaction parameters, T_{wall} and α, on the other hand are assumed to be constant.

To test the influence of each parameter individually, one parameter is changed within the range given in the tables below, while keeping the other parameters fixed. It is important to note however, that the thermospheric conditions are highly interdependent. For example, when the thermosphere heats up due to energy coming from solar radiation or geomagnetic storms, the density increases. If the density increases the thermosphere inflates and the upper boundary of the thermosphere increases. Because of the relatively high density, there are more intermolecular collisions present, which results in a more molecular atmosphere as was explained in subsection 6.4.3. It is therefore unlikely that in reality only one parameter will change. Nevertheless, this method is important to understand the contribution of every parameter individually.

The sensitivity of $C_D * A_{ref}$ can be characterized by the Sensitivity Index (S_I) [Hamby, 1994]. S_I is defined by Equation 9.0.1.

$$S_I = \frac{(C_{D,max} * A_{ref} - C_{D,min} * A_{ref})}{C_{D,ref} * A_{ref}} \tag{9.0.1}$$

$C_{D,ref}$ is equal to the result of the simulation performed with the nominal values for the thermospheric parameters for each altitude and the standard satellite shape. It is expected that since the thermospheric parameters and the gas-wall interaction parameters do not influence the attitude of the satellite, that A_{ref} does not change throughout the cases.

It should be noted that in Table 9.1 and Table 9.2 no values for the composition are given. To test the sensitivity of $C_D * A_{ref}$ with respect to composition, the simulation is run once with a composition corresponding to geomagnetic quiet time (GQT) and once to a composition corresponding to high geomagnetic activity (HGA). The values for the mass concentrations of both cases are given in the respective, subsection 9.1.3. The mass concentrations for GQT are used as the nominal values.

Table 9.1: Nominal values and sensitivity range of input parameters at 120 km.

Parameter	Nominal value	Lower limit	Upper limit	unit
T_{inf}	400	300	600	K
ρ	2.66e-8	4.78e-9	4.78e-8	kg/m^3
Composition	GQT	GQT	HGA	$-$
T_{wall}	400	200	600	K
α	1	0.9	1	$-$

Table 9.2: Nominal values and sensitivity range of input parameters at 300 km.

Parameter	Nominal value	Lower limit	Upper limit	unit
T_{inf}	1000	500	1600	K
ρ	2.66e-12	2.13e-12	2.66e-10	kg/m^3
Composition	GQT	GQT	HGA	$-$
T_{wall}	400	200	600	K
α	1	0.9	1	-

9.1 Sensitivity to thermospheric conditions

As explained in section 6.4, the thermospheric conditions vary with time, location and geomagnetic activity. Therefore, in this section the sensitivity of the drag coefficients to the variability of the parameters that describe the thermospheric conditions is researched.

9.1.1 Gas temperature

First of all, the sensitivity of the satellite's drag coefficients with respect to the gas temperature surrounding the satellite is examined. In Figure 9.1a and Figure 9.1b the $C_D * A_{ref}$ with respect to the surrounding temperature is given for the TF altitude of 120 km and and the FMF altitude of 300 km respectively. It can be seen that for both cases the total $C_D * A_{ref}$ is increasing with temperature. When decomposing the total $C_D * A_{ref}$ in the frictional and pressure component it can be seen that the increase in the total $C_D * A_{ref}$ is due to the increase in frictional drag. This can be explained when going back to the equations in section 6.3. Here it can be seen that the gas temperature influences the most probable thermal speed. If the gas temperature increases the most probable thermal speed also increases. This results in a lower speed ratio. When the speed ratio decreases, practically it means that the particles have more chances to hit the satellite's side surfaces and therefore the frictional component of the drag increases. It is interesting to note that even though the analytical expressions assume FMF, this relation between temperature increase and $C_D * A_{ref}$ increase can also be found in the TF.

In Figure 9.2, the contributions of the different parts of the satellite are shown. Here it can be seen that the gas temperature variation mostly influences the drag coefficient of the wings. This can be explained by the fact that the wings have the biggest ratio of side area with respect to frontal area and therefore relatively more frictional drag than the other parts. Since it was found that the gas temperature mainly effects the frictional drag, the $C_D * A_{ref}$ of the wings is most subjective to the gas temperature change. In addition, it can seen that the $C_D * A_{ref}$ of the body increases slightly with temperature. This is better visible for the FMF case than for the TF case. The $C_D * A_{ref}$ of the booms stay constant independent of the temperature or flow regime.

When comparing the nominal case in the Paraview image given in Figure 9.3 with the case with a higher temperature in Figure 9.4a, the conclusions drawn before are visualized. The number density above and below the wings is slightly higher, which is shown by a bright green color, due to the higher temperature. This increases the frictional component of both the wings and the body. The area of the

wings that is affected is larger and therefore a larger increase can be found for the wings. Behind the wings a shadowing region can be observed, colored very dark blue, which corresponds to a very low number density.

(a) In Transitional Flow.

(b) In Free Molecular Flow.
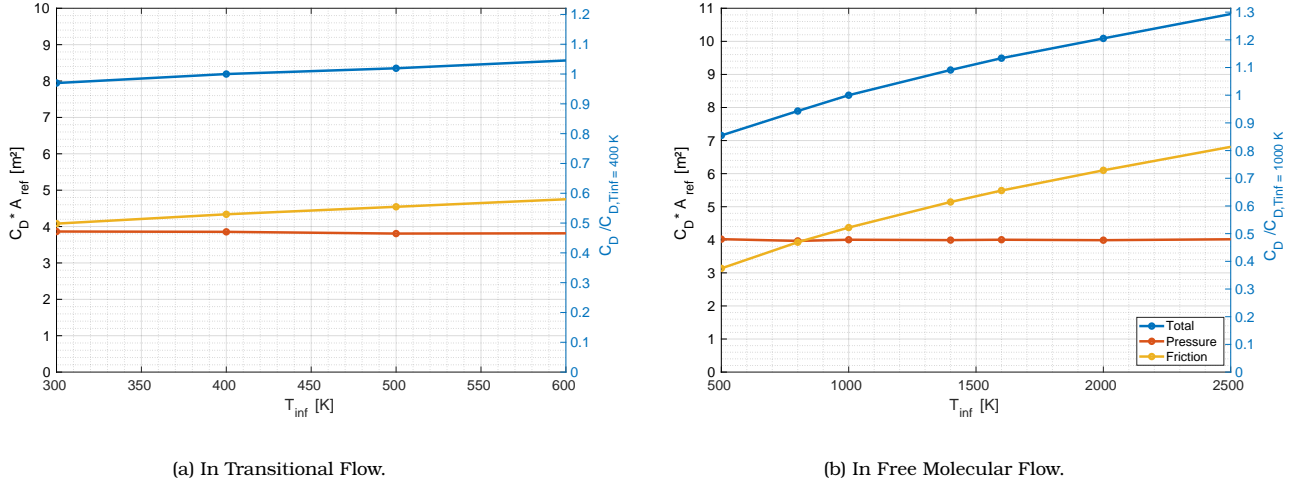
Figure 9.1: Sensitivity of total C_D, frictional $C_D * A_{ref}$ and $C_D * A_{ref}$ due to pressure with respect to T_{inf}.

(a) In Transitional Flow.

(b) In Free Molecular Flow.
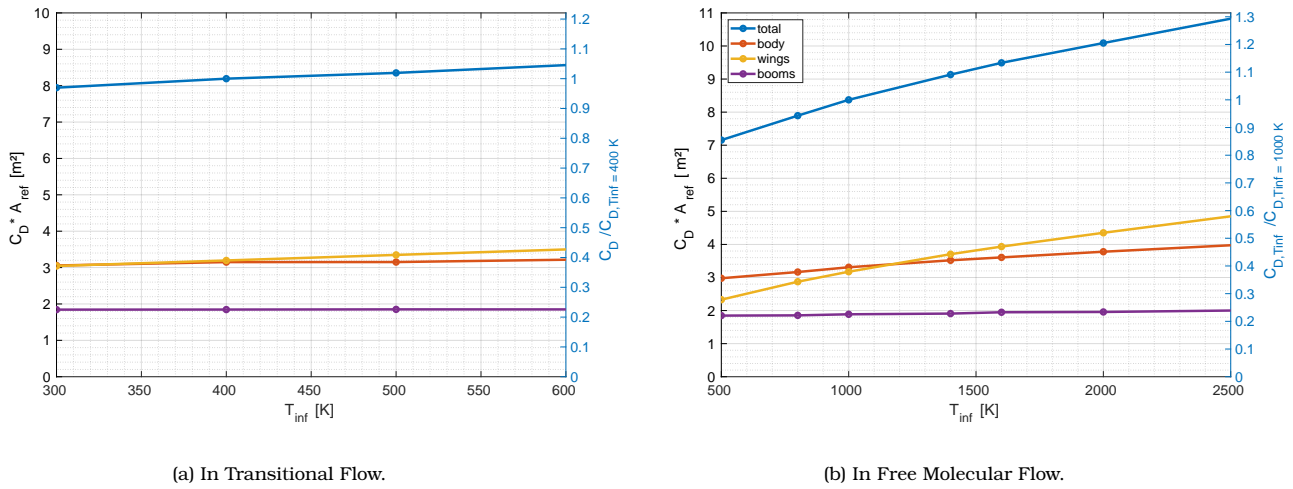
Figure 9.2: Sensitivity of $C_D * A_{ref}$ with respect to T_{inf} for all satellite parts.

The sensitivity index of the $C_D * A_{ref}$ to the variability of the gas temperature is equal to 0.093 for the TF and 0.28 for the FMF. This means that for the TF, a 10% difference in $C_D * A_{ref}$ due to T_{inf} variability can occur. For the FMF this is almost 30%.

Even though, the blue lines in Figure 9.2 are not completely linear, it is interesting to make an estimation of the increase of $C_D * A_{ref}$ per 200 K change for altitude cases. When looking at the right y-axis the change in $C_D * A_{ref}$ with respect to the nominal value can be found. Since A_{ref} is assumed to stay constant throughout the temperature cases, it cancels out. For the TF altitude at 120 km, a change of 100 K in temperature, results in a change of approximately 0.2 m^2 ($\pm$ 2.5%) in $C_D * A_{ref}$. At the FMF altitude of 300 km, the change between 1000 and 1600 K is 1.12 m^2 ($\pm$ 15%). This results also in an

average of 2.5% increase of the nominal value for an increase of T_{inf} per 100 K. From this it could be concluded that there is a general trend visible for the dependency on T_{inf} for a given shape, independent of the altitude and other thermospheric conditions. However, since these are only two test cases, more cases of thermospheric conditions should be tested in order to set it in stone.
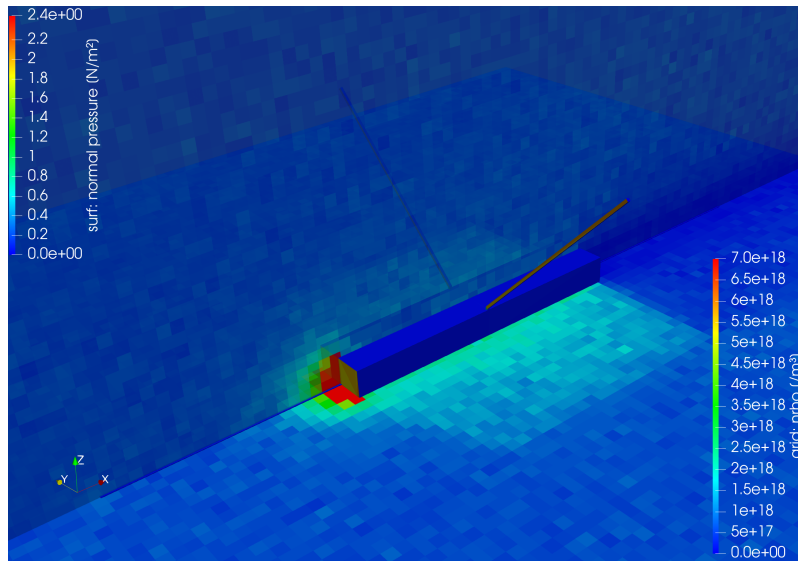
Figure 9.3: The standard model in the flow made in Paraview, for the nominal values of the thermospheric conditions in the TF at 120 km altitude. The colors in the grid represent the total number density $[/m^3]$, the colors on the satellite surface represent the normal pressure $[N/m^2]$.
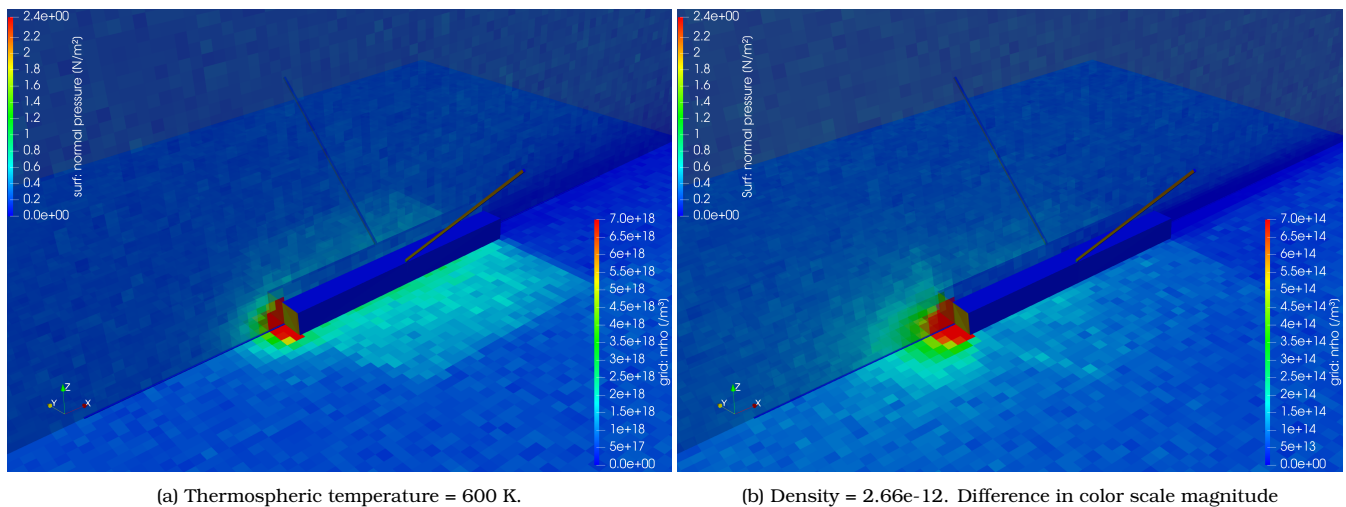
(a) Thermospheric temperature = 600 K.

(b) Density = 2.66e-12. Difference in color scale magnitude

Figure 9.4: The standard model in the flow made in Paraview, for the nominal values of the thermospheric conditions in the TF at 120 km altitude, with variations of temperature (a) and density (b). The colors in the grid represent the total number density $[/m^3]$, the colors on the satellite surface represent the normal pressure $[N/m^2]$.

9.1.2 Gas density

Just like the temperature, the density of the thermosphere is highly variable. It was found in section 6.4 that in the FMF the gas density does not influence the aerodynamic coefficients due to the absence of intermolecular collisions. However, in the TF, the density does have an influence. The variability for the density at 120 km altitude was found to be between 0.5e-8 kg/m^3 to 5e-8 kg/m^3.
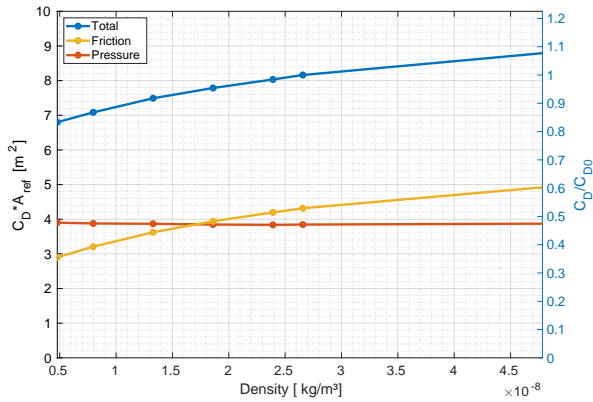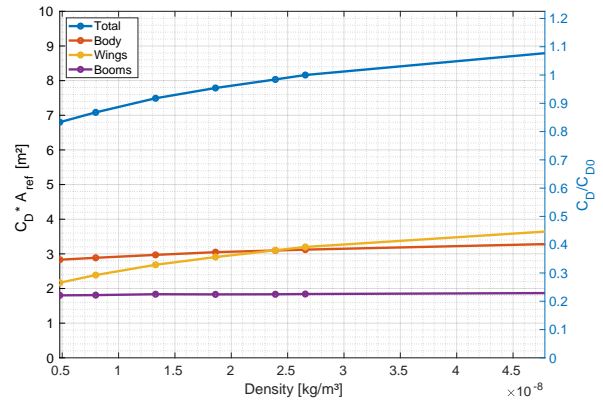
(a) For all drag coefficient components.   (b) For all satellite parts.

Figure 9.5: Sensitivity of $C_D * A_{ref}$ to density for the TF case at 120 km altitude.

The results of the sensitivity of $C_D * A_{ref}$ with respect to this density variability are given in Figure 9.5a. It is interesting to note that the density mainly influences the frictional component of the drag coefficient rather than the pressure component. The pressure component is slowly decreasing, while the frictional component is increasing. Above a density of 1.7e-8 $/m^3$, the frictional component is the biggest contributor to the total drag coefficient. When decomposing the $C_D * A_{ref}$ with respect to the different satellite geometry parts, in Figure 9.5b, it can be found that the solar panel wings wings are responsible for the large increase of the $C_D * A_{ref}$ when increasing the density. This can, just as for the sensitivity to the gas temperature, be subjected to the relatively large wing areas, which induce frictional drag. The $C_D * A_{ref}$ of the body is slightly increasing with density and the $C_D * A_{ref}$ of the booms is constant independent of the density variation at 120 km altitude.
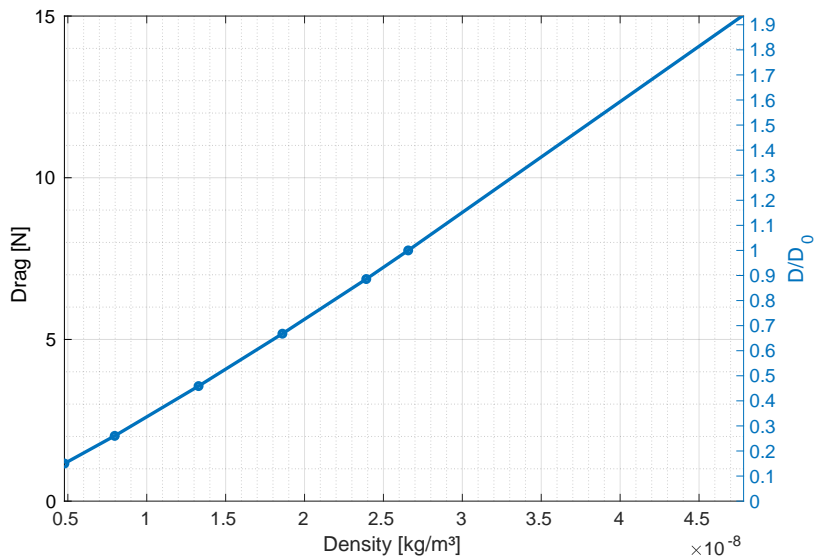

Figure 9.6: Sensitivity of a satellite's drag to density at 120 km altitude.

The range in $C_D * A_{ref}$ due to the density variation is equal to [6.8, 8.8]. The sensitivity index is therefore equal to 0.25. Practically this means that $C_D * A_{ref}$ can vary approximately a quarter of its value depending on the density.

When looking at the drag equation in Equation 6.1.4, the density is not only part of the satellite's $C_D * A_{ref}$, but also influences the drag directly. If $C_D * A_{ref}$ would be kept constant, the drag is linearly dependent on the density, such that an increase of 10x the density would mean an increase of 10x the drag. This is the case for the drag of satellites in the FMF regime, since the density does not influence the $C_D * A_{ref}$. Within the TF regime on the other hand, the total drag of a satellite is influenced by the change in density directly as well as through $C_D * A_{ref}$. The total drag for a satellite with respect to the density is given in Figure 9.6. There is an almost linear trend visible.

9.1.3 Gas mixture composition sensitivity

Next, it was also found that the gas mixture composition at a certain altitude could vary depending on the radiation or geomagnetic activity. In subsection 6.4.3, the following values for the mass concentrations of the most common thermospheric constituents at 120 km altitude (TF) and 300 km altitude (FMF) for low and high geomagnetic activity were found:

Table 9.3: Mass concentrations of the main constituents of the thermosphere at 120 km altitude and 300 km altitude during geomagnetic quiet time.

Altitude	120 km	300 km
Atomic Oxygen	0.08	0.73
Molecular Nitrogen	0.80	0.26
Molecular Oxygen	0.12	0.01

Table 9.4: Mass concentrations of the main constituents of the thermosphere at 120 km altitude and 300 km altitude during geomagnetic storm conditions.

Altitude	120 km	300 km
Atomic Oxygen	0.08	0.41
Molecular Nitrogen	0.82	0.57
Molecular Oxygen	0.09	0.02

In order to compare various compositions with each other, it is more efficient to calculate the aerodynamic coefficient per speed ratio corresponding to every gas component separately. Then, the total aerodynamic coefficient can be obtained by taking the weighted average of the aerodynamic coefficient based on the mass concentration of every constituent in the composition. These mass concentrations can then be changed easily without having to perform new simulations. This method has been validated in section 8.3.

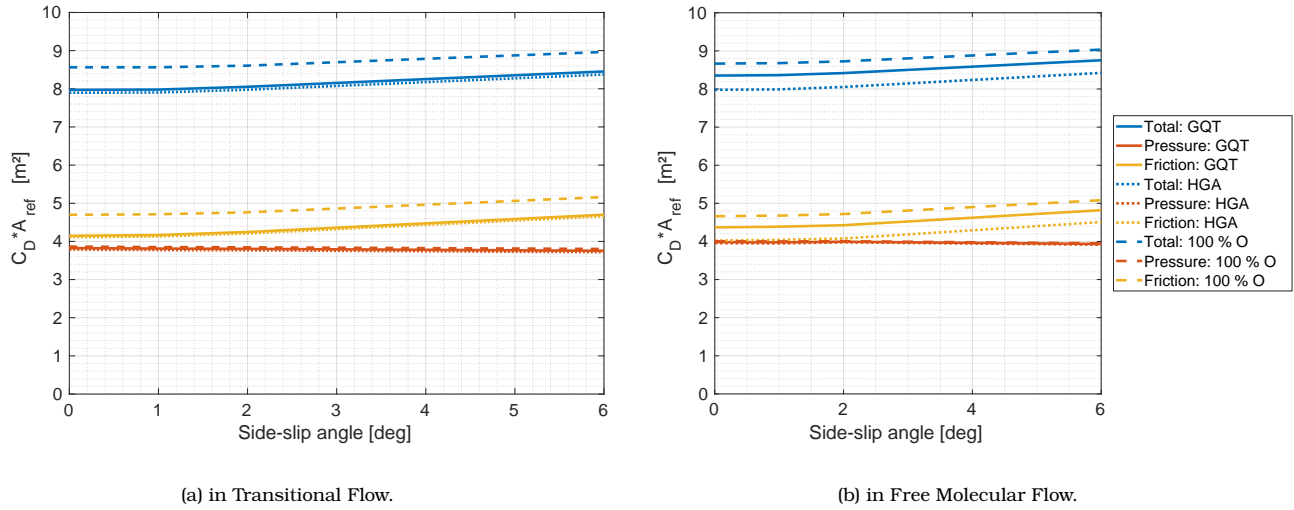(a) in Transitional Flow.   (b) in Free Molecular Flow.

Figure 9.7: $C_D * A_{ref}$ with respect to side-slip angle for three different gas composition cases: geomagnetic quiet time conditions (GQT), high geomagnetic activity (HGA) and for a 100 % atomic Oxygen gas.

In section 6.4, three cases were considered for the composition variability of the thermosphere: during GQT, during geomagnetic storm conditions with HGA and a completely atomic Oxygen atmosphere. The density and temperature is kept the same, even though it can be expected that during geomagnetic storm conditions the density and temperature might be higher as well. This is done to draw conclusions on the influence of only the composition variation. The drag coefficients for the three different cases are given with respect to the side-slip angle in Figure 9.7 for the TF (a) and the FMF (b).

The dotted and continuous line represent $C_D * A_{ref}$ for the geomagnetic storm conditions and the geomagnetic quiet time conditions respectively. It can be seen that there is a bigger difference in the $C_D * A_{ref}$ between GQT and GMA for the FMF than for the TF. This can be explained by the fact that the composition in FMF changes more depending on the geomagnetic activity than the composition in the TF as can be seen in the tables above.

The variation in composition at the TF altitude of 120 km, results in a difference in $C_D * A_{ref}$ of approximately: 0.08 m^2, which is less than 1% of the nominal value. This can be deemed negligible. At the FMF altitude of 300 km, the difference between low and high geomagnetic activity can result in a difference in $C_D * A_{ref}$ of 0.35 m^2, which is approximately 4% of the nominal value. It can be concluded that the variation in the gas composition of the thermosphere due to the change in geomagnetic activity has a much lower impact on $C_D * A_{ref}$, than the variation of the other thermospheric parameters, temperature and density, that change simultaneously with the change in geomagnetic activity.

The assumption of a 100% atomic Oxygen gas composition, which is shown by the striped lines, shows a significant influence in the TF regime at 120 km altitude. When decomposing the total $C_D * A_{ref}$, into the frictional (yellow) and pressure (red) components, it can be seen that the difference in total $C_D * A_{ref}$ is mainly due to the frictional component. Just as was the case for the temperature and density, due to the relatively large wings the frictional component is large as well. It is important to remember that the assumption of a 100% atomic Oxygen thermosphere can increase $C_D * A_{ref}$ with 7.5% at 120 km altitude and 3.7% for at 300 km altitude for the standard satellite shape including the wings and booms as described in this thesis. The reason that the sensitivity of $C_D * A_{ref}$ to this assumption is larger for at the TF altitude than at the FMF altitude, is that the TF is known to have a more molecular gas composition, which is therefore more different from the 100 % atomic Oxygen assumption. The influence of the assumption in the FMF is in the same order magnitude as the difference in $C_D * A_{ref}$ due to the change in composition from low to high geomagnetic activity.

9.2 Sensitivity to gas-wall collisions parameters

Next to the sensitivity to the thermospheric variability, it is expected from chapter 6 that the drag coefficient of the satellite is also dependent on the gas-wall collision parameters; the energy accommodation coefficient and the wall temperature. These parameters contain an uncertainty due to the unavailability of observational data. The influence of this uncertainty is tested in this section by performing a sensitivity analysis of the $C_D * A_{ref}$ with respect to a variation in these two gas-wall collision parameters.

9.2.1 Energy accommodation coefficient

The energy accommodation coefficient, α_E, is a coefficient that influences the way particles that hit the surface get reflected. The results for the sensitivity analysis is given in Figure 9.8. From March et al. [2019], it was found that for the GOCE and CHAMP satellites an energy accommodation coefficient of around 0.85 results in better thermospheric products from their measurements. For the FMF case, which is around the same altitude as these satellites, the total $C_D * A_{ref}$ does not change between the range for α_E of 0.8 and 1. From March et al. [2019] a larger sensitivity was expected than found here. This can be explained by the large contribution of the frictional component due to the relatively large wings of the standard satellite shape. Because of this, the change in the frictional and pressure component of the $C_D * A_{ref}$ due to the change in α_E seem to cancel out. With smaller wings, it could be expected that the contribution of the frictional component is smaller and therefore that the $C_D * A_{ref}$ will decrease with increasing α_E

For the TF case at 120 km, a slight decrease is visible in the total $C_D * A_{ref}$ when reducing the value of α_E. From Moe and Moe [2005] Hedin et al. [1973] it was concluded that for altitudes lower than 200 km, it can be assumed that the value for α_E is close to 1, because the incoming particles reflect in a diffuse direction due the coat of absorbed molecules.

However, a more thorough analysis of the influence of the variation of α_E for multiple angles and satellite shapes will give a valuable insight to get an indication of the influence of the uncertainty in this assumption. This will be further discussed in the recommendations section of the conclusion.

(a) In Transitional Flow.
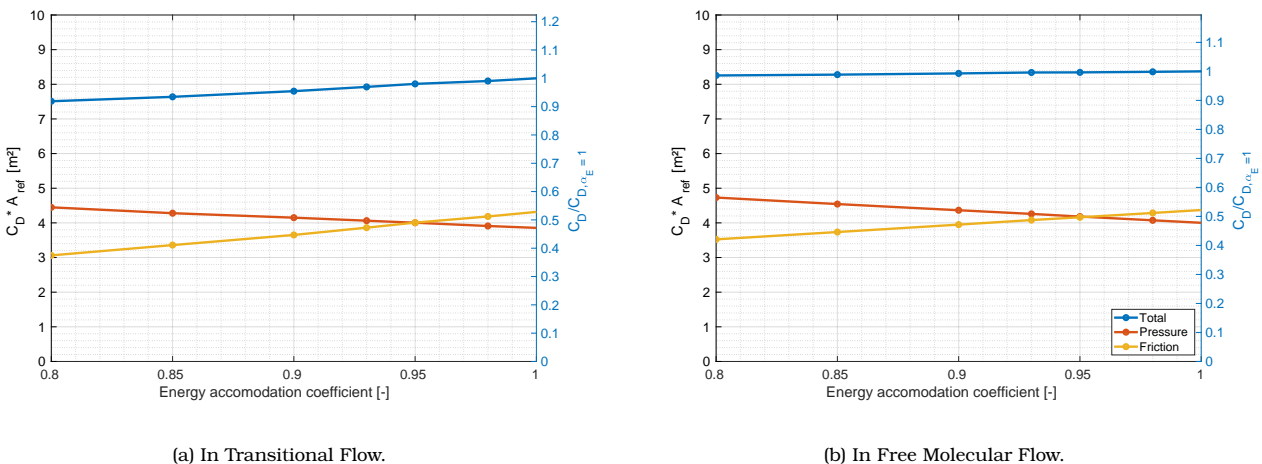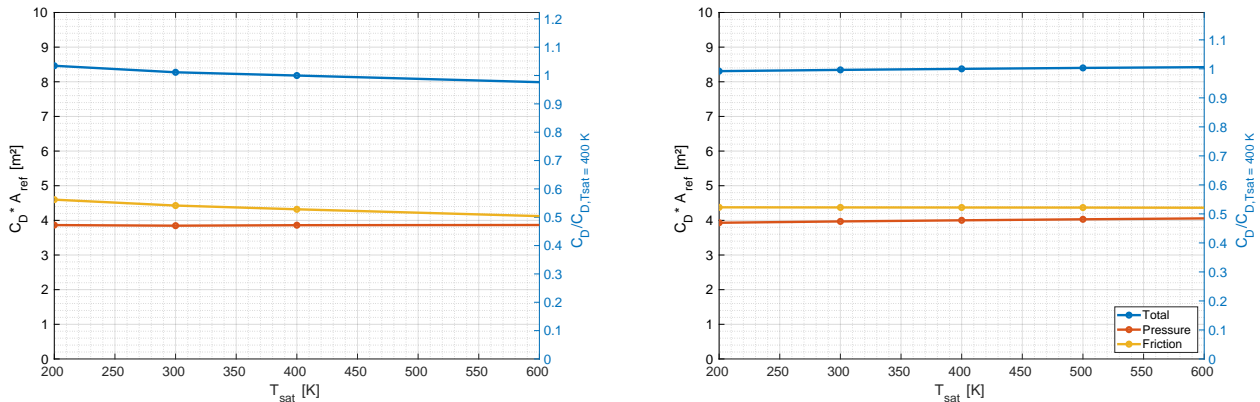
(b) In Free Molecular Flow.

Figure 9.8: Sensitivity of all components of $C_D * A_{ref}$ with respect to the energy accommodation coefficient.

9.2.2 Satellite wall temperature

From the theory discussed in chapter 6, it was expected that the sensitivity of the $C_D * A_{ref}$ to the satellite wall temperature is not significant for the FMF. This agrees with Figure 9.9b. In a range of ±

200 K there is negligible change visible in the total $C_D * A_{ref}$. For the TF however, it can be seen that there is some dependency on T_{sat}. The yellow and red line in Figure 9.9a represent the friction and drag component of the drag coefficient respectively. From this it can be concluded that the satellite wall temperature has most influence on the friction drag. The influence is in the order of 2% per 200 K.

(a) In Transitional Flow.

(b) In Free Molecular Flow.

Figure 9.9: Sensitivity of $C_D * A_{ref}$ with respect to T_{sat} for all satellite parts.

9.3 From 120 km altitude to 300 km altitude

The main differences between the TF and the FMF are the density, the composition, the gas temperature and the satellite velocity. The satellite velocity difference due to the change in perigee altitude from 120 km to 300 km has a negligible influence (1%), which is further elaborated upon in the coming chapters. The purpose of this section is to understand how the thermospheric conditions change when going from an altitude in TF regime (120 km) to the an altitude in the FMF regime (300 km) and how this influences the satellite's drag coefficient. The density, temperature are considered step by step. The analysis starts for a satellite in TF with the nominal values for gas temperature, gas density and gas composition that correspond to an altitude of 120 km. Next, only the density is changed until it is equal to the density that corresponds with 300 km altitude. Then, the mass concentrations that describe the composition are changed to the mass concentrations that were found at an altitude of 300 km. Now, the only difference with the FMF case at 300 km altitude is the gas temperature. The temperature is changed from 400 K corresponding to 120 km altitude to 1000 K corresponding to 300 km altitude. These steps are more elaborately described in this section.

The results for the change in density from the TF to the FMF are given in Figure 9.10. Just like in the validation based on the paper of Mehta et al. [2014] discussed in section 8.2, the $C_D * A_{ref}$ in Figure 9.10 and the C_D in Figure 8.2 shows a straight line until a density equal to the number density expressed in atomic Oxygen of 1e16 $/m^3$. Since A_{ref} does not change by changing the density, this means that the density does not influence the C_D until that point. After that point the $C_D * A_{ref}$ is increasing fast. This is different from what was found in the validation with Mehta et al. [2014] in section 8.2, where the value for C_D decreases when the density increases. This can be explained by the fact that the satellite shapes for which the $C_D * A_{ref}$ are obtained are different in both cases. From Figure 9.10, it can be found that the large increase with density is mainly due to the frictional component. From prior analysis it was found that the large frictional component is mainly caused by the relatively large solar array wings. The shapes tested in Mehta et al. [2014] are cylinders, without solar arrays, with a smaller length over cross-sectional area than the body of the standard shape. Because of this the frictional component is small and the drag coefficient will go down with density. A similar trend can be seen for the pressure

component of the drag coefficient in Figure 9.10.
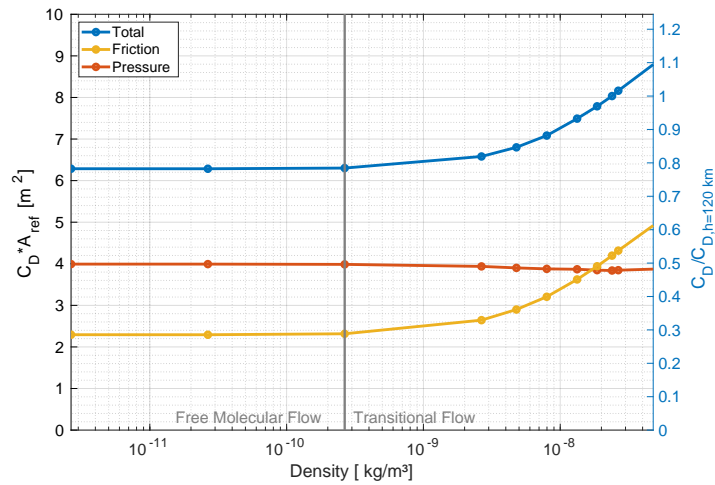
Figure 9.10: Change in $C_D * A_{ref}$ due to change in density from 120 km altitude (TF) to 300 km altitude (FMF).
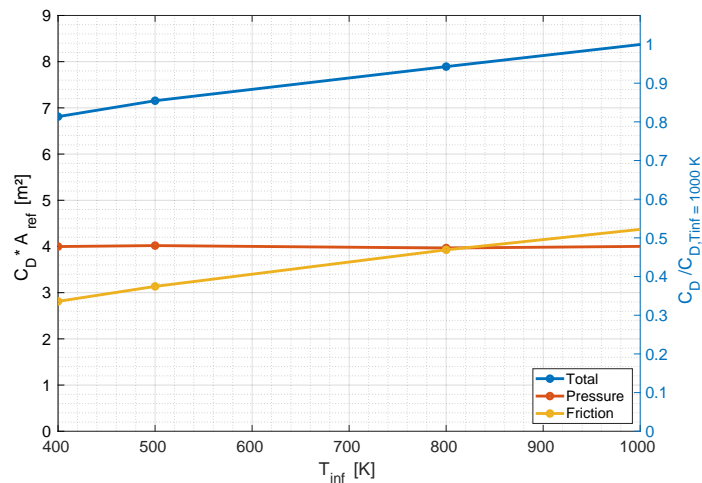
Figure 9.11: Change in $C_D * A_{ref}$ due to change in thermospheric gas temperature from nominal value at 300 km altitude (1000 K) to nominal value at 120 km altitude (400 K).

To visualize this, in Figure 9.4b the Paraview image of the satellite in the flow for a FMF density is given. This can be compared to the to the result for the standard satellite model with nominal value for density in TF in Figure 9.3. The color scaling is adapted relatively to the density of the main flow. It can be observed that the relative density above the wings is much higher for the TF density case than the relative density above the wings for the FMF density case. That is why the frictional component of the body and the wings is relatively higher when intermolecular collisions occur. On the other hand, the colors in front of the satellite are more bright for the FMF density case. This is the reason that in Figure 9.10 for low densities in the FMF the pressure component of the drag coefficient is found to be larger.

The difference in $C_D * A_{ref}$ due to solely the density change from 120 km to 300 km is equal to -1.9 m^2, which is a decrease of approximately 23%. However, density never changes by itself. With increasing altitude it was found in the theoretical background in chapter 6 that while the density decreases the temperature increases. In addition, the gas composition changes from a molecular composition to an atomic composition.

In Figure 9.11 the results are given for the composition and density corresponding to the FMF altitude at 300 km, whereas the gas temperature is varied from the nominal value at 120 km altitude (400 K) to the nominal value at 300 km altitude (1000 K). Unlike the density, the temperature increases with increasing altitude, and consequently increases the value of $C_D * A_{ref}$. At 400 K the value for $C_D * A_{ref}$ in Figure 9.11 is equal to 6.8 m^2. Whereas the value for $C_D * A_{ref}$ in Figure 9.10 for the same FMF density and gas temperature of 400 K, but a different composition, is equal to 6.3 m^2. $C_D * A_{ref}$ is 0.5 m^2 lower for the the more molecular composition corresponding to the TF at 120 km altitude. In subsection 9.1.3, it was found that the value for $C_D * A_{ref}$ in the FMF can change 5% between geomagnetic quiet time and geomagnetic storm conditions when looking at the impact of the changes in composition. The difference in the mass concentrations between the two altitude cases is even larger than the difference between high and low geomagnetic activity in the FMF. Furthermore, it was found that a lower mass ratio of atomic oxygen and a higher mass ratio of molecular nitrogen results in a decrease in $C_D * A_{ref}$. This explains the gap of 0.5 m^2 between the two graphs.
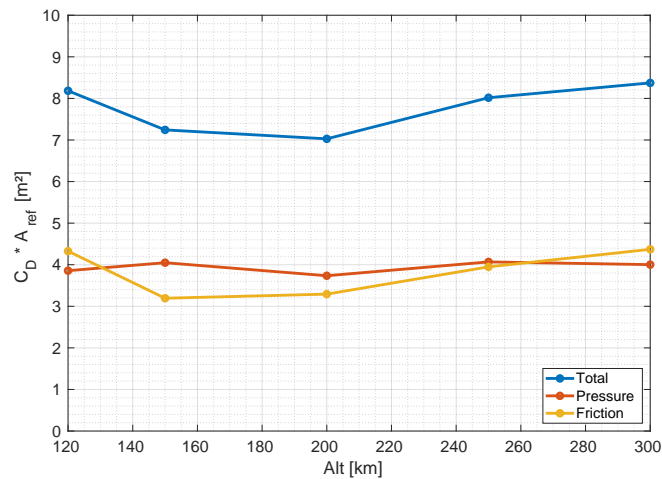
Figure 9.12: Pressure, frictional and total drag coefficients with respect to altitude.

In conclusion, with increasing altitude the density decreases which reduces the value of $C_D * A_{ref}$ until the FMF is reached. However, at the same time the temperature increases and the mass concentration of atomic oxygen will increase which increases the value for $C_D * A_{ref}$ again. As was found in NRLMSISE-00 result in Figure 6.3, the density decreases from 120 to 150 km altitude from approximately 3e-08 to 2e-09 kg/m^3 , while the temperature goes from 400 to 600 K approximately. When looking at the graphs given in Figure 9.10 and Figure 9.11, it can be found that the $C_D * A_{ref}$ due to the density will decrease with 1.66 m^2, whereas the $C_D * A_{ref}$ due to the temperature will increase less than 1 m^2. Therefore it can be expected that the value for $C_D * A_{ref}$ will first decrease with increasing altitude. However, when going higher, the density decreases even more and the graph for $C_D * A_{ref}$ in Figure 9.10 flattens. Around an altitude of 170-200 km, the density reaches a value of less than 0.5e-9 kg/m^3, which is approximately the value of the FMF regime as can be found in Figure 9.5a. $C_D * A_{ref}$ is now not anymore influenced by the density. At that point the temperature is still increasing and influencing the value for $C_D * A_{ref}$, so it is expected that the $C_D * A_{ref}$ will increase again.

To test this, single simulations are performed for a few altitudes for the standard satellite shape for side-slip angle = $0°$, wind = 0 m/s and roll angle = $0°$. The results are given in Figure 9.12. Since it is time consuming to take many steps in between, only 5 points are taken. The purpose is to give an idea of the trend of the $C_D * A_{ref}$ with altitude. The results presented in Figure 9.12 agree with the behaviour of $C_D * A_{ref}$ as described before.

9.4 Summary of the aerodynamic coefficient sensitivities

In Table 9.5, the sensitivity of $C_D * A_{ref}$ with respect to the input parameters is given. Note that the sensitivity to composition change in the thermosphere is also given. However, for this sensitivity, not a range of values is tested, just two cases; one case during geomagnetic quiet time and one case during high geomagnetic activity. The values for both cases are given in the table. The nominal values for the composition expressed in mass concentrations is taken to be equal to the values during geomagnetic quiet time.

Table 9.5: $C_D * A_{ref}$ sensitivity index for all parameters for the standard satellite model in m^2.

Parameter	Flow regime	$C_{D,nominal}$	$C_{D,min}$	$C_{D,max}$	S_I
T_{inf}	TF	8.19	7.95	8.57	0.075
	FMF	8.38	7.15	9.49	0.28
ρ	TF	8.16	6.80	8.79	0.24
	FMF	8.38	8.38	8.38	0
Composition	TF	7.97	7.89	7.97	-0.01
	FMF	8.36	7.98	8.36	-0.05
T_{wall}	TF	8.18	8.46	7.99	-0.057
	FMF	8.37	8.31	8.42	0.013
α_E	TF	8.17	7.51	8.17	0.08
	FMF	8.37	8.25	8.37	0.014

The nominal values for $C_D * A_{ref}$ change slightly for the different sensitivity analyses. The changes are generally smaller than one percent and can be explained by simulation errors. The largest difference is with the composition nominal value. This is due to the difference in method, which was explained in section 8.3. The difference is between 2-3%.

In conclusion, it was found that the total sensitivity to the thermospheric parameters is higher for the FMF than for the TF altitude. This can be explained by the fact that the range of the thermospheric condition parameters is larger at larger altitudes. In addition, it was found that mainly the relatively large wings were responsible for the sensitivity of the satellite with respect to temperature, density and composition. The value of $C_D * A_{ref}$ for the booms did not change throughout all the cases.

Chapter 10

Wind influence results

The focus of this research is to examine the influence of horizontal wind on the satellite aerodynamics in the TF. The aerodynamics of a satellite in the TF regime at 120 km altitude is compared to the aerodynamics in the better known FMF regime at 300 km altitude. In the previous chapters the nominal values for the thermospheric conditions surrounding the satellite have been chosen and the sensitivity of their variability has been researched. In this chapter, the influence of horizontal wind on a standard satellite shape is tested assuming the thermospheric parameters to be constant and equal to the nominal values as given in Table 8.3. The dynamic range for HWM14 and in-situ data sets of the horizontal neutral winds were stated in chapter 5. The computational simulations as described in chapter 7 are run for multiple wind magnitudes within that range. In addition, the influence of the errors between HWM14 and in-situ data is highlighted and discussed.

The wind influences the direction and magnitude of the relative velocity of the satellite with respect to the surrounding gas. Another important factor of the relative velocity is the orbital velocity of the satellite. The orbital velocities at the perigee altitudes of 120 km in the TF and 300 km in the FMF have been found in section 3.1. All velocities are summarized in Table 10.1.

Table 10.1: Orbital velocities and maximum horizontal wind velocities.

Velocity [m/s]	120 km	300 km
Wind from HWM14	200	500
Wind from in-situ data	370	1080
Orbital velocity	8455.9	8293.4

The wind can be decomposed in two directions. The wind in the cross-track direction of the satellite and the wind in the in-track direction of the satellite. The influence of both wind directions are discussed in section 10.1 and section 10.2 respectively. The values for $C_D * A_{ref}$ per altitude and per wind source input are summarized in section 10.3

10.1 Cross-track wind influence

The influence of the cross-track wind is illustrated in Figure 10.1. Here the satellite has a forward velocity with respect to the surrounding gas ($\bar{V}_{r,orb}$). In this case this is equal to the orbital velocity at the perigee. The wind introduces a cross-track movement of the gas particles and therefore a cross-track velocity relative to the surrounding gas ($\bar{V}_{r,wind}$). The magnitude of the total relative velocity ($\bar{V}_{r,tot}$) can be computed by using the Pythagoras theorem. The difference in magnitude between the satellite's

orbital speed and the total relative speed can be calculated by Equation 10.1.1.

$$V_{r,tot} - V_{r,orb} = \sqrt{V_{r,wind}^2 + V_{r,orb}^2} - V_{r,orb} \tag{10.1.1}$$
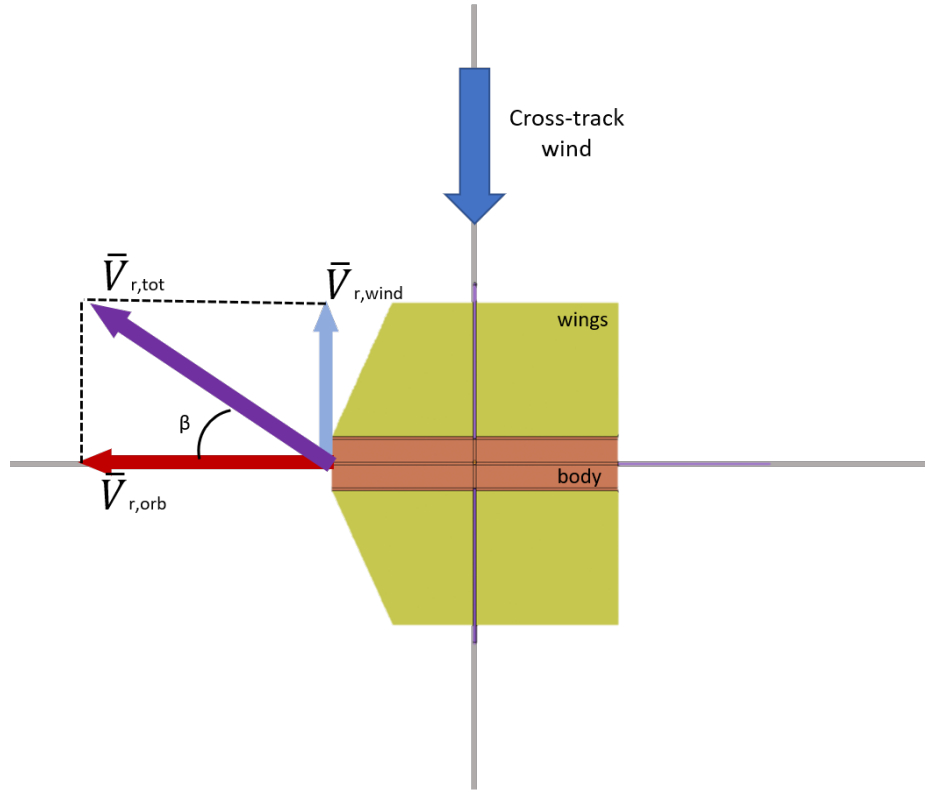
Figure 10.1: Illustration of the influence of cross-track wind on the colored satellite shape.

From Equation 10.1.1, it can be concluded that the difference between the total relative speed with the orbital velocity is largest when $V_{r,orb}$ is smallest and $V_{r,wind}$ is largest. For the two perigee altitudes investigated in this study, this is the case for an perigee altitude of 300 km.

In that case, the satellite moves with a velocity of approximately 8300 m/s through its perigee. The maximum wind that can be encountered at that point is 1080 m/s. In the worst-case scenario in terms of cross-track wind, the total wind of 1080 m/s is directed perpendicular to the satellite's velocity. This results in a worst case difference of 70 m/s between the orbital speed and the total relative speed. In section 11.1, a difference of 100 m/s in the relative speed is tested. There it is found that the difference in negligible. To simplify the simulations and to minimize the number of runs necessary, it is therefore assumed that $V_{r,tot} \approx V_{r,orb}$.

The resulting side-slip angle (β), as shown in Figure 10.1 can be calculated by Equation 10.1.2. Due to the symmetry of the satellite, it does not matter if the wind reaches the satellite from the left or right side.

$$\beta = tan^{-1}\left(\frac{V_{r,wind}}{V_{r,sat}}\right) \tag{10.1.2}$$

Using Equation 10.1.2 and the values given in Table 10.1 the side-slip angles can be calculated. The results are given in Table 10.2

Table 10.2: Side-slip angles [deg], β, due to the wind at perigee altitude due to TF and FMF regimes.

Data source	120 km	300 km
HWM14	1.3	3.5
In-situ data	2.5	7.4

To quantify the influence the cross-track wind has on the satellite, the simulation is run for various side-slip angles. The wind induced side-slip angles that are given in Table 10.2 are marked in the figures with a grey (model) and black (data) line. The influence of the wind is modeled for the case that the roll angle of the satellite is equal to 0 and 90°.

The result for roll angle = 0° is given in Figure 10.2a for the TF and in Figure 10.2b for the FMF case. Note the difference of magnitude in the x-axis. The wind results in a larger side-slip angle in the FMF case than the TF case. Generally, it can be concluded from the plots, that when the side-slip angle is increased, the contribution of the body to the total $C_D * A_{ref}$ is increasing while the contribution of the wings and the booms stay constant. This is because when the relative velocity of the satellite with respect to the gas is on an side-slip angle with respect to the satellite shape, the gas particles push against the sides of the satellite. This is a larger area than the frontal area and therefore increases the $C_D * A_{ref}$. The areas of the wings and booms does not increase much when a side-slip angle is introduced, this agrees with the straight lines visible in the plots.

On the right y-axis of both plots the fractional increase is given. The fractional increase is defined in this thesis as:

$$\frac{(C_D * A_{ref})_\beta}{(C_D * A_{ref})_{\beta=0°}}$$

In other words it shows to relative increase of the $C_D * A_{ref}$ due to the side-slip angle. At $\beta = 4°$, the $C_D * A_{ref}$ has increased 2.7% for the TF 2.2% for the FMF. Even though the increment in C_D is slightly higher for the TF, the difference is so little that no strong conclusions can be made.

(a) In Transitional Flow.

(b) In Free Molecular Flow.
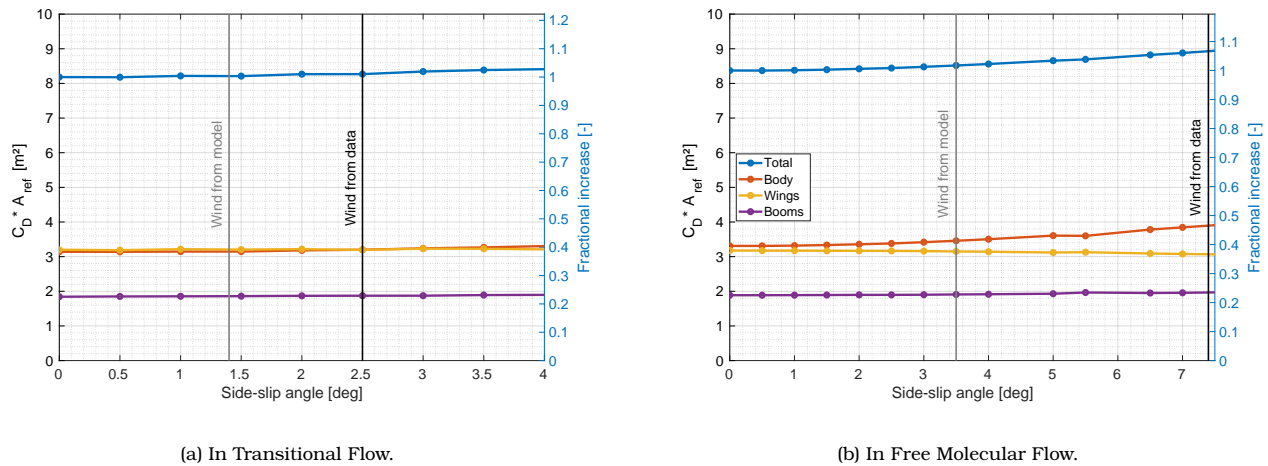
Figure 10.2: $C_D * A_{ref}$ variation of standard satellite model with respect to the side-slip angle due to cross-track winds at 120 km altitude (a) and 300 km altitude (b), for roll angle = 0°.

In conclusion, the biggest difference between the TF case and the FMF case lies in the difference in the magnitude of the wind and therefore the difference in side-slip angle. In case of the TF, the maximum wind results in a side-slip angle of $2.5°$. The respective $C_D * A_{ref}$ is equal to $8.27\ m^2$, which is an increase of the nominal value of approximately 1%. This is in the same order of magnitude as the simulation

errors as found in section 8.4. From this it can be concluded that for the TF case, the cross-track wind does not have a significant influence. For the calculation of the drag for a satellite in TF when roll angle = 0°, it is therefore not a needed to take the cross-track wind into account.

For the FMF case the side-slip angles are bigger. The $C_D * A_{ref}$ values for the side-slip angle due to the maximum model wind and maximum data wind are 8.52 m^2 and 8.93 m^2 respectively. This is an increase with respect to the nominal case with $\beta = 0°$, equal to 8.38, of 1.7% and 6.7%.

The result for roll angle = 90° is given in Figure 10.3a for the TF and in Figure 10.3b for the FMF case. Again, it should be noted that the x-axis of the both plots are different due to the fact that in the FMF case the wind introduces a bigger side-slip angle. When comparing these to Figure 10.2, it can directly be seen that the side-slip angle has more influence when the satellite is turned 90°. The contribution of the various parts of the satellite are given. The value for $C_D * A_{ref}$ for the body increases similarly as for the case described above when the roll angle is 0. It can be concluded that the contribution of the body is independent of roll. This is due to the body's symmetry around the x-axis. Furthermore, it can concluded that the $C_D * A_{ref}$ of the booms is independent of the cross-track wind.

From Figure 10.3a and Figure 10.3b, it can be found that the biggest change in $C_D * A_{ref}$ is in the contribution of the wings. The bigger the side-slip angle, the more wing area is exposed in the direction of the relative velocity. That is why in the plots an increase as part as a sine wave can be observed. In this case, there is also a significant difference in the results when the wind from the model is assumed compared to when the wind from the in-situ data is taken into account. For the TF altitude of 120 km in Figure 10.3a, the wind from the model results in an increase of 2.5%, with respect to an increase 8.2% when the in-situ data is assumed with respect to the nominal $C_D * A_{ref}$, which equals $\pm$ 8.2 m^2. For the FMF altitude this is an increases in the nominal $C_D * A_{ref}$ (equal to 8.34 m^2 of 12% when assuming the horizontal wind from the model, compared to 47% increment when taking into account the wind from the in-situ data.

Furthermore, when comparing both regime cases again with each other for side-slip angle = 4°, it can be found that the increase in the TF with respect to no side-slip angle is slightly higher, from 8.2 to 9.6 (18%), with respect to the FMF case, from 8.3 to 9.1 (15%).

It can be expected that the increase in the drag coefficient due to the wings is related with the size of the wings. This is tested in chapter 12.

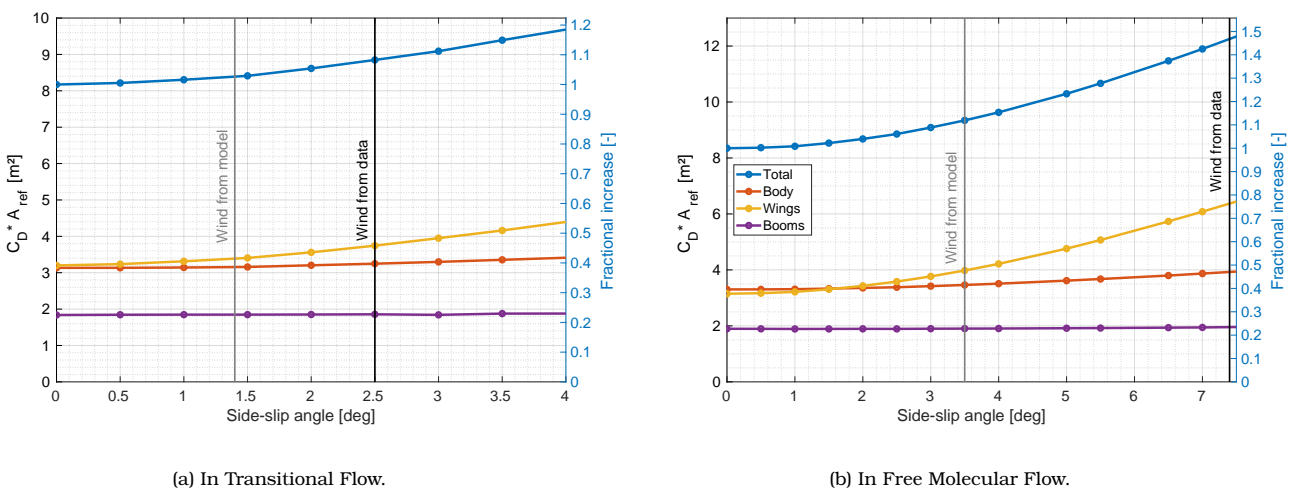(a) In Transitional Flow.   (b) In Free Molecular Flow.

Figure 10.3: $C_D * A_{ref}$ variation of the standard satellite shape with respect to the side-slip angle due to cross-track wind at 120 km altitude (a) and at 300 km altitude (b), for roll angle = 90°.
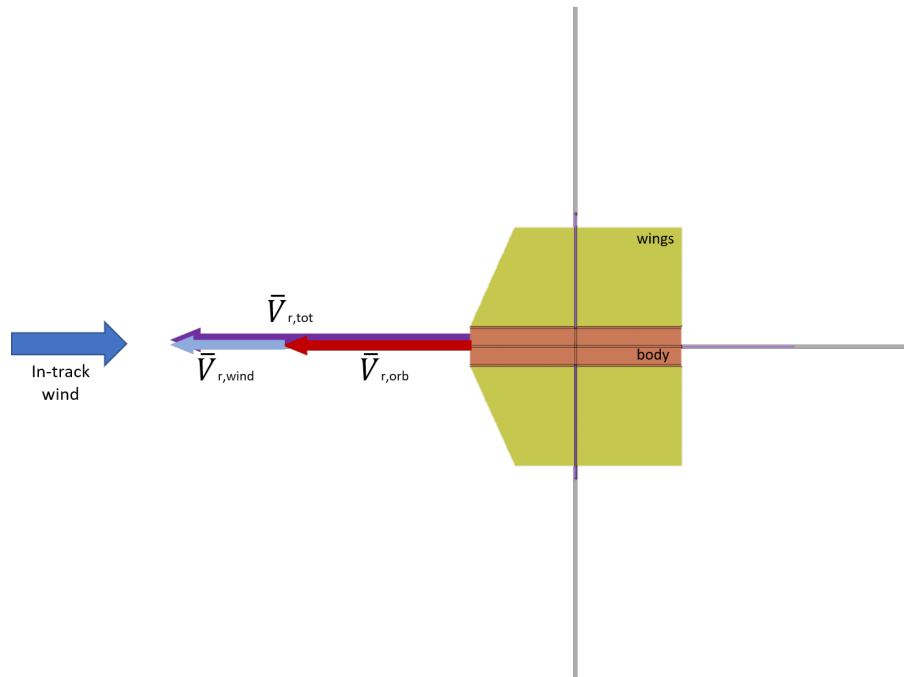
10.2   In-track wind influence

Figure 10.4: Illustration of the influence of in-track wind.

The in-track wind influences the relative velocity of the satellite with respect to the atmosphere as illustrated in Figure 10.4. The wind can be blowing in the same direction as the satellite velocity, tailwind, or in the opposite direction, headwind. This will decrease or increase the relative velocity of the satellite respectively. The wind is defined positive if it increases the relative velocity of the satellite with respect to the flow, which is the case for the head wind. The tailwind is defined negative.

To test what the quantified influence is of the in-track wind on the satellites aerodynamic coefficients, the wind velocity is added to the satellite velocity. Since the wind is then in the same plane as the satellite, it can be expected that the wind does not have an influence on the lift coefficient or on the side-slip angle.

At the TF altitude of 120 km, it was found that the maximum wind in the data is 370 m/s in the altitude region of 110-130 km. The simulation is run for various magnitudes of the in-track wind. The results are given in Figure 10.5a. Here the total drag coefficient, the frictional and pressure drag coefficient are given. The graph shows nearly a straight line for all drag coefficient components. This means that the in-track wind has a negligible influence on the drag coefficient in case of the TF.

For the FMF case at 300 km altitude, the influence of the in-track wind on the standard satellite's $C_D * A_{ref}$ is larger due to the increase in the magnitudes of the wind found at higher altitudes. By increasing the head wind, the relative velocity of the satellite with respect to the thermosphere increases too. It was found that when the relative velocity increases the speed ratio increases. Because of this, the frictional component of the wind on the sides decreases, which decreases the total drag coefficient as well, this agrees with Figure 10.5b. When, on the other hand, the tailwind is increasing, the opposite can be observed, due to the decrease of relative velocity and therefore a decrease in speed ratio.

In previous analysis it was found that the wings contribute most to the frictional component of the drag coefficient. Therefore, the difference in $C_D * A_{ref}$ with varying in-track wind is mainly due to the wings. This agrees with the results shown in Figure 10.6. Here the total $C_D * A_{ref}$ is decomposed in

the contribution of the various satellite body. The line that signifies the wings (yellow) decreases most rapidly with rising head wind and therefore increasing relative velocity.
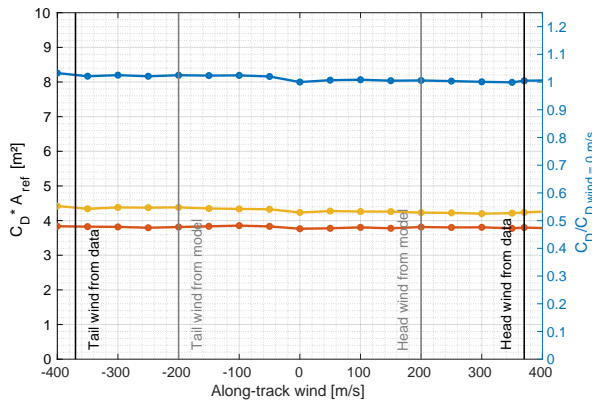
(a) In Transitional Flow.
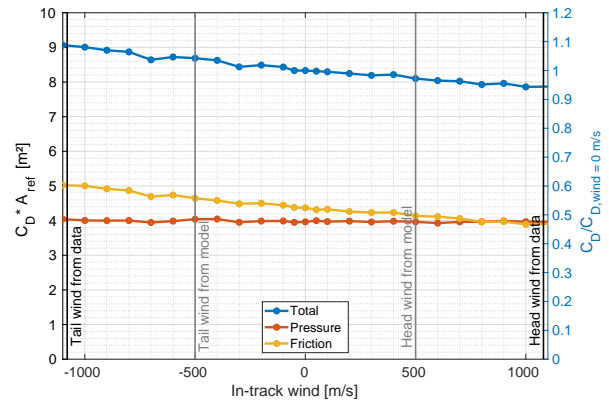
(b) In Free Molecular Flow.

Figure 10.5: The influence of the in-track wind found in the TF (a) and FMF (b) on the drag coefficient components.
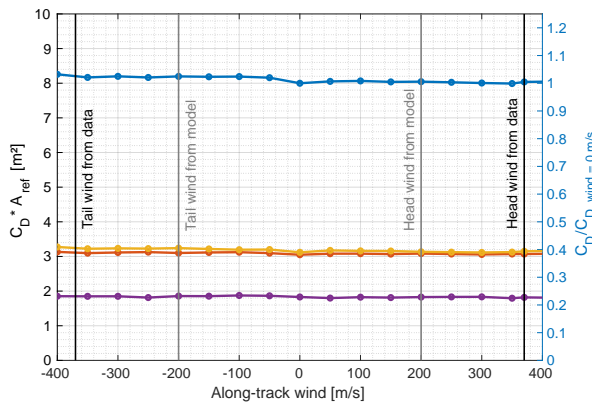
(a) In Transitional Flow.
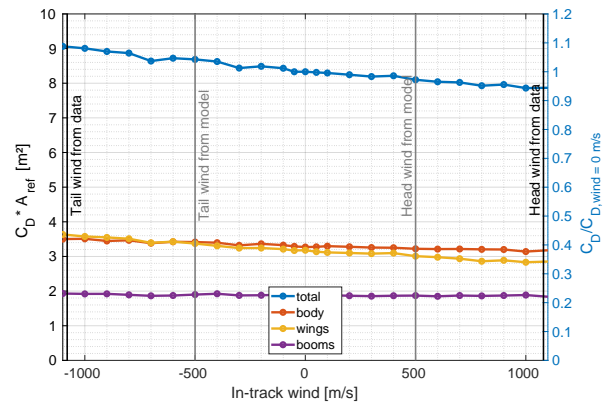
(b) In Free Molecular Flow.

Figure 10.6: The influence of the in-track wind found in the TF (a) and FMF (b) on the body, wings and booms.

In addition, when looking at the drag equation given in Equation 6.1.4, the wind does not only influence the $C_D * A_{ref}$, but also the velocity, V. Consequently, even though the in-track wind does not influence the satellite's $C_D * A_{ref}$ significantly, the increase in relative velocity due to the wind can increase the drag on the satellite as can be seen in Figure 10.7. Here the results for the total drag with respect to the in-track wind are shown. The plot shows that the total drag can increase with 9.5%, equal to 0.72 N, in the TF regime at 120 km altitude under the assumption of the worst-case headwind from in-situ data, in case the other parameters stay constant. In the FMF, the total drag is much lower due to the lower density. The maximum in-track headwind obtained from in-situ data can results in an increase in the drag of 19.0%, which is equal to approximately 1.4e-4 N. For the tailwind, the opposite could be observed and the drag is decreased by similar values. Over the complete mission lifetime, it can be expected that the satellite encounters the wind the same amount of time from the front as from the back. This means that the drag will sometimes be increased, and sometimes decreased. Over the complete

mission lifetime, the assumption could be made that the drag due to the in-track wind balances out.

(a) In Transitional Flow.

(b) In Free Molecular Flow.
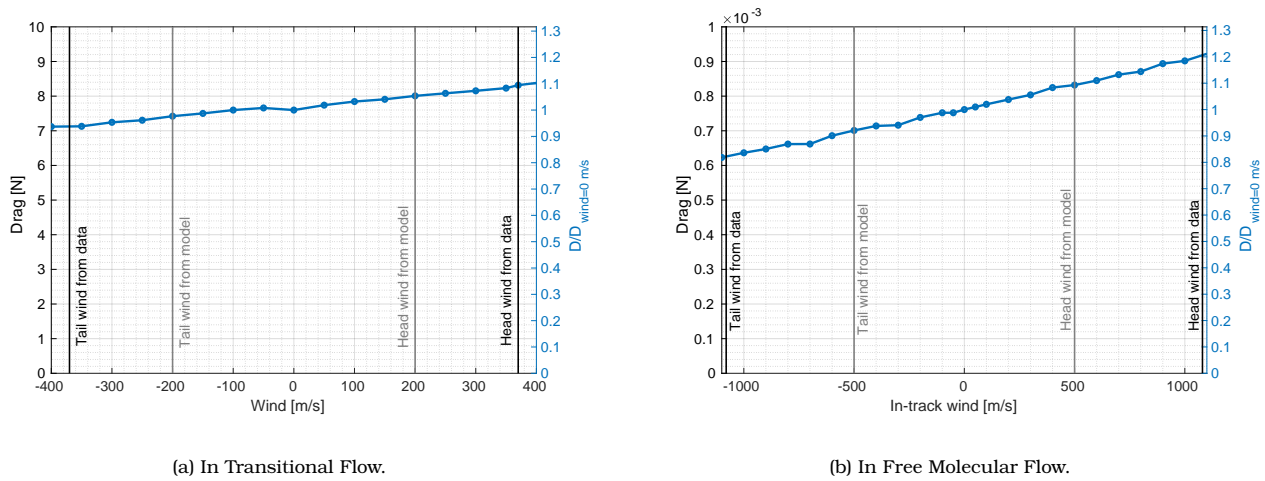
Figure 10.7: The influence of the in-track wind on the Drag.

10.3 Summary of wind influence

In this section, the results of the previous chapter are summarized. First the conclusions on influence of the cross-track wind on the $C_D * A_{ref}$ of the standard satellite shape are summed-up, which is followed by conclusions about the influence of in-track wind. In Table 10.3, the summary of the influence of the worst-case cross-track wind on $C_D * A_{ref}$ can be found subdivided by the respective wind data source. From this it can be concluded that in the TF regime at 120 km, when the satellite is rolled 0°, the cross-track wind has a negligible influence. When the satellite is rolled 90°, the worst-case cross-wind can increase the $C_D * A_{ref}$ with 8.2%, due to the contribution of the satellite wings. The value for $C_D * A_{ref}$ of the satellite body part increases slightly with increasing the side-slip angle. The influence of the wind on the $C_D * A_{ref}$ value of the booms is negligible.

The strongest winds can be found during geomagnetic storms. From the previous chapter it was found that during geomagnetic storms the density and therefore the drag is already larger. An increase of 8.2% in the already increased drag, results therefore in a significant increase in drag. This increment in $C_D * A_{ref}$ was only visible when taking the in-situ wind data into account. When using the data from the models, a insignificant increment of 2.5% would have been found.

In addition, it was concluded that the cross-track wind has more influence on the satellite's $C_D * A_{ref}$ in the FMF. This is due to the fact that in the FMF altitude range stronger winds occur than in the TF altitude range, and therefore larger side-slip angles are induced due to the wind. The general increment in $C_D * A_{ref}$ per beta angle is however slightly bigger for the TF than for the FMF regime.

Table 10.3: Total $C_D * A_{ref}$ taking into account cross-track wind obtained from HWM14 and in-situ data for Transitional Flow and Free Molecular Flow.

Case	No wind	roll = 0°		roll = 90°	
		model	data	model	data
TF [m^2]	8.18	8.21	8.27	8.39	8.85
FMF [m^2]	8.38	8.85	9.26	9.34	12.25

The in-track wind does not only influence $C_D * A_{ref}$, but also influences the drag directly by increasing or decreasing the relative velocity of the satellite with respect to the gas, as stated in the drag equation. The in-track wind influence on the total drag is summarized in Table 10.4. It was found that the increase in drag due to headwind is similar as decrease in the drag due to tailwind. Over a complete mission duration of a global and geomagnetic activity coverage, it can be assumed that these cancel out. More research should be done to prove this.

Table 10.4: Total drag taking into account in-track wind obtained from HWM14 and in-situ data for Transitional Flow and Free Molecular Flow.

Case	No wind	Tailwind		Headwind	
		model	data	model	data
TF [N]	7.60	7.42	7.12	8.01	8.32
FMF 1e-4 [N]	7.61	7.00	6.23	8.32	9.05

Chapter 11

Mission design sensitivity results and discussion

Now that the aerodynamics of a satellite are explained and the influence of the wind on the nominal case with the standard satellite shape and nominal mission geometry is analyzed, the focus of this chapter will be on the impact of the variations from that nominal case on the satellite's drag. This chapter focuses on the variations in mission geometry. To do this, for every section of this chapter, the focus will be on one of the still open design choices for Daedalus, for which the influence on the drag and on the wind sensitivity will be evaluated. The rest of the parameters stay equal to the nominal values. The nominal values of the input parameters are summarized in Table 11.1.

Table 11.1: Nominal values for input parameters.

Parameter	Nominal value		unit
	FMF	TF	
Altitude	300	120	km
T_{wall}	400	400	K
T_{inf}	1000	400	K
α	1	1	$-$
m	16e-3	16e-3	kg/mol
R_{gas}	519.65	519.65	$J/(K*kg)$
V_r	8293.4	8455.9	m/s
ρ	2.66e-8	2.66e-12	kg/m^3

The chapter starts by evaluating the influence of the apogee in section 11.1. Secondly, the influence of the satellite attitude is tested and discussed in section 11.2. In chapter 12, the results for the satellite geometry variation are discussed.

11.1   Influence of apogee altitude

As explained in section 3.1, it was found in ESA [2020], that there are two possibilities for the apogee altitude: at 2700 km and at 2200 km. The nominal value for this thesis has been 2700 km. In this section, it will be investigated what the aerodynamics will be of a satellite with a lower apogee altitude. The respective satellite velocities for the apogee/perigee altitude combinations are summarized in Table 11.2

Table 11.2: Satellite velocity [m/s] in the perigee for apogee altitude and perigee altitude combination.

	Perigee: 120 km	Perigee: 300 km
Apogee: 2200 km	8355.0	8192.8
Apogee: 2700 km	8455.9	8293.4

A lower apogee means a lower orbital velocity in the perigee of the orbit. Consequently, the side-slip angle induced by the wind is slightly bigger. The aerodynamic coefficients are modeled for various side-slip angles, β, with the different satellite velocities. The results for both the TF and FMF are given in Figure 11.1.

The dotted line corresponds to the results for the apogee altitude of 2200 km and the continuous line corresponds to the results for the apogee altitude of 2700 km. In addition, the respective side-slip angles for maximum model wind and maximum in-situ data wind are marked with grey and black continuous and dotted lines. Since the colored lines seem to overlap, the velocity change of approximately 100 m/s does not have a significant influence on the C_D or how the wind influences the C_D. The difference between the two cases are for every side-slip angle smaller than 1%. The biggest influence the different apogee altitude has on the C_D is due to the slight increase in side-slip angle per wind speed, due to the smaller difference between the wind velocity and the satellite orbital velocity. For a roll angle of 90 degrees and assuming maximum cross-track wind, the maximum difference in C_D due to the decrease of apogee altitude is 8.848-8.861 = 0.013, which is still less than 1%.

A change in relative velocity does not only influence the drag coefficient, but also influences the drag directly. The velocity at the perigee decreases with approximately 100 m/s, when the apogee altitude decreases from 2700 km to 2200 km. This is a decrease of approximately 1% for both cases. Since the change in V is squared in the drag equation, the difference for the drag is slightly more than one percent, but still negligible.

(a) In Transitional Flow.

(b) In Free Molecular Flow.
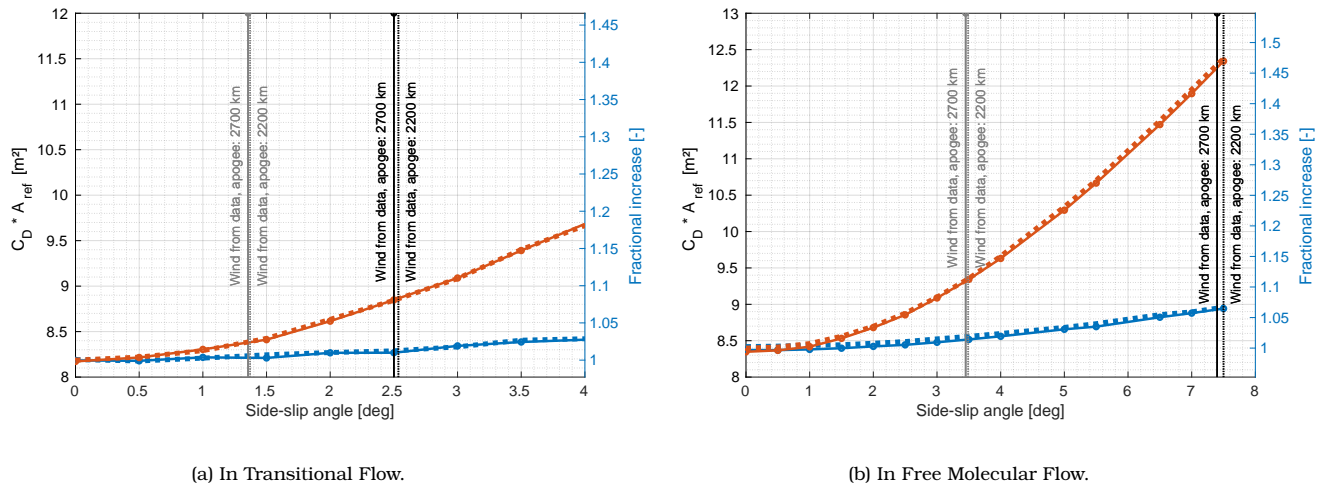
Figure 11.1: Difference between apogee altitude of 2700 km (continuous) with 2200 km (dotted) for roll = 0° (blue) and roll = 90° (red) analyzed for $C_D * A_{ref}$ for cross-wind induced side-slip angles.

Although the difference in apogee altitude does not result in a significant change in the drag, it does change the semi-major axis of the orbit. When the decay of the semi-major axis was explained in section 6.2, it was found that the semi-major axis itself also influences the rate of decay. To find out what that decay is due to the change in apogee altitude, the computations as explained in section 6.2, are run for a few possibilities in terms of apogee altitude. The result is given in Figure 11.2. It can be

found that by increasing the apogee altitude and therefore the semi-major axis, the decay of the satellite increases exponentially. In order to keep the satellite in the preferred orbit, it can be expected that more propulsion will be needed. On the other hand, it should be noted that by increasing the apogee altitude, it will take longer for the satellite to circularize and completely decay. What this shows is that the mission lifetime can be prolonged by increasing the apogee altitude. However it can be expected that, the decay will be higher in the beginning and then exponentially decreases when the apogee is lowering.

Figure 11.2: Decay per day with respect to apogee altitude, with a perigee altitude of 120 km.

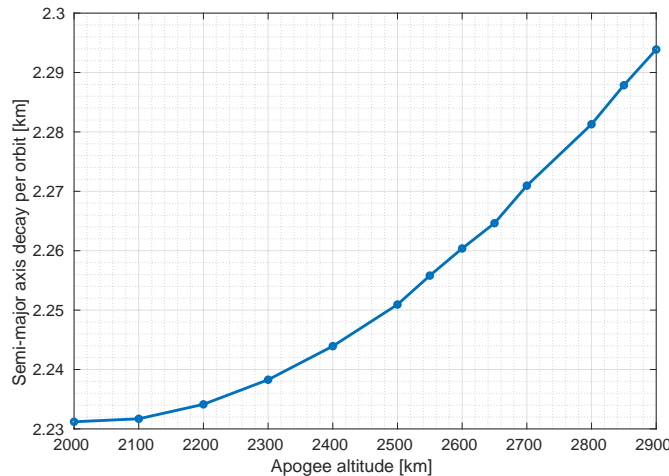From this analysis it can be concluded that for the choice of apogee altitude, the aerodynamics in terms of C_D and the influence that the wind has at the orbit's perigee do not have to be taken into account. However, the apogee should be taken into account when estimating the decay per orbit.

11.2 Influence of satellite attitude

In this thesis a perfect attitude control has been assumed where the $\alpha = 0°$, β is only induced by the wind and the satellite rolls itself such that its attitude is most optimal to reduce the drag in the lower thermosphere. The influence of the latter two assumptions has been tested throughout this thesis. The influence of the first assumption however has not been tested yet.

Due to the symmetry of the satellite shape, an induced angle of attack is equal to an induced side-slip angle when the satellite is rolled 90 degrees. These runs have already been performed. The results are give in Figure 11.3 for both the TF and FMF. When the angle of attack rises, $C_D * A_{ref}$ increases due to the contribution of the wings. The $C_D * A_{ref}$ can increase up until 18.5% with an increase of the angle of attack to 4 degrees. When comparing the TF case and the FMF case with each other, it can be found that the $C_D * A_{ref}$ for the TF case increases slightly faster. The difference is a few percentages.

If the satellite has an angle of attack with respect to the flow, the wings generate more drag and a lift force is generated. To see what the influence is of not a perfect attitude control system, the satellite is first turned for small angles of attack and then the side-slip angle due to the wind is introduced. The results are given in Figure 11.4. The lines with a small angle of attack follow the same nearly straight lines as for the zero angle of attack case. From this it can concluded that the wind will not have an extra effect on the satellites aerodynamics, if the attitude control in terms of angle of attack varies with +- 2°. It does increase the $C_D * A_{ref}$ independent of the wind following the trend visible in Figure 11.3.

(a) In Transitional Flow.

(b) In Free Molecular Flow.
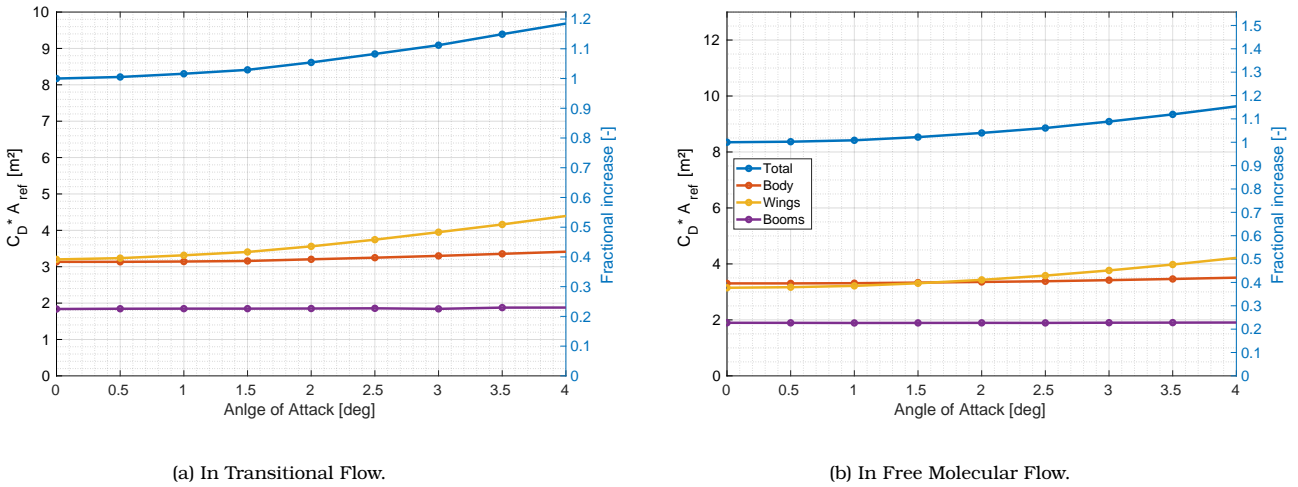
Figure 11.3: $C_D * A_{ref}$ variation with respect to an angle of attack variation of maximum $4°$.

(a) In Transitional Flow.

(b) In Free Molecular Flow.
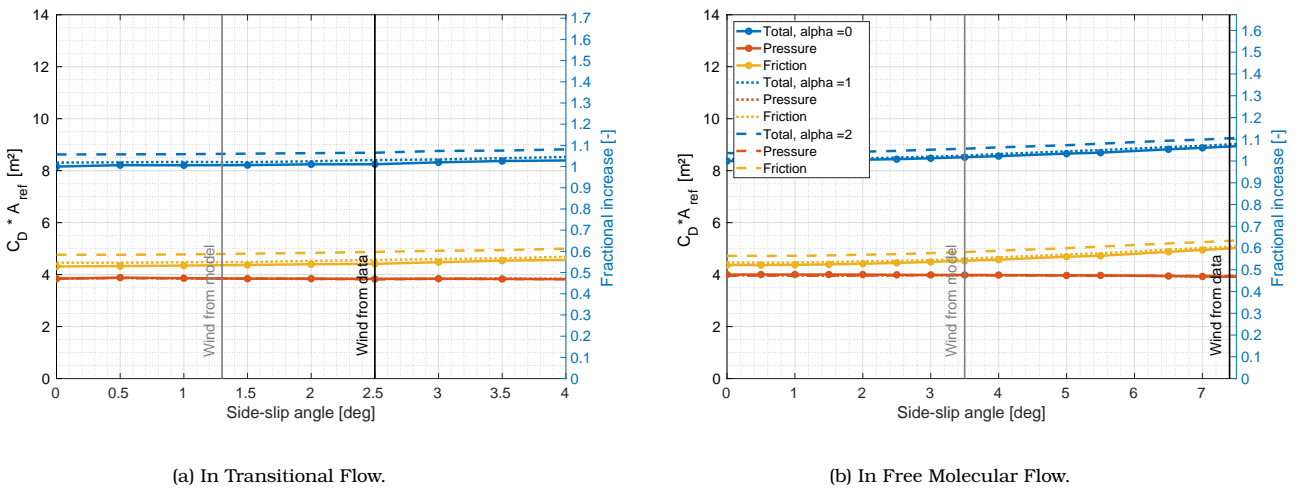
Figure 11.4: The drag coefficient times the reference area with respect to the wind induced side slip angle the angles of attack of 0 (continuous), $1°$ (dotted) and $2°$ (striped).

11.3 Summary

The influence of the orbital design choices with respect to the aerodynamics and the sensitivity with respect to the wind have been discussed in this section. It was found that the $C_D * A_{ref}$ and drag do not significantly depend on the choice of apogee altitude equal to 2200 km or 2700 km. However, it was found that the orbital decay of the semi-major axis is dependent on the apogee altitude. With increasing apogee altitude, the semi-major axis increases as well. A larger semi-major axis means a faster decay. Small variations in α only influences the drag coefficient of the satellite shape and not its sensitivity with respect to the wind.

Chapter 12

Influence of satellite geometry

Up until this point, the standard satellite shape has been used as mesh input in the simulations. However, as explained before in chapter 2, the design of the mission is still in an early phase. Therefore the geometry of the satellite is still unknown. The design depends on the instruments needed to fulfill its scientific requirements, the propulsion system used and the energy needed to keep the satellite in orbit. Apart from that, the satellite shape can be optimized for its aerodynamic properties such that the satellite will encounter the least possible drag and therefore the least possible decay. The purpose of this section is to investigate how much drag can be saved when making satellite geometry design choices. In addition, the shape variations are examined for their sensitivity to thermospheric horizontal wind and their errors.

The satellite exist of 3 parts: the body, the solar panel wings and the booms. All three parts of the satellite are analyzed individually in section 12.1, section 12.2 and section 12.3 respectively. The size of the body and the wing are most uncertain. Both parts are varied in size as explained in chapter 2.

12.1 Body variation

First of all, the influence of the body variations is discussed. The body caries the payload and therefore its assumed that the volume of the body stays constant when varying the length and cross-section of the body. Two body geometry cases are compared to the standard case. The first one has twice the length and half of the cross-section of the standard case, this was referred to as the slender body. The second one has half the length and twice the cross-section, which was referred to as the compact body. Furthermore, these three body geometries are compared to a satellite body with a smaller volume which was proposed by ESA [2020], this body was referred to as the Daedalus body.

To find the influence of solely the body, the simulations are run for the body without the wings and the booms. The first simulations are run for a side-slip angle, β, equal to 0°. The results of the pressure and frictional component of the drag coefficients for the body variations in the TF regime at 120 km altitude with respect to the respective frontal areas are given in Figure 12.1. There is a linear relation visible between the pressure component of the drag coefficient and the frontal area as can be seen in Figure 12.1a. The Daedalus body has approximately the same cross-sectional area as slender body. This results in the same magnitude for $C_{D_p} * A_{ref}$ which is half the magnitude of the $C_{D_p} * A_{ref}$ for the standard body. The compact body which has twice the cross-section with respect to the standard body also has twice the value for $C_{D_p} * A_{ref}$. From this it can be concluded that C_{D_p} stays in all cases the same and the only thing that changes is A_{ref} and increasing the cross-section of a body, linearly increases the $C_{D_p} * A_{ref}$.

In the case of the frictional component of the drag coefficient at the TF regime altitude of 120 km, given in Figure 12.1a a less clear relation is visible. When keeping the volume the same, if the frontal area decreases the length increases. Therefore, a higher C_{D_f} is expected when the frontal area is decreased. The slender body, which has twice the length, has a 20% higher $C_{D_f} * A_{ref}$. Whereas the $C_{D_f} * A_{ref}$ value for the satellite body shape with half the length of the standard body, is only 5% smaller than the nominal value. An exponential function can be recognized in these three points. From that it could be concluded that when having an even more slender and long body, the $C_{D_f} * A_{ref}$ value can be expected to increase more exponentially. In addition, when looking at the magnitude of $C_D * A_{ref}$ for both components, it should be noted that the pressure component is the main contributor to $C_D * A_{ref}$ for the standard body, compact body and the Daedalus body. Whereas, for the slender body, the frictional component is the main contributor. The total $C_D * A_{ref}$ is given in Figure 12.2a.

(a) Pressure component of $C_D * A_{ref}$.
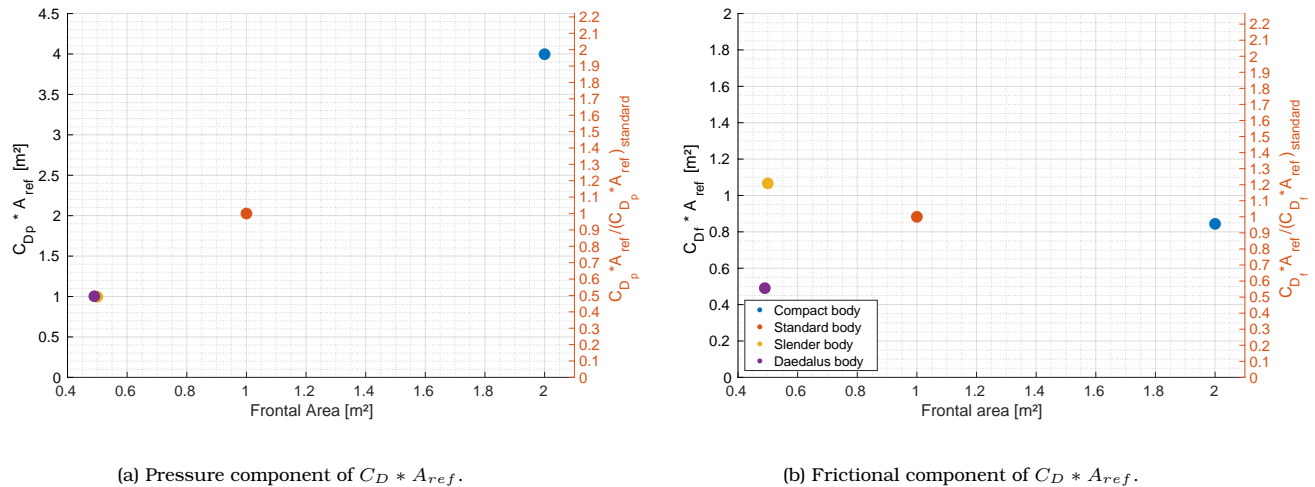
(b) Frictional component of $C_D * A_{ref}$.

Figure 12.1: Drag coefficient components with respect to the frontal area of the satellite body variations in TF.

When comparing the values of the total $C_D * A_{ref}$ in the TF regime to the results of the FMF regime in Figure 12.2b, similar relations can be found. However, the values for the total $C_D * A_{ref}$ are significantly larger for the FMF with respect to the TF. The difference of $C_D * A_{ref}$ in FMF with respect to $C_D * A_{ref}$ in the TF is in the order of [0.3-1] m^2 depending on the satellite body part size. It is important to note, that in this case only the body is being tested without the wings. When comparing the influence of the density variation on the total standard satellite shape's $C_D * A_{ref}$ in section 9.3, with respect to the impact of the density on the $C_D * A_{ref}$ of the cylinders in the validation in section 8.2, it was found that for cylinders the drag coefficient is going down with respect to the density, whereas the drag coefficient of the standard shape is going up with increasing density. The satellite body part without its solar panel wings results in a case more similar to the cylinders. It can therefore be expected that with decreasing altitude and increasing density the drag coefficient for the satellite body part goes down. On top of this, the temperature decreases when lowering the altitude, which results the drag coefficient to decrease even more. The $C_D * A_{ref}$ of the slender body shows the largest difference, equal to approximately 0.9 m^2, when going from the TF regime in Figure 12.2a to the FMF Figure 12.2b. The $C_D * A_{ref}$ for the standard body differs approximately 0.6 m^2 and the $C_D * A_{ref}$ for the compact body and Daedalus body approximately 0.4 m^2. The order in body variations from the smallest to largest difference of $C_D * A_{ref}$ when going from the TF to the FMF agrees with the order of the bodies when arranged from smallest side panel area to largest side panel area; 3.1500 m^2 (Daedalus body), 3.7477 m^2 (compact body), 5.3000 (standard body), 7.4953 (slender body). In conclusion, the larger the side panel area and therefore the frictional component of the drag, the larger is the difference in $C_D * A_{ref}$ when going from 120 km in the TF regime to 300 km in the FMF regime.
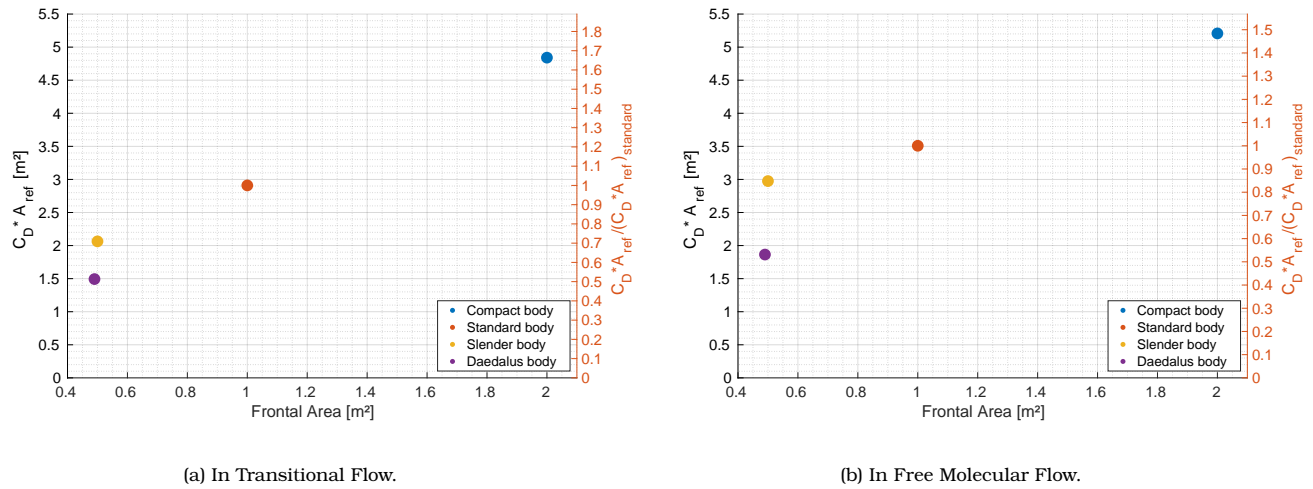
(a) In Transitional Flow.

(b) In Free Molecular Flow.

Figure 12.2: Total $C_D * A_{ref}$ with respect to frontal areas of the body variations.

Influence of body variations on cross-track wind sensitivity

As explained in section 10.1, the cross-track wind induces a side-slip angle of the satellite with respect to the gas flow. The magnitude of the maximum side-slip angle is larger in the FMF altitude range as in the TF altitude range. The results for the TF altitude of 120 km for all body variations are given in Figure 12.3a. The total C_D is decomposed in the pressure and frictional component in Figure 12.4. When looking at the three figures, the first thing that can be noted is that the pressure component has most influence on the total drag coefficient, but does not change with respect to the side-slip angle.

The frictional component however, is responsible for making the body more subjective to the side-slip angle and therefore the wind. It can clearly be seen that the steepest line (yellow) in the total drag coefficient with respect to the side-slip angle belongs to the slender body. The compact body is least subjective to wind. From this it can be concluded that when keeping the volume of the body the same, the body is most subjective to cross-track wind when its longer and thinner. However, the total $C_D * A_{ref}$ is higher for a shorter and thicker satellite body, due to the larger cross-sectional area. The worst-case magnitude of the wind obtained from in-situ data is not large enough to result in a side-slip angle so big that the $C_D * A_{ref}$ of the long slender body will exceed the $C_D * A_{ref}$ of the standard body.

Similar relations were found for the FMF case, only with larger winds, resulting in larger side-slip angles. The result for the total $C_D * A_{ref}$ is shown in Figure 12.3b. Here it can be seen that even with the maximum winds that can be found in in-situ data in the FMF at 300 km altitude, the $C_D * A_{ref}$ increase due to the wind does not exceed the $C_D * A_{ref}$ saved by the reduction of the frontal area. From this it can be concluded that, for the standard satellite shape at 120 and 300 km altitude, to save $C_D * A_{ref}$, it is more favorable to have a longer and slender body. The Daedalus body (purple) has the smallest total drag coefficient due to its smaller volume.

When comparing the results for $C_D * A_{ref}$ of the standard body, without wings and booms, with respect to the cross-track wind, with the results given in Figure 10.2a, where the body was part of the standard model, similar trends can be found. It should be noted however, that $C_D * A_{ref}$ is slightly smaller ($\pm$ 8%) for the body part without the wings and booms as found in Figure 12.3a, than the body as part of the total shape in Figure 10.2a. This is due to the fact that the frictional component of drag coefficient of the wings increases the number density above and below the wings, and therefore also slightly increases the frictional component of the body. This shows that the aerodynamics of the separate satellite parts influence each other's $C_D * A_{ref}$.

(a) In Transitional Flow
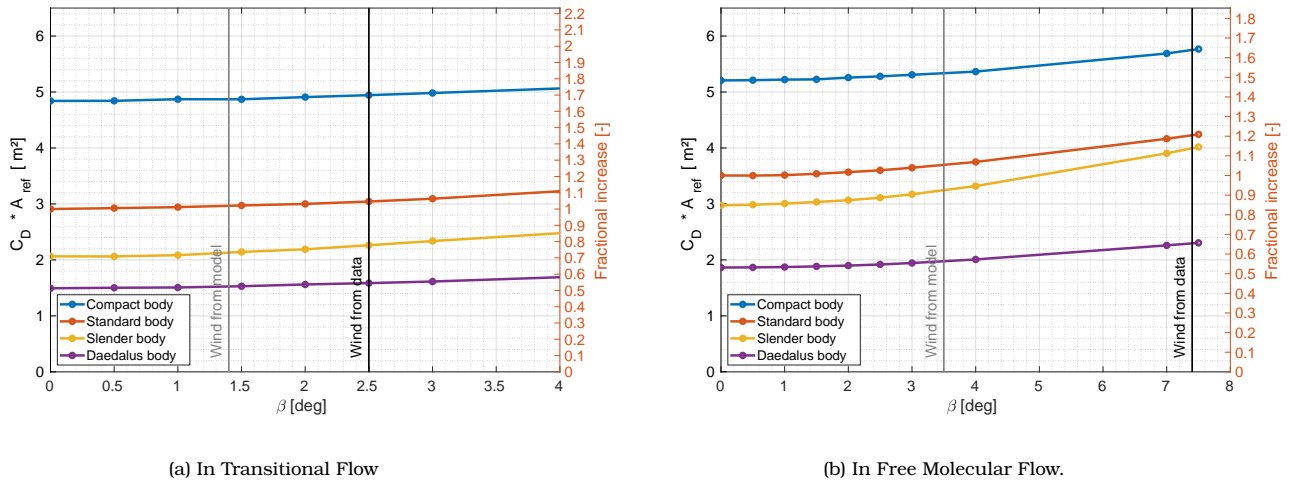
(b) In Free Molecular Flow.

Figure 12.3: Influence of the cross-track wind induced side-slip angle on the $C_D * A_{ref}$ for different body shapes. The grey line signifies the wind obtained from HWM14, whereas the black line signifies the wind obtained from the data.

(a) Pressure component of $C_D * A_{ref}$.

(b) Frictional component of $C_D * A_{ref}$.
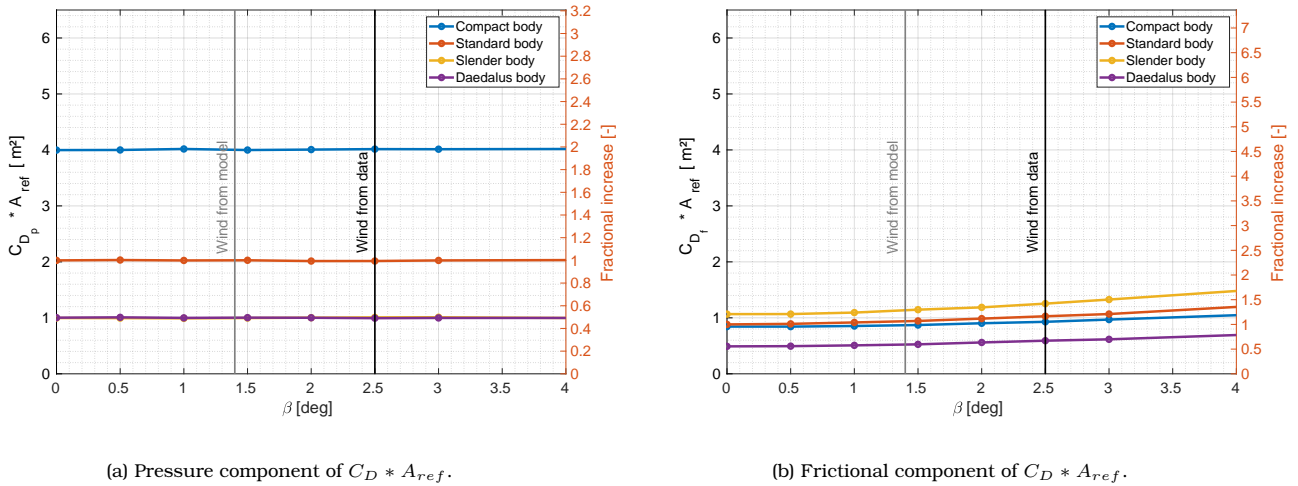
Figure 12.4: Pressure (left) and friction (right) component of the drag coefficient of the body variations with respect to the cross-track wind induced side-slip angle in the Transitional Flow. The grey line signifies the wind obtained from HWM14, whereas the black line signifies the wind obtained from the data.

Influence of body variations on in-track wind sensitivity

In this section the influence of the in-track wind on the body variation is discussed. As explained in section 10.2, the in-track wind influences the relative velocity of the satellite with respect to the atmosphere. The results for the drag coefficient with respect to the in-track wind for the satellite body variations are given in Figure 12.5. At the TF regime altitude of 120 km (a), the $C_D * A_{ref}$ decreases very little with the wind. At 300 km altitude (b), on the other hand, the magnitude of the wind is larger and therefore there is more difference visible in the $C_D * A_{ref}$. Just like was concluded in section 10.2, it can be seen that with more head wind, such that the relative velocity with respect to the atmosphere increases, $C_D * A_{ref}$ decreases. Previously it was found that this was due to the decrease of the frictional component of $C_D * A_{ref}$. As was found from Figure 12.1, the drag coefficient from the slender body (yellow) was mostly influenced by the frictional component. These two prior findings together, explains why in

Figure 12.5b the yellow line has the steepest slope with respect to the in-track wind.

(a) In Transitional Flow.
(b) In Free Molecular Flow.
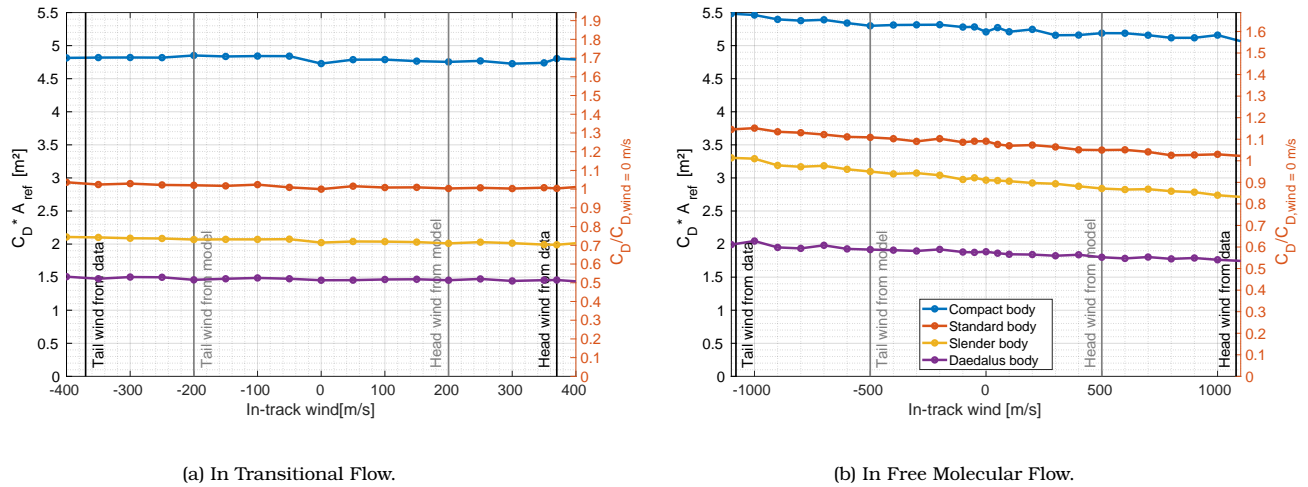
Figure 12.5: Influence of in-track wind for body variations.

The in-track wind does not only influence the drag coefficient, but also influences the total drag due to the velocity change in the drag equation. The results are given in Figure 12.6. It can be seen that the lines rise with increasing head-wind. Since the (positive) change in relative velocity is bigger than the (negative) change in $C_D * A_{ref}$, the total drag increases with an increase head wind. The drag for the satellite body with the largest cross-section, in this case the compact body, also increases the fastest with increasing head wind.

(a) Total drag in Transitional Flow.
(b) Total drag in Free Molecular Flow.
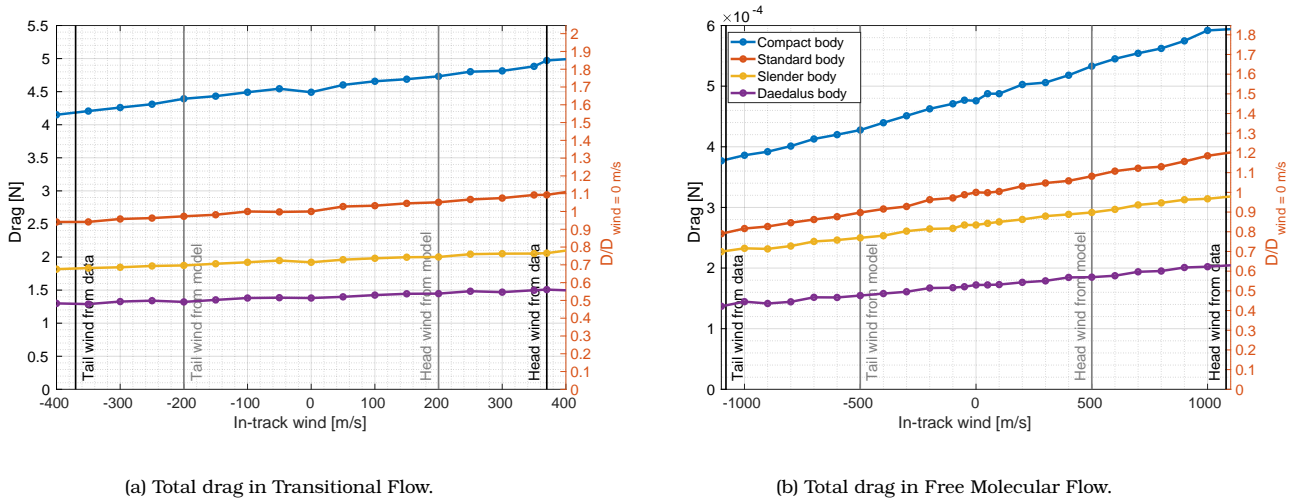
Figure 12.6: Influence of in-track wind for body variations.

12.2 Solar panel wing variation

From earlier analyses of the sensitivity of the drag to the thermospheric conditions, it was found that the large wings of the standard model as defined in this thesis, increase the sensitivity of the drag to

density, the gas temperature and the gas composition due to the increase in the frictional component of the drag coefficient. In addition, it was found that the large solar panel wings can make the satellite more subjective to wind which increases the drag as well. For a mission like Daedalus the large wings are necessary to obtain enough energy to stay in orbit. Therefore, in this section, the influence of the size of the wings on the aerodynamics of the satellite is further investigated.

The wing variations have been explained in chapter 2. The influence of the thickness as well as the area of the wing is tested in this section. The wing variations are tested on their influence on the total drag as well as on the sensitivity of the satellite shape to wind.

12.2.1 Wing thickness variations

The thickness of the wings is varied from $0.01\ m$ to $0.06\ m$. In Figure 12.7, the result of the simulations of the $C_D * A_{ref}$ for various wing thicknesses is given for the TF altitude case and FMF altitude case. On the bottom x-axis of Figure 12.15b, the wing thickness is given. This is directly related to the frontal area of the satellite. The frontal area is plotted on the top axis. It should be noted that by increasing the wing thickness (and therefore frontal area) the frictional component, $C_{D_f} * A_{ref}$, stays practically the same, whereas the pressure component, $C_{D_p} * A_{ref}$, increases with nearly 5% per 2 cm. An increase in thickness of 2 cm is equal to an increase in the affected area of approximately 5%. From this it can be concluded that the $C_{D_p} * A_{ref}$, just as with the body variation, is linearly dependent on the frontal area. Even though A_{ref} increases with almost 5% for 2 cm thickness increase, $C_{D_f} * A_{ref}$ increases less than 1%. Therefore it can be concluded that the frictional component of the drag coefficient, C_{D_f}, decreases with increasing of the thickness.

To test the influence of the wing thickness, the complete satellite shape is taken into account. The increase in the total $C_D * A_{ref}$ can better be seen in Figure 12.7b. It can be concluded that the C_D increases approximately 3% per 2 cm. This is because the frictional component is the dominant component and does not change significantly (1% >) with increasing thickness. In addition, the increase seems to be slightly higher for the TF case than for the FMF case, however since this is only one percent difference, no strong conclusions are linked to this finding.
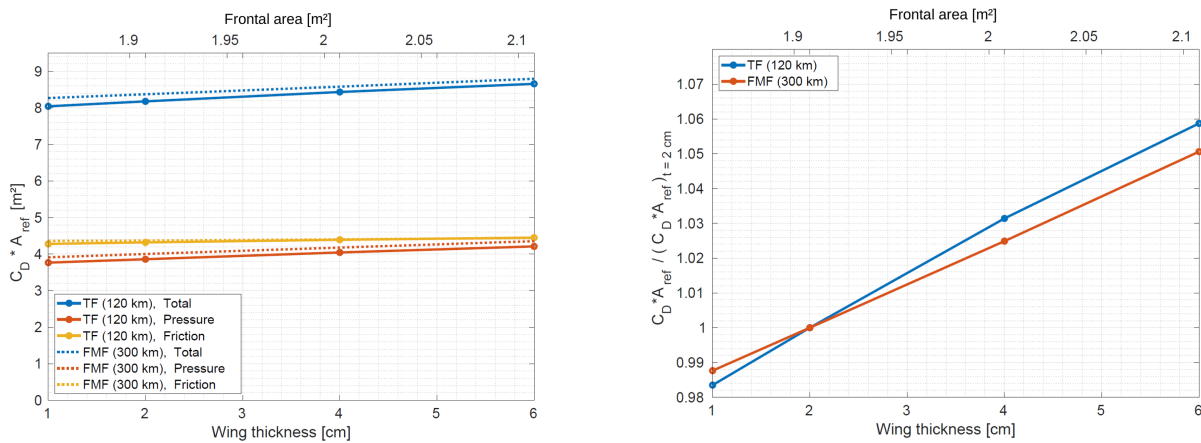
(a) $C_D * A_{ref}$ with respect to wing thickness (bottom x-axis) and frontal area (top x-axis) of the body including the two wings and booms.

(b) Factorial increase of $C_D * A_{ref}$ with respect to a wing thickness of 2 cm.

Figure 12.7: Influence of the wing thickness on the satellite's $C_D * A_{ref}$ for TF and FMF, roll = 0° and β = 0°.

Influence of thickness on cross-track wind sensitivity

Next, the influence of the thickness variation on the sensitivity of the satellite shape with respect to the wind is examined. The goal of this section is to find out if the thickness of the wings makes the satellite

more or less subjective to cross-track wind. The simulation is run for all thickness variations for the various side-slip angles induced by the thermospheric wind. From the section 10.1, it was found that the roll angle has a huge influence on $C_D * A_{ref}$ of the wings and therefore, the simulations are run for both 0° roll angle and 90° roll angle. The results for the various thickness with respect to the side-slip angles are given in Figure 12.8a for a roll angle of 0° and in Figure 12.8b for a roll angle of 90° for the TF.

(a) Roll angle = 0°.

(b) Roll angle = 90°.

Figure 12.8: Sensitivity of C_D to side-slip angle per wing thickness for roll = 0 and roll = 90° at 120 km altitude in TF.

The nominal run with the standard model is the dark orange line. For all thickness variations, the $C_D * A_{ref}$ with respect to the side-slip angle follows approximately the same trend as for the standard case. From this it can be concluded that the difference in the thickness does not have a significant influence on the sensitivity with respect to the wind neither for a roll angle of 0° or a roll angle of 90°.
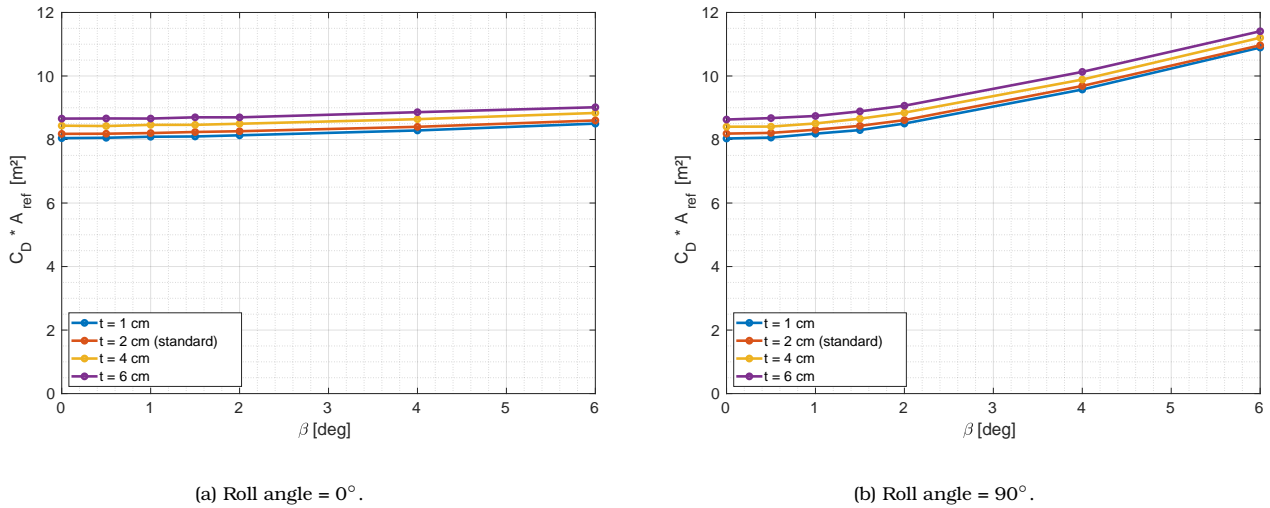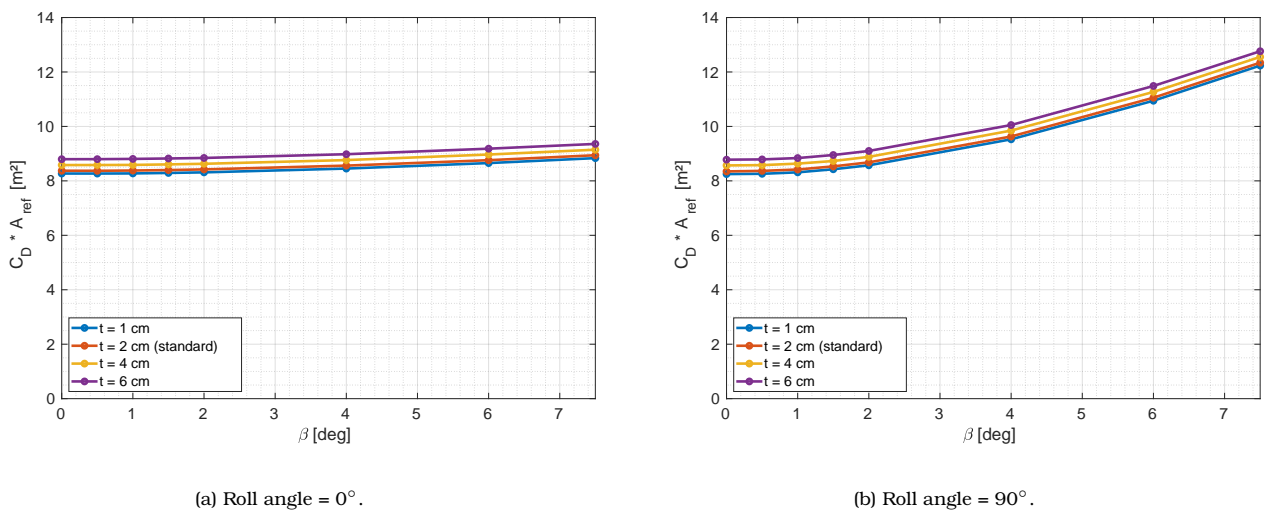

(a) Roll angle = 0°.

(b) Roll angle = 90°.

Figure 12.9: Sensitivity of C_D to side-slip angle per wing thickness for roll = 0 and roll = 90° at 300 km altitude in FMF.

The results for the FMF are given in Figure 12.9. Here, just as for the TF, the thickness does not have

a significant influence on the satellite's sensitivity to the cross-track wind.

Influence of thickness on in-track wind sensitivity

Now simulations are performed to investigate the influence of the wing thickness on the sensitivity to the in-track wind. These simulations are performed for 0° side-slip angle and roll angle. When looking at the in-track wind sensitivity in Figure 12.10, something similar can be found as was seen for the cross-track wind sensitivity. The simulations for the various thicknesses show a similar trend as the standard (dark orange) one, only with a different value for $C_D * A_{ref}$ for no in-track wind. Since the thickness only influences the $C_D * A_{ref}$ and not other parameters in the drag equation from Equation 6.1.4, that it can be concluded that it neither has an influence on the sensitivity of the satellite's drag to the wind.

In general it can be concluded that the thickness of the solar panel wings, within a range of 1-6 cm, mainly influences the magnitude of $C_D * A_{ref}$ due to the change in A_{ref}. In addition, the thickness of the wings within this range do not make the satellite more or less subjective to wind. By decreasing the thickness of the wings, the $C_D * A_{ref}$ will be decreased as well.

(a) Drag coefficient in Transitional Flow.   (b) Drag coefficient in Free Molecular Flow.
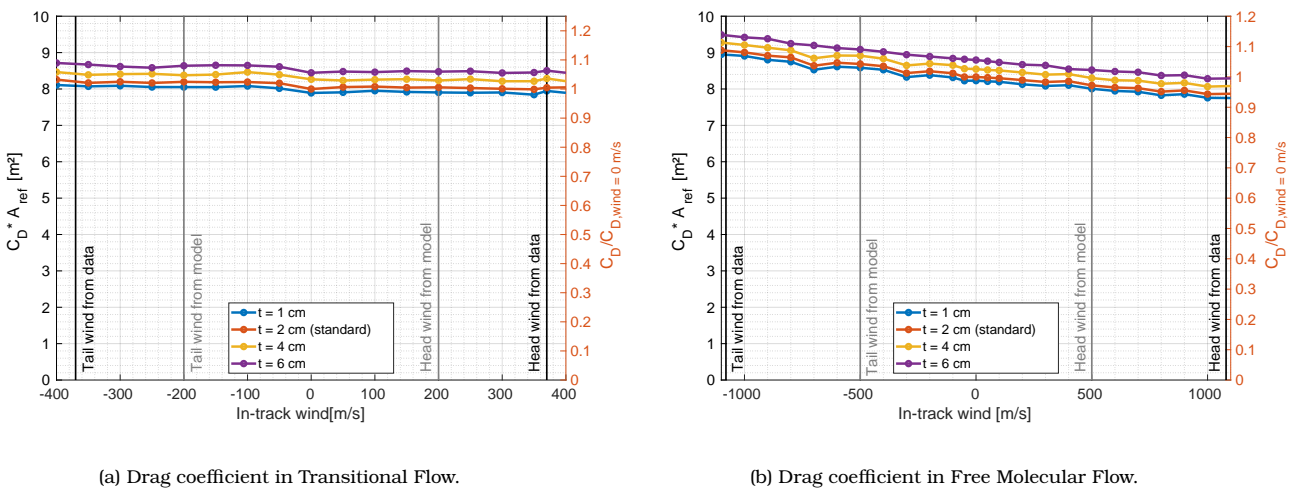
Figure 12.10: Influence of in-track wind for various wing thicknesses.

12.2.2 Solar panel wing area variations

Next to the thickness, the area of the wings can also be varied. The wings are varied by changing the wingspan as explained in subsection 2.2.2. The five different wingspans (per wing) chosen are 0.7, 1.3, 1.9, 2.5 (standard) and 4 m. These approximately correspond to effective energy producing panel areas of 6.6, 12.3, 18.0, 23.7 and 37.9 m^2. It can be assumed that the effective energy producing area is approximately equal to only the bottom or only the top side of solar panels. The results of the solar panel wing size is given in Figure 12.11. The frontal area is given in the top x-axis and the total wing area (top and bottom) are given in the bottom x-axis. When looking closely $C_{D_p} * A_{ref}$ is slightly increasing with the increase of the frontal area, just as was the case with the increasing thickness.

From previous analysis it was found that the wings are responsible for the large contribution of the frictional component to the drag coefficient. By increasing the wing area it can be expected that the frictional component increases. This is what can be seen in Figure 12.11a. The total drag $C_D * A_{ref}$, increases significantly, almost linearly, with wing area, due to the increasing frictional component. In Figure 12.11b, the increase in $C_D * A_{ref}$ is shown for the TF and the FMF. It can be seen that decreasing the wing area by half, will result in a reduction of approximately 20% of the $C_D * A_{ref}$ and therefore the drag.

From ESA [2020], it was found that the effective energy producing area should be between 15-23 m^2. This requirement of Daedalus would correspond to a total wing area (top and bottom) between 30 - 46 m^2. These values for the total area can be found in Figure 12.11. The wing size of the standard shape as defined in this thesis is approximately the same size as the upper boundary of the estimation by ESA [2020]. When choosing the lower boundary of the wing area estimation, corresponding to total area of 30 m^2, 14% of the drag can be saved when assuming FMF at 300 km altitude and 16% of the drag can be saved when assuming TF at 120 km altitude, for the nominally defined parameters at the respective altitudes. In addition, the frictional component decreases, so it can be expected that the satellite will be less subjective to the variability of the thermospheric parameters as discussed in chapter 9.
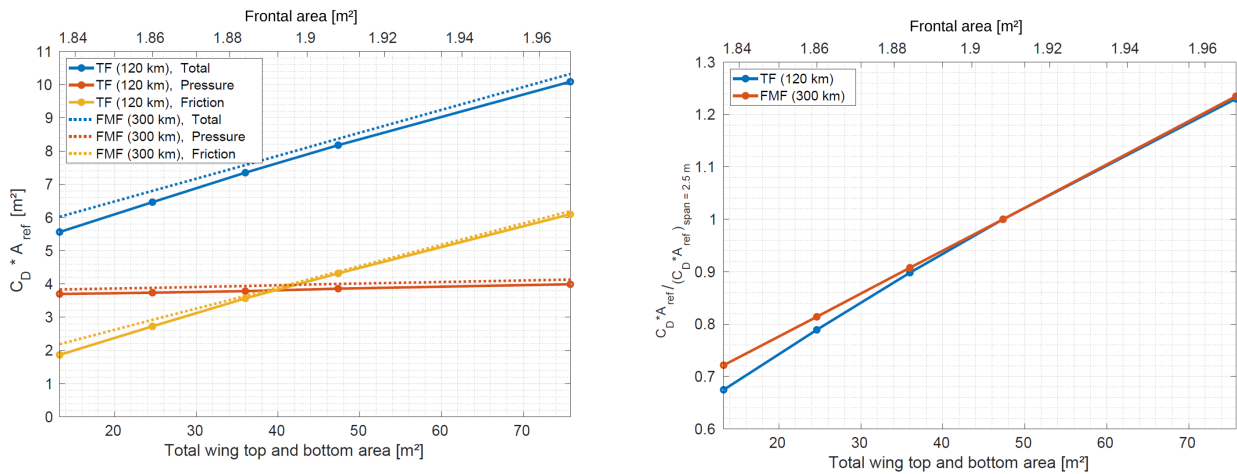
(a) $C_D * A_{ref}$ with respect to wing wing area due to span width change (bottom x-axis) and frontal area (top x-axis) of the body including the two wings and booms.

(b) Factorial increase of C_D with respect to a single wingspan of 2.5 m and a total wing area, top an bottom, of 47.36 m^2.

Figure 12.11: Influence of the wing thickness on the satellite's C_D for TF and FMF, roll = 0° and β = 0°.

Influence of wing span variation on cross-track wind sensitivity

Keeping in mind that changing the wing area by changing the wingspan, mostly influences the frictional component of $C_D * A_{ref}$, it is interesting to investigate the influence of the cross-track wind on the satellites dynamics for various wingspans. To do this, the standard models with varying wingspan are run for multiple side-slip angles, β. This is done for the two cases of roll angle is 0 and roll angle is 90°.

From section 10.1, it was concluded that the cross-track wind does not seem to have much influence on the satellite's $C_D * A_{ref}$ for the TF altitude case at roll = 0°. This is also the case for the satellite shape variations with different wingspan as can be seen in Figure 12.12a. The distance between the lines corresponding to the various wingspans stays approximately constant. This difference in $C_D * A_{ref}$ can be derived from the satellite geometry difference independent of the wind. A similar conclusion can be drawn from Figure 12.13a, which shows similar results for the FMF altitude case.

The results of the $C_D * A_{ref}$ for roll = 0° for the TF and FMF altitudes are compared to the results after rolling the satellite 90°. The results are given in Figure 12.12b for the TF altitude of 120 km and Figure 12.13b for the FMF altitude of 300 km. It was already concluded that rolling the satellite with a 90° angle has a huge influence on the sensitivity of the satellite with respect to the wind. From these figures it can be concluded that this sensitivity with respect to the wind increases when increasing the span width, as could be expected.

(a) roll = 0°.   (b) roll = 90°.
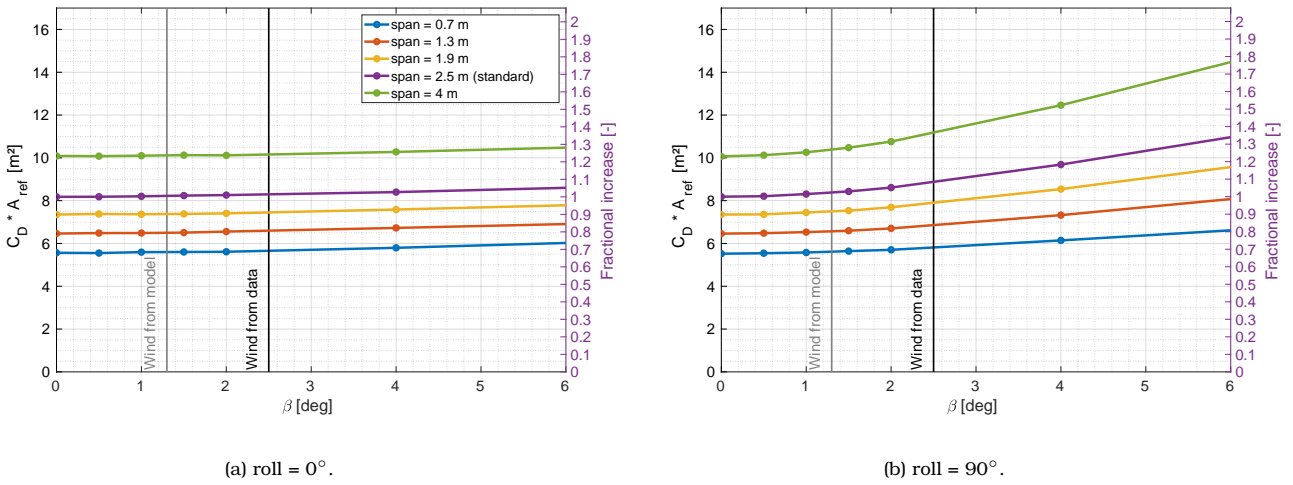
Figure 12.12: C_D with respect to side-slip angle for wing area variations in the TF at 120 km altitude.

(a) Roll = 0°.   (b) Roll = 90°.
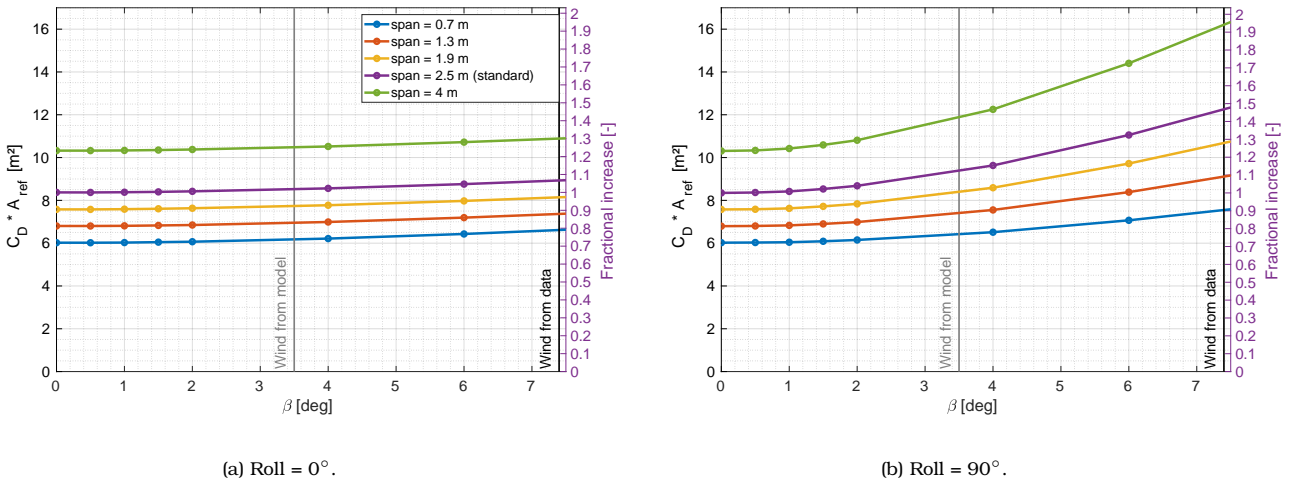
Figure 12.13: C_D with respect to side-slip angle for wing area variations in the FMF at 300 km altitude.

The magnitude of the increment due to the wind per wing area variation is given for both the TF and the FMF altitude in Figure 12.14 for roll = 90°. From these plots, it can be concluded that it is important to keep in mind that the wing variation does not only influence the $C_D * A_{ref}$, it also makes the satellite more subjective to wind when the satellite is rolled 90°. It was found in section 6.2 that the decay of a satellite like Daedalus is mostly due to the drag that the satellite encounters below 200 km altitude. At 120 km altitude, increasing the wingspan from 2.5 meter to a 4 meter span results in an increment of $C_D * A_{ref}$ with more than 23% from 8.2 to 10.1 m^2. At the same time, when large winds occur an increment of another 11% in the $C_D * A_{ref}$ can be expected.

The grey lines in Figure 12.14 signify the maximum wind from the model and the black line signifies the maximum wind from the data. When taking into account the wind from the model only, the increments of the drag coefficient with respect to the wind is very small for the wing variations, within the range of [1.6, 3.2]% for the maximum wind. With that information it could be decided to neglect the influence the wind has on the satellite shape, independent of the roll angle and independent on the wing size.

However, when looking at the side-slip angle due to the maximum wind from the data, the range for the increment due to the wind for the various angles in between [5.2, 11.2]%. An 11% in the C_D due to large winds, for example when the satellite flies through a geomagnetic storm, is equal to an 11% increase in the orbital decay for that orbit. This is important to take into account while designing the satellite.

In comparison, at the FMF altitude of 300 km, due to the larger winds, an increment of another 58% can be the result of the winds on top of the 23% that was the result of only increasing the wing span from 2.5 to 4 m. Even though it is important to remember that these values for the FMF are much bigger, they will have less influence on the drag due to the density which is 4 orders of magnitude smaller.

In the scope of Daedalus, it was previously found that, when deciding on the solar panel area within the expected range of 30 - 46 m^2, ±16% of the drag could be saved at 120 km altitude when taking a solar panel area of 30 instead of 46 m^2. On top of this, when looking at Figure 12.14a, it can be found that instead of an increment of $C_D * A_{ref}$ of 8.5% (purple line) due to the worst-case cross-track wind, the increment will be ±7% (between dark orange and yellow line).

(a) In Transitional Flow at 120 km altitude.

(b) In Free Molecular Flow at 300 km altitude.
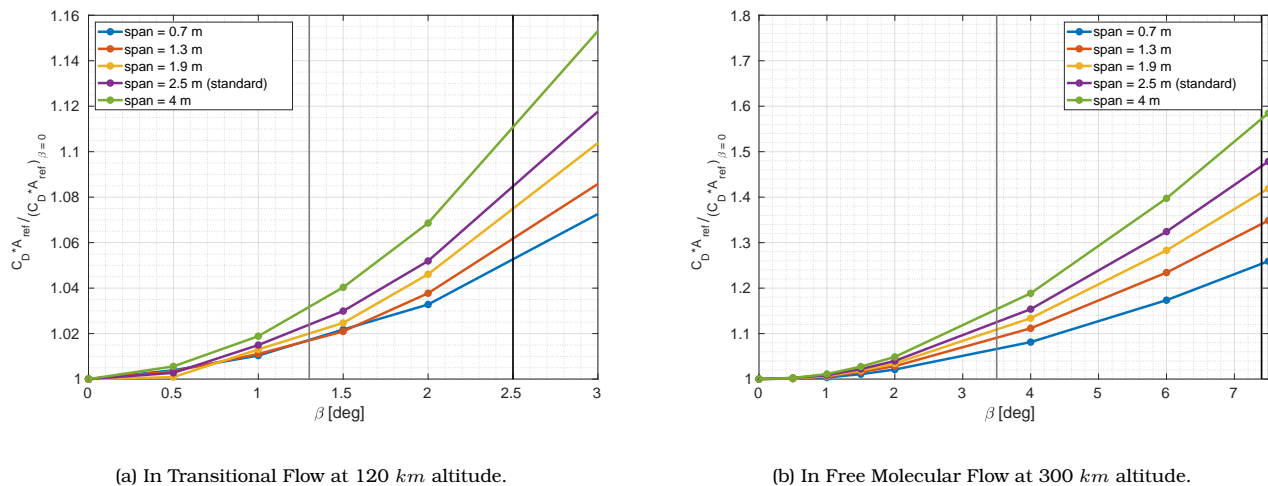
Figure 12.14: $C_D * A_{ref}$ increment, in graph shown as of due to wind for wind induced side-slip angles. The grey line signifies the wind obtained from HWM14, whereas the black line signifies the wind obtained from the data.

Influence of wingspan on in-track wind sensitivity

Next, just as for the wing thickness and body variations, the influence of the wingspan on the sensitivity of the satellite to the in-track wind is tested. First of all, the results for the $C_D * A_{ref}$ are discussed, which are followed by the results for the total drag that are obtained by the value for $C_D * A_{ref}$ and the new relative velocities in the drag equation.

The results for the $C_D * A_{ref}$ are given in Figure 12.15. On the left side the TF case is shown. The lines show a slight decrease with increasing head wind within the range of 5%. This is extremely small. The right graph shows the FMF altitude case. Due to the larger winds there is a clearer trend visible. The $C_D * A_{ref}$ for the satellite shape with the largest wingspan seems to decrease the fastest. This is because the large wings correspond with a large frictional component of the drag coefficient. Increasing the relative velocity of the satellite with respect to the flow reduces the frictional component. Here it is shown that the larger the frictional component, the faster it reduces as well.
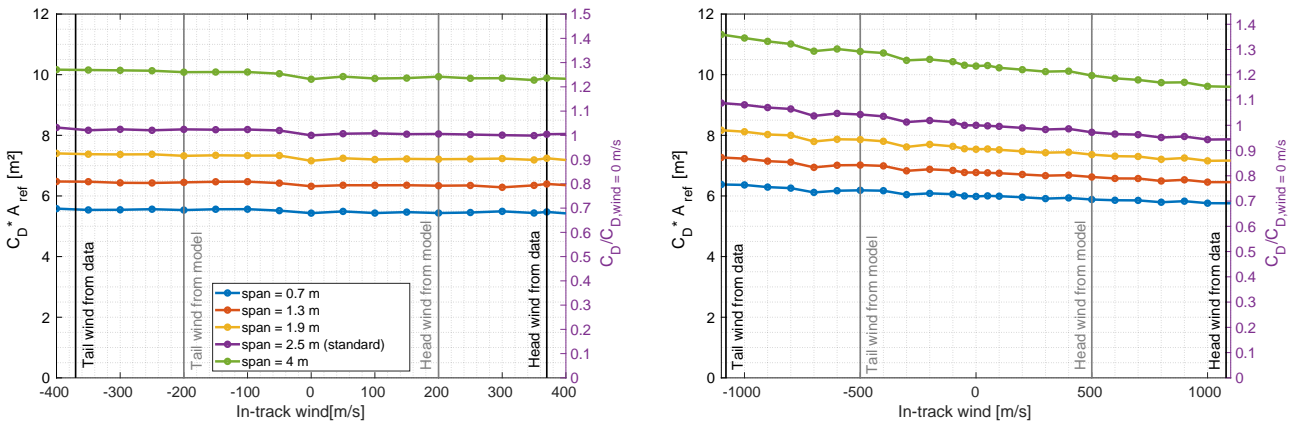
(a) $C_D * A_{ref}$ in Transitional Flow at 120 km altitude.

(b) Drag coefficient in Free Molecular Flow at 300 km altitude.

Figure 12.15: Influence of in-track wind on the drag coefficients for various wingspans.

The total drag for the various solar panel wing area variations with respect to the in-track wind is given in Figure 12.16. The leading factor in the trends is the change in the relative velocity of the satellite with respect to the flow, due to the in-track wind. The factorial increase is approximately the same for all wingspan cases.
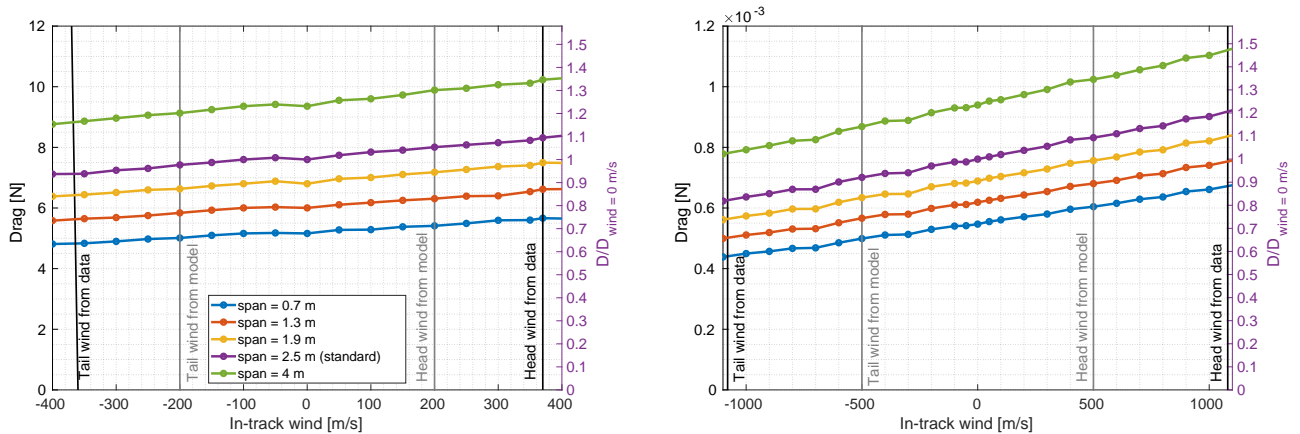
(a) Total drag in Transitional Flow.

(b) Total drag in Free Molecular Flow.

Figure 12.16: Influence of in-track wind on the total drag for various wingspans.

12.3   Boom contribution

The boom configuration is kept constant over all the cases, in terms of body variations, flow regimes and wind angles, that have been discussed in this thesis. The booms are symmetric around the x-axis. That is the reason why there is no difference expected in the contribution of the booms with respect to the satellite drag when rotating the satellite around its x-axis (in roll) with 90°.

In chapter 9, the sensitivity of the total $C_D * A_{ref}$ with respect to the thermospheric conditions have been tested. The contribution of the booms have been constant throughout the analysis on a value for

$C_D * A_{ref}$ of approximately 1.8 m^2 for the TF case and 1.9 m^2 for the FMF case.

Similar results can be found when looking at the results of the influence of the wind in chapter 10. In that chapter, all the parts of the satellite body have been examined for their contribution to the C_D*A_{ref}. When looking closely to the graphs found in that chapter it can be seen that the $C_D * A_{ref}$ of the booms in all cases changes a maximum of 0.1 m^2, which is negligible with respect to the total $C_D * A_{ref}$, which equals 8.5 or more. Furthermore, the change in $C_D * A_{ref}$ due to the booms is much smaller than the changes due to the wings or the body itself. From this it can be concluded that the booms can be taken into account as a constant value in the total $C_D * A_{ref}$, one that is not subjective to the thermospheric conditions or wind. The value for $C_D * A_{ref}$ depends on the configuration and size of the booms. In this case, the booms with a total frontal area of approximately 0.8 m^2, have a contribution to the total $C_D * A_{ref}$ of approximately 2 m^2.

12.4   Summary

The following conclusions can be drawn about the satellite shape design with respect to its aerodynamics and sensitivity with respect to the wind. To save drag, it was concluded that it was better to have a long and slender body, than a shorter, but thicker body. This does increase the sensitivity with respect to the wind. However, even when the body's length is multiplied by two and its cross-sectional area is halved, the sensitivity with respect to the wind does not exceed the drag saved by decreasing its cross-section.

Next, the thickness increases the total $C_D * A_{ref}$ with 3% per 2 added centimeters for this wing size, but do not make the satellite more sensitive to the wind. The size of the wings have a huge influence on the total $C_D * A_{ref}$. Furthermore, when the satellite is rolled 90°, the cross-track wind influence is between 5-11% depending on the wing size. Finally, the in-track wind influences the drag mainly due to the change in relative velocity. This means that actual drag for a satellite shapes with already a higher $C_D * A_{ref}$ will increase more due to the in-track wind, than a satellite with a smaller $C_D * A_{ref}$.

Chapter 13

Conclusions and recommendations

The lower thermosphere (100 - 200 km) is the most undiscovered region of the Atmosphere. This region is characterized by the high energy inputs from the Sun, in the form of energized ions at the poles and solar radiation at the Sun-facing side of the Earth. This results in space weather. Space weather can result in the colorful auroras that have fascinated people throughout the ages. On the other hand, it can endanger the safety of electrical grids on Earth and the safety of the astronauts and satellites in Space. Therefore, it is important to get a better understanding of the lower thermosphere and the processes that take place there.

Space weather influences the thermospheric conditions. This results in a region where density, temperature and composition are extremely variable with time and location and unevenly distributed. Consequently, high winds can occur from high to low pressure areas and around the poles. To get a global understanding of this area, a continuous and global data set is needed that covers all (geomagnetic) conditions, which can be obtained by a satellite, like the proposed ESA mission, Daedalus.

The satellite's scientific purpose would be to investigate the electrodynamics and neutral processes in the region. However, designing such a satellite that at the same time is affected by the uncertainties in the dynamics and variability of the thermosphere is a real challenge. The satellite can decay due to aerodynamic drag as a result of high densities or wind. In the introduction of this thesis, the research objective has been stated. The purpose of this thesis is:

To investigate the influence of the horizontal wind and the errors in the horizontal wind models on satellite aerodynamics at an altitude of 100 – 150 km.

The research questions that needed to be answered to fulfill the research objective were:

1. What is the wind magnitude and direction that the satellite can encounter during its lifetime?

2. What are the errors and uncertainties in the wind models?

3. How do the thermospheric conditions in the region of 100-150 km and their variability affect the satellite's aerodynamics?

4. How does the wind influence the aerodynamics of a general satellite shape and orbital parameters?

5. What are the influences of the design variables, like apogee altitude, attitude and satellite shape, on the aerodynamics of the satellite and its wind sensitivity?

To answer these questions, the research consisted of a literature study, data analysis and computational

modeling part. The focus is on the altitude region of 100 -150 km. There, the flow is in a so-called Transitional Flow (TF) regime between the Free Molecular Flow (FMF) above and the Continuous Flow below. Since this is still a fairly unknown region the differences with respect to the FMF, which is a more observed regime, are highlighted. The conclusion given here will be based on results for the aerodynamics at a perigee altitude of 120 km, within the TF regime, and the comparison with a perigee altitude of 300 km,within the FMF regime, but will not quantify the aerodynamics at 300 km specifically.

The focus of this thesis is primarily on the influence of wind on the drag, because the orbit of a low Earth orbiting satellite is, after the gravitational force, most affected by the aerodynamic drag. The wind influences the drag by changing the relative velocity in the drag equation and by changing the product of the drag coefficient times affected area ($C_D * A_{ref}$) from the drag equation. There is no analytical expression available for the drag coefficient in the TF regime. Therefore a computational method, using SPARTA, has been proposed to obtain $C_D * A_{ref}$ of a specific satellite shape made in Blender.

Since Daedalus is still in an early design phase, the satellite shape is not fixed yet. The nominal satellite shape, or standard shape, that has been used in this thesis is a slender body based on the measurements of the body of GOCE with relatively large solar array wings and six booms to measure the electrical field. The influence of variations from this satellite shape have been tested.

In this chapter, the conclusions of the thesis are stated that answer the research questions. They are structured from a mission design point of view. First of all, the influence on the aerodynamic drag of the uncertainties in the thermospheric conditions are discussed. Secondly, the impact of the mission design choices (apogee altitude, attitude, satellite shapes) on the drag is discussed with the assumption that there is no wind. Thirdly, the wind from models and in-situ data is introduced and the influence that the wind has on the design choices is discussed.

In conclusion, recommendations are given on how the mission design can be simplified. In addition, drag reduction considerations are discussed. Finally, the recommendations are given for future research in the scope of topic.

13.1 Sensitivity to thermospheric variability

From the drag equation and analytical expressions for C_D, under the assumption of a FMF regime, it is shown that the drag, next to the wind, also dependents on the thermospheric conditions; gas temperature, composition and density, and the gas-surface collision parameters. The thermospheric conditions are dependent on the location, time, geomagnetic activity and solar radiation power. In order to find the influence of the wind, it is necessary to decide upon a nominal value for all thermospheric parameters. These have been based on typical values during geomagnetic quiet time. The sensitivity of the $C_D * A_{ref}$ with respect to the thermospheric parameters has been tested, to see how the nominal results can change depending on the thermospheric conditions. Even though these parameters are interdependent, in this thesis they have been tested separately to quantify the influence that each of them has on the satellite aerodynamics.

The following conclusions have been drawn on the influence of the variability of the separate thermospheric parameters on the $C_D * A_{ref}$ of the standard satellite shape with respect to its nominal value of ± 8.2 m^2 at 120 km altitude and ± 8.4 m^2 at 300 km altitude:

1. In the TF, $C_D * A_{ref}$ has proven to be most sensitive to the variability of the density in that area. The range of values for $C_D * A_{ref}$ computed with the maximum and minimum density found in that region is [6.80,8.79] m^2, which results in a sensitivity index with respect to the $C_D * A_{ref}$ with the nominal density of 0.24.

2. The sensitivity of $C_D * A_{ref}$ to the total variability of the thermospheric gas temperature was 0.075 at the TF altitude. It was found that the increase in $C_D * A_{ref}$ for both the TF and FMF altitude is approximately 2.5% per 100 K from the nominal value.

3. The sensitivity of $C_D * A_{ref}$ to the composition between high and low geomagnetic activity is negligible (0.01) at the TF altitude.

4. The TF case of 120 km is compared to a FMF case of 300 km altitude. The range for the thermospheric parameters depending on the geomagnetic activity, location and time increases with increasing altitude. Because of this, the sensitivity in the FMF with respect to the thermospheric gas temperature and composition is larger than in the TF. The density for the FMF, on the other hand, is extremely low and no intermolecular collisions take place. Because of this it was found that the variability of density at 300 km altitude, unlike at 120 km, does not influence the $C_D * A_{ref}$.

5. Due to the large wings of the standard satellite shape, the contribution of the frictional component of $C_D * A_{ref}$ is significant. It was found that the assumption of a 100% atomic Oxygen composition can increase $C_D * A_{ref}$ with 7.5% at 120 km and 3.7% at 300 km. Therefore, for a similar satellite shape as proposed in this thesis with large wings, the assumption of a 100% atomic oxygen composition might not be valid for neither the TF nor the FMF.

6. The thermospheric parameters mostly influence the frictional component of the drag coefficient. The large frictional component is due to the large wing area that is expected for a mission like Daedalus. With a smaller wing area it could be expected that the sensitivity with respect to the geomagnetic activity and day-night variations in terms of thermospheric parameters is lower. This should be further investigated, and is therefore elaborated upon in the recommendations

As mentioned before, the thermospheric condition parameters never change separately, but always together. With increasing geomagnetic activity, the temperature increases at high latitudes, the density increases, and consequently the composition changes to a more molecular composition. When solely looking at the drag coefficient, it was found that the total sensitivity index of $C_D * A_{ref}$ between low and high geomagnetic activity is higher for the FMF than for the TF. In other words, it is expected that $C_D * A_{ref}$ changes more depending on the geomagnetic activity at higher altitudes in the FMF than at lower altitudes in the TF. An increase in the drag coefficient has a linear relation with the drag.

However, at higher altitudes the density is much lower, in the range of 2.13e-12 and 2.66e-10 kg/m^3. This results in very low values for drag. It was therefore also found that for a highly eccentric orbit with a low perigee like the one for Daedalus, 96% of the orbital decay is due to the drag at altitudes lower than 150 km. Even though $C_D * A_{ref}$ is more variable at higher altitudes, it will have less influence on the total drag that the satellite will encounter during one orbit.

Finally, when speaking about total drag, it is important to note that the density does not only influence $C_D * A_{ref}$, but is also found in the drag equation directly. The range of densities found at 120 km is between 5e-9 kg/m^3 and 5e-8e kg/m^3. This means that the density can increase by a factor of 10. Because the density and drag are proportionally related, the drag then also increases by a factor of 10.

13.2   Influence of mission design choices on aerodynamics, assuming no wind

The design choices that are expected to influence the aerodynamics and that are still open to be optimized for Daedalus are the shape of the satellite, its attitude and the apogee altitude.

Starting with the apogee altitude, it is still under discussion if an apogee altitude of 2700 km or 2200 km should be selected. It was found that the apogee altitude does not have a significant influence (less than 1%) on the drag coefficient for both the TF case and the FMF case. In addition, the influence on the drag of the relative velocity due to the change in apogee altitude is also equal to approximately 1%. It can therefore be concluded, that in terms of drag, the apogee altitude has a negligible influence. However, the apogee, when keeping the perigee the same, influences the semi-major axis. A larger semi-major axis results in a faster decay. Therefore, the satellite would need more propulsion to stay in the

originally designed orbit. It will, on the other hand, result in a longer orbital lifetime, since the satellite has more distance from the Earth before it completely decays.

Secondly, it was found that small variations in the angle of attack result in a slight exponential increase (as part of a sine wave) in $C_D * A_{ref}$. An increase in angle of attack of $4°$ of the standard satellite shape can increase the $C_D * A_{ref}$ with almost 18.5%. This is something that should be taken into account when designing the attitude control system of the satellite.

Thirdly, the variations of the satellite shape have been tested. The main variations that are possible and interesting to discuss are variations in the body length over diameter ratio and the solar array wing size and thickness. The following conclusions have been drawn:

1. For the body variations, it was found that the pressure component, $C_{D_p} * A_{ref}$, of the $C_D * A_{ref}$ is linearly dependent on the cross-sectional area with respect to the flow, A_{ref}. Consequently, C_{D_p} stays the same for all cases.

2. The total $C_D * A_{ref}$ and therefore the drag decreases with increasing the length/cross-sectional area ratio. When the cross-sectional area is smaller, to keep the same volume, the length of the satellite needs to be larger. Increasing the length of the satellite, enforces the frictional component of $C_D * A_{ref}$. It was found that $C_{D_f} * A_{ref}$ of the body part increases at a slower pace than A_{ref} decreases. The reduction of $C_D * A_{ref}$ of the satellite body part when the length is doubled and the cross-section is halved is 30% of the nominal value of approximately 3 m^2. This is a total reduction of the $C_D * A_{ref}$ of the complete standard satellite shape of 10%, assuming the $C_D * A_{ref}$ contribution of wings and booms stay the same.

3. It has been concluded that the total $C_D * A_{ref}$ increases with 3% per 2 added centimeters solar array wing thickness. This is partly due to the increase in A_{ref}, which is 5% per added 2 cm and partly due to the reduction of the frictional component.

4. The wing area, expressed in span width, was found to have a significant influence on the total $C_D * A_{ref}$, due to the change in the frictional component. In the FMF it was found that $C_D * A_{ref}$ of the satellite is linearly dependent with the wing area. The $C_D * A_{ref}$ for the satellite at the TF altitude of 120 km, shows a slight curve. In other words, the $C_D * A_{ref}$ increases slightly faster with increasing span width in the TF than in the FMF.

5. A reduction of approximately half the area of the wings results in a 20% reduction of the drag. The energy-generating area of the solar panels is assumed to be half of the total solar panel area, which is the bottom area plus the top area of the wings. This means that this would also halve the energy-generating area. In the scope of Daedalus, the estimated range for the energy generating area is 15-23 m^2. The difference in the total $C_D * A_{ref}$ of the standard shape at 120 km altitude with a solar panel area of 15 m^2 with respect to 23 m^2 is a reduction of $\pm16\%$, assuming that the shape of the wings is similar as the ones presented in this thesis.

13.3 Influence of mission design choices on wind sensitivity

The satellite will encounter wind during its orbit through the lower thermosphere. Wind can increase the drag on the satellite. The conclusions made on the influence of the wind on the aerodynamic drag of the satellite are summarized here. In addition, the impact of the satellite mission design choices and satellite geometry design on the satellite's sensitivity to the wind are concluded.

One of the requirements flowing from the scientific objectives of Daedalus is to have a global coverage. This means that Daedalus will need to measure around all local solar times, latitudes and through geomagnetic storms. It can therefore be expected that the maximum horizontal wind from the models and data can be encountered by Daedalus from any direction in the horizontal plane.

Horizontal wind at 120 km and 300 km altitude

A data analysis has been performed in which in-situ horizontal wind data, originating from chemical tracers on board of sounding rockets and accelerometer data on board of GOCE have been compared to HWM14. In this data analysis it was found that the maximum horizontal wind from the models is much lower than the maximum horizontal wind from the data. The maximum winds from the [model,data] are [200, 370] m/s around an altitude of 120 km and [500, 1080] m/s around an altitude of 300 km. In addition it was found that 75% of the in-situ data showed a total wind of 100 m/s or lower at 120 km and 280 m/s or lower at 300 km. For the model this was 50 m/s and 150 m/s respectively. It was decided to look at the maximum winds to get an indication of the worst case scenario. The horizontal wind is decomposed in two directions, the cross-track direction of the wind, which is perpendicular to the velocity vector and within the horizontal plane and the in-track wind, which is, in the opposite direction as the velocity vector.

Cross-track wind influence on satellite body part design

The cross track wind results in a side-slip angle of the satellite shape with respect to the relative velocity of the satellite. It was found that for roll angles of 0°, the cross-track wind has most impact on the drag coefficient of the standard satellite's body part. However, this impact is very small and it was concluded that the cross-track wind has an insignificant influence (approximately 1%) on the total drag coefficient at the TF altitude. Comparing this to the results at the FMF altitude, the influence of the wind on the body and therefore the whole satellite, is slightly higher. This is due to the larger winds that occur at higher altitudes.

In case of no wind, it was found that drag could be reduced by increasing the length over area ratio of the body. When making the satellite more slender it was found that the body becomes more subjective to cross-track wind. For example, for the case that the body has twice the length and half the cross section, the frictional component is more subjective to wind than for the standard case. To quantify, the maximum wind found in the in-situ data, results in an increase of 0.2 m^2 in $C_D * A_{ref}$ of the slender body variation. This does not weigh up against the drag that was saved (0.9 m^2) by reducing the frontal area from the standard body to the slender body. So even though the satellite would become slightly more subjective to wind, much more drag would be saved by making the satellite slimmer and longer.

Cross-track wind influence on satellite solar array wing design

For the nominal satellite attitude with a roll angle of 0°, the wings of the satellite are aligned with the satellite velocity and therefore the impact of the worst-case cross-track wind on the satellite wings at 120 km was found to be negligible. When keeping the roll angle equal 0°, it has been concluded that the size and thickness of the wings have a negligible influence on satellite's aerodynamic sensitivity with respect to the wind.

However, for roll angles of 90°, the influence of the cross-track wind changes. Now, the wings are perpendicular to the cross-track wind, which results in a much larger affected area than for roll = 0°. The largest difference is therefore visible in the contribution of the wind on the wings. In the TF at 120 km altitude, the maximum wind from the in-situ data results in an increases of the total $C_D * A_{ref}$, equal to 8.2 m^2, by approximately 8.2%. The maximum wind from the model (HWM14) would have shown a 2.5% increase in the $C_D * A_{ref}$.

The values that describe the impact of the cross-track wind on the satellite are dependent on the size of the wings. Larger wings do not only increase the $C_D * A_{ref}$, as was mentioned in the previous section, but also increase the induced $C_D * A_{ref}$ due to the cross-track wind exponentially.

In addition, the errors in the model, based on the differences with the in-situ data, have most impact when the satellite is rolled with 90°. When the maximum modeled horizontal wind is taken into account for the solar panel wing design, the influence of the wind on the $C_D * A_{ref}$ would be in the range of [1.6, 3.2]% with respect to the $C_D * A_{ref}$ without wind depending on the wing size. From this it could be

concluded that the wind has a negligible effect on the $C_D * A_{ref}$ for various wingspans. However, the horizontal wind from the data would result in an increase of [5.2, 11.2]% with respect to the $C_D * A_{ref}$ in case of no wind for various wing sizes. Then, the wind shows a much more significant contribution to the drag and should not be neglected. This particular case shows that an underestimation of winds, by for example using the HWM14 model to obtain the winds, can have a significant impact on the Daedalus mission.

The thickness of the wings does not influence the sensitivity of the satellite to the wind. The thickness just increases the $C_D * A_{ref}$ by the same factor as for the case of no wind at every wind induced side-slip angle.

When comparing the influence of the cross-track wind on the wings at the TF altitude to the FMF altitude, it was found that the wind has more influence on the $C_D * A_{ref}$ at higher altitudes due to the larger winds that occur there, but follow approximately the same trends as at the TF altitude. Due to the low density at high altitudes, the influence of the cross-track wind on the total drag in FMF is 4 orders of magnitude smaller.

In-track wind influence

The other horizontal wind component is the in-track wind. The in-track wind can either be in the same direction as the orbital velocity, the so-called tailwind, or in the opposite direction of the orbital velocity, the so-called head wind. Since the in-track wind does not induce an extra attitude angle of the satellite's body with respect to the relative velocity, it can be assumed that the wind is exactly aligned with the satellite velocity and shape. Therefore, the influence of the in-track wind only need to be tested for the nominal satellite attitude with a roll angle of $0°$.

At the FMF altitude of 300 km, due to the large winds, a decrease in the $C_D * A_{ref}$ can be found for an increase of head wind. This is due to the fact that the relative velocity of the satellite with respect to the flow increases and therefore the frictional component along the sides of the satellite decreases.

At the TF altitude of 120 km, it was concluded that the winds are not large enough to find this relation in $C_D * A_{ref}$. The in-track wind does not have a significant influence on the drag coefficient of the satellite geometry in the TF at 120 km altitude. This conclusion is independent of the size of the body and the size and thickness of the wings as tested in this thesis.

When looking at the drag equation, the in-track wind does not only impact the relative velocity when obtaining the drag coefficients, but also influences relative velocity in the drag equation directly. In terms of drag, it can be expected that the in-track wind enforces satellite shapes with already a higher $C_D * A_{ref}$ or at a higher density. This was substantiated from the findings in this thesis. The head wind obtained from the in-situ data in the TF can result in a 10% increase in the drag. When the drag is already large due to a large $C_D * A_{ref}$ or density, the increase in the actual drag is also large. In the case of tail wind, the same reasoning applies, though in opposite direction as the drag is decreased with increasing wind. In that case the drag is decreased with increasing wind. It can be expected that for the complete mission lifetime, the head wind and tail wind effects balance out. Therefore, when looking at the complete mission duration, these forces cancel out. However, when looking at one orbit, it is important to take it into consideration.

Influence on the E-field booms

Through the report, the influence of the booms have been tested. Throughout all the cases, the value of $C_D * A_{ref}$ for the E-field booms stayed approximately the same. The largest variation was in the order of 0.1 m^2, which is small with respect to the total $C_D * A_{ref}$ of 8.2 m^2 or more. This means that the booms are not subjective to attitude, thermospheric condition variation nor wind. This can be explained by the configuration and size of the booms. For the booms to fulfill their scientific requirements they have be able to measure in all directions. In addition, the booms are extremely thin and long. This results in an almost constant value for $C_D * A_{ref}$ independent of the attitude, wind and thermospheric variability.

13.4 Recommendations

Finally, what recommendations can be given for the mission design based on the conclusions of this thesis? First of all, recommendations are given on how to simplify the design process of a mission through the lower thermosphere. Secondly, drag reduction considerations are presented. This conclusion is completed by giving some recommendations about research subjects that still need to be discussed in this topic.

13.4.1 Mission design simplification

Designing a mission that will orbit such a complex and variable region of the thermosphere is extremely difficult. It is therefore vital to make certain assumptions to simplify the process of mission design. From this thesis, certain recommendations for simplifications can be made based on what parameters have an insignificant or small influence on the satellite design. It is important to note, that the Daedalus design as proposed in ESA [2020], is slightly smaller, with possible slightly smaller wings, than the standard satellite shape used in this thesis. The influence that this difference in satellite geometry can have on the respective recommendation will also be discussed.

First of all, it was found that the apogee altitude difference between 2200 km and 2700 km has a negligible influence (less than 1%) on the aerodynamic drag. In order to compare for a smaller body and smaller wings, like the Daedalus geometry, the conclusions from the wing and body variations of the in-track wind can be used. The change in apogee altitude from 2200 to 2700 km results in a difference in satellite velocity at the perigee of 100 m/s. In case of no wind, this increases the relative velocity of the satellite at the perigee altitude with respect to the surrounding gas by 100 m/s. It was found, that for a satellite with a smaller body or slightly smaller wings, the sensitivity of the aerodynamic coefficients and the drag with a relative velocity increase of 100 m/s, does not increase. Which means that the simplification would still hold for a satellite like proposed for Daedalus. It is important to note however, that the apogee altitude should still be taken into account for the semi-major axis decay calculation.

Next, it can be assumed that the contribution of the booms to the total drag coefficient stays constant, independent of the attitude variations with respect to the flow (α, β, roll), the thermospheric parameter variations, and the relative velocity range, as tested in this thesis in terms of wind. It would therefore be possible to once calculate or simulate the contribution of the booms in a certain flow and then keep that value constant.

One of the most important recommendations in terms of simplification is that,when the satellite is rolled in such a way that its wings are aligned with the relative flow around the satellite, for the altitudes below 150 km, the worst-case cross-track winds have an insignificant influence on the $C_D * A_{ref}$ and therefore on the drag. This conclusion is independent of the wing size, wing thickness and body length over diameter ratio. In addition, it was found that the in-track wind has an insignificant impact on the drag coefficient too at 120 km altitude. Therefore, when the satellite is rolled 0°, the calculation of $C_D * A_{ref}$ at low altitudes can be simplified by not taking into account the wind. This means that also the difference between horizontal wind from the model and in-situ data has an insignificant influence on the drag. However, the in-track wind does influence the drag due to its relative velocity change, therefore the change in relative velocity due to the in-track wind should still be taken into account.

13.4.2 Drag reduction considerations

In order to minimize the decay of the satellite orbit with a perigee altitude around 120-140 km, the drag, which is mostly encountered at altitudes lower than 200 km, should be minimized. In this section some recommendations are given based on the conclusions of this thesis on how to save drag for a mission like Daedalus.

First of all, in terms of the body part shape, drag can be saved by making the body longer and thinner. It was found that by making the body twice as long and twice as thin, the drag coefficient times the

reference area, $C_D * A_{ref}$, and therefore the drag, was reduced by 0.8 m^2, for the body this is a reduction in $C_D * A_{ref}$ of 30%. For the $C_D * A_{ref}$ of the total satellite this is approximately 10%. It should be noted, that the satellite will respectively become more sensitive to cross-track wind when the length over diameter increases. It was found that the increase in $C_D * A_{ref}$ due to the enhanced sensitivity to the wind is negligible with respect to how much the change in geometry saves. It is expected that the payload bring forth the minimum constraint for the cross-sectional area.

Secondly, the wings are a huge source for drag. The size of the wings should be optimized by how much energy is needed and how much drag they generate. In the scope of Daedalus, $\pm16\%$ of $C_D * A_{ref}$ can be saved by the taking the lowest value of the expected solar panel area range of 15 - 23 m^2 with respect to the upper value. In addition, the horizontal wind can have a significant impact on the drag of the wings when rolling the satellite around its x-axis. Rolling the satellite during its mission is vital to position its solar array wings with respect to the Sun in order to obtain enough solar energy. However, rolling the satellite increases the affected area in $C_D * A_{ref}$ for the cross-track wind. By rolling the satellite back around the perigee altitude, the satellite can save up to 5-11% of the drag coefficient caused by the worst-case cross-track wind, depending on the wing area. For the estimated wing area range of Daedalus, this value is 7-8.5%. Saving drag at the perigee is important, since at the perigee the density is relatively high. In addition, large winds, during for example a geomagnetic storm, are often paired with even higher densities, such that more drag is exerted on the satellite. An increase in drag coefficient due to the wind increases that drag per percent wise. To minimize the drag, it is therefore favorable to have a low drag coefficient for high densities and during geomagnetic storms at high latitudes. It was found that an increase in the drag at these altitudes of 10% could increase the orbital decay with 10 %. In addition, not only the drag due to wind decreases, but it decreases so significantly that the cross-track wind does not need to be taken into account anymore. This will simplify the design.

To know more about drag reduction through shape optimisation for very Low Earth Orbiting satellites, the interested reader can refer to Walsh et al. [2021]. The focus of that research was to test many different shapes to optimize for the drag reduction.

13.4.3 Future research

In this section, some topics for future research are proposed. These topics have not been included in this thesis, or were only explained briefly, since they were out of the scope of the focus of this research. However, they are important for the topic of aerodynamics of a satellite flying through the TF.

Attitude stability

The satellite is not only influenced by the forces due to the wind in terms of drag and lift, but the wind also exerts moments and therefore torques on the satellite shape. The stability of the satellite depends on these torques. A satellite should generally be stable in order to fulfill its scientific requirements. The degree of stability needed depends on the scientific objective. The aerodynamic torque is a function of atmospheric density, the relative velocity vector of the satellite with respect to the thermospheric wind, the drag coefficient, reference area, and the moment arm between the center of pressure and the center of mass [Rawashdeh et al., 2009].

The wind influences the torque by changing the relative attitude of the satellite, the relative velocity, the drag coefficient and the reference area. It is expected that the torques increase with decreasing altitude due to the increase of density.

The aerodynamic torques are not the only torques exerted on the satellite. For GOCE for example, the total torque consists of magnetic torques, aerodynamic torques, gravity gradient torque, solar radiation pressure torque, Earth's albedo torque and the torque due to the misalignment of the ion thrusters Visser [2019]. Which of these torques is the dominant torque and in what direction the torques have the largest impact depends partly on the shape of the satellite. As an example, for GOCE, the aerodynamic torques were the dominant torques and its effects were especially clear in yaw direction, in this thesis

defined by side-slip angle Visser [2019].

Since 120 km is well below the orbital altitude of GOCE (around 270 km), it can be expected that the aerodynamic torques have an even greater influence on a satellite like Daedalus. To give a first hand estimation of the torques, the distance between the center of pressure distance and the center of mass can be investigated. In the case of the standard satellite model presented in this thesis, it can be expected that the center of mass is at the middle of the y and z axis, due to the symmetry of the shape. The center of mass of the body and the booms are as well in the middle of the x-axis due to symmetry, however the center of mass of the wings is a little behind due to the wing shapes. In Figure 13.1 the results of the center of pressure with respect to the center of gravity are given for a change in side-slip angle and in Figure 13.2 for a change in angle of attack.

A satellite is stable when a rotation of the satellite around the z-axis in the positive direction, results in a torque around the z-axis in the negative direction which forces the satellite to rotate back. This is visible for the side-slip, β, rotation in Figure 13.1, as well as the angle of attack, α, rotation in Figure 13.2. In Figure 13.1, it can be seen that if the satellite turns with its nose in the negative y-direction that the center of pressure is on the right side of the satellite. The force will then act in this point and push the satellite back to its original position. The same can be seen for the angle of attack in Figure 13.2. Also the magnitude of the torque is important, to see which torque is the dominant torque and in which direction the satellite is most stable. This is a preliminary analysis of this topic and the influence that various shapes and wind have on the stability of the satellite, should be investigated more thoroughly.
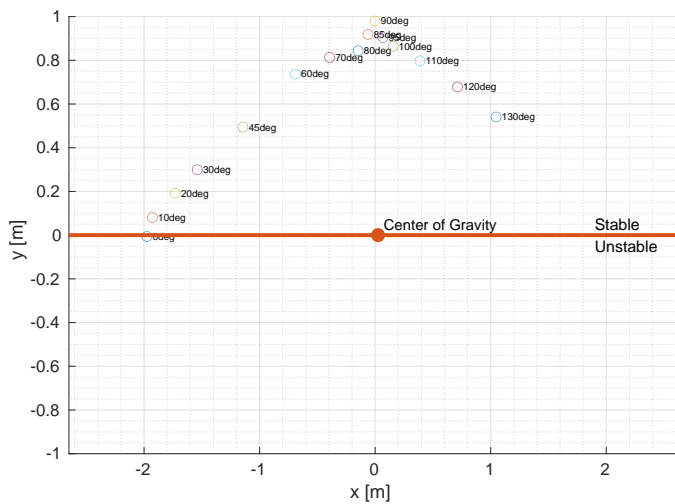
(a) With respect to side-slip angles range $[0,130]°$.
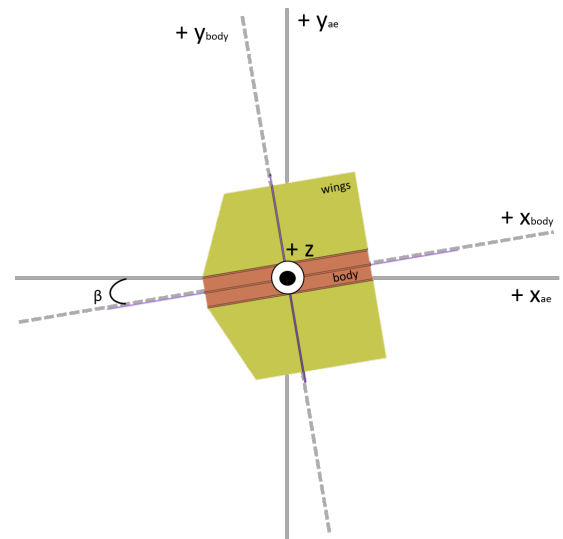
(b) Image of turning the satellite with a side-slip angle

Figure 13.1: Center of pressure with respect to side-slip angle.

(a) With respect to angles of attack range $[0,130]°$.

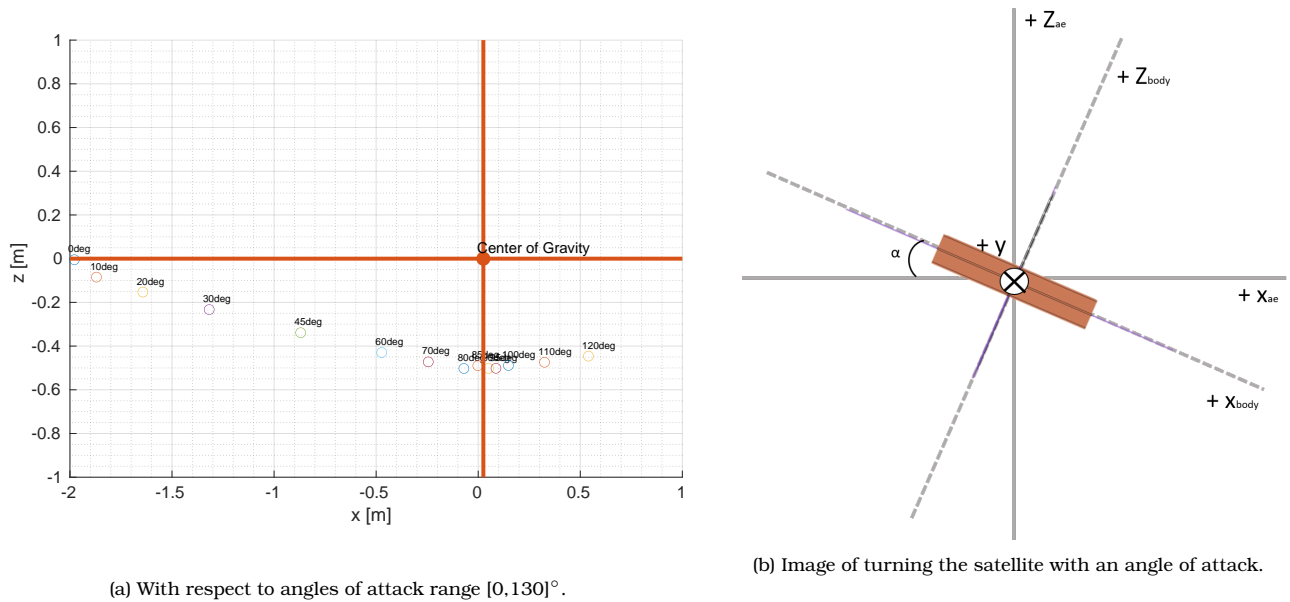(b) Image of turning the satellite with an angle of attack.

Figure 13.2: Center of pressure with respect to side-slip angle and angle of attack.

Vertical winds

In this thesis, the focus has been on the influence of the horizontal winds. However, from chapter 4, it was found that the horizontal winds are paired with vertical winds. From Visser et al. [2019b], it was found from comparing data sets of Explorer satellites and GOCE that the maximum magnitudes of the vertical winds were in the order of 50 m/s. This is much smaller than the magnitude for the horizontal wind that were taken into account in this thesis. The vertical winds have a similar influence on the satellite as the horizontal cross-track wind. Instead of inducing a side-slip angle, the vertical wind induces an angle of attack of the satellite velocity with respect to the atmosphere. In essence, a satellite rolled 0° with an angle of attack is the same as a satellite rolled 90° with a side-slip angle. A maximum wind magnitude of 50 m/s, would result in an angle of attack of approximately 0.35°. The influence in the orbital direction is therefore negligible. Nevertheless, it could be measured by the measurements of the accelerometer in the z-direction of the satellite orbital reference frame. The influence that a vertical acceleration has on the satellite in terms of torques and stability is an interesting topic and should be researched for the design of a mission like Daedalus.

Energy accommodation coefficient

The energy accommodation coefficient describes the reflection of the incoming particles with the surface. In this thesis, the energy accommodation coefficient has been assumed to be equal to 1 for all the cases, which corresponds to a total diffuse reflection. This was based on the assumption that at low altitudes the satellite surfaces are coated with absorbed atomic oxygen. Because of this, the incoming particles are re-emitted in a diffuse direction [Moe and Moe, 2005]. Furthermore, a sensitivity analysis, with energy accommodation coefficients varying between 0.8 and 1, was performed for the standard case at the attitude angles equal to 0°. It was found that the contribution of the frictional and pressure component of the drag coefficient interchanges with changing energy coefficient and balance out. As a result, the total change in drag coefficient is small. March et al. [2019] stated that the energy accommodation coefficient does have a significant influence on the satellite dynamics for satellites flying at an altitude of 300 km or higher and that the energy accommodation coefficient needs to be slightly smaller than 1 in order to give better results.

For a satellite like Daedalus, it would be useful to perform a more thorough analysis of the influence

of the uncertainty in the energy accommodation coefficient for multiple different attitudes. When the energy accommodation is less than 1, practically this means that the reflection of the particles on the surface becomes less diffusive and more specular. When the particle reflection is more specular, the orientation of the satellite surface with respect to the incoming particles becomes more important as well. For example, if the frontal surface is round or straight also matters. Testing various shapes, attitudes and accommodation coefficients can be a thesis by itself and was therefore out of the scope of this research.

Wing size

An interesting finding in this thesis was the big impact of the satellite wings on the drag coefficient. The large wings of the standard satellite geometry increase the frictional component of the total drag coefficient significantly. It was found that the large wing size made the drag coefficient of the satellite much more sensitive to the density, temperature and composition. An example of this is given in Figure 13.3. For two satellite shape geometries which varied in wing size, the drag coefficient with respect to the density is simulated. The standard satellite geometry, with a single wingspan of 2.5 m is compared to a similar geometry with a single wingspan of 0.7 m. It is found that the $C_D * A_{ref}$ of the large wing model increases with 2.5 m^2 in the TF, whereas the case with the small wings increases less than 0.9 m^2.

A big dependency of the drag coefficient with respect to the values of the thermospheric conditions is not favorable, because these conditions are highly variable. In addition, for high densities a lower $C_D * A_{ref}$ is most preferable to minimize the drag. It would therefore be interesting to further investigate what the impact is of the wing size and shape on the sensitivity of the satellite with respect to the thermospheric parameters and what the effect of this is on the mission.
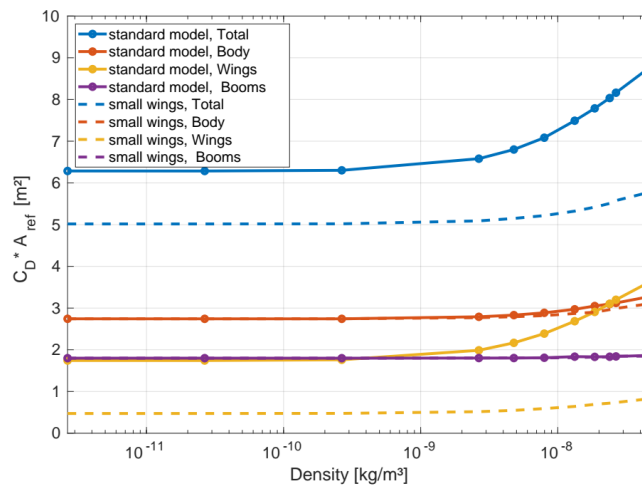

Figure 13.3: Density variation influence on the drag coefficient for satellite shape with small wings (span = 0.7 m) and the standard case (span = 2.5 m).

Bibliography

A. L. Aruliah and D. Rees. The trouble with thermospheric vertical winds: geomagnetic, seasonal and solar cycle dependence at high latitudes. *Journal of Atmospheric and Terrestrial Physics*, 57(6):597–609, 1995. ISSN 00219169. doi: 10.1016/0021-9169(94)00100-3.

X. Cai, T. Yuan, and L. Han-Li. Large-scale gravity wave perturbations in the mesopause region above Northern Hemisphere midlatitudes during autumnal equinox: A joint study by the USU Na lidar and Whole Atmosphere Community Climate Model. *Annales Geophysicae*, 35(2):181, 2017. ISSN 14320576. doi: 10.5194/angeo-35-181-2017.

T. D. Clark, J. Schoendorf, and A. D. Aylward. Modelling the effects of thermospheric winds on satellite orbits. *Environment Modeling for Space-Based Applications*, 392:299, 1996. ISSN 03796566.

H. D. Curtis. *Orbital Mechanics for Engineering Students*. 2013. ISBN 9780080977478. doi: 10.1016/C2011-0-69685-1.

E. Doornbos. *Thermospheric Density and Wind Determination from Satellite Dynamics*. Springer Science & Business Media, 2012. ISBN 3642251285. doi: 10.1007/978-3-642-25129-0. URL https://books.google.com/books?id=PQ4OUeD2cB0C&pgis=1.

E. Doornbos and H. Klinkrad. Modelling of space weather effects on satellite drag. *Advances in Space Research*, 37(6):1229–1239, 2006. ISSN 02731177. doi: 10.1016/j.asr.2005.04.097.

E. Doornbos, J. Van Den IJssel, H. Lühr, M. Förster, and G. Koppenwallner. Neutral density and cross-wind determination from arbitrarily oriented multiaxis accelerometers on satellites. *Journal of Spacecraft and Rockets*, 47(4):580–589, 2010. ISSN 00224650. doi: 10.2514/1.48114.

M. R. Drinkwater, R. Floberghagen, R. Haagmans, D. Muzi, and A. Popescu. GOCE: ESA's first Earth Explorer Core mission. Technical report, European Space Agency, ESTEC, Noordwijk, The Netherlands, 11 2003. URL http://www.esa.int/livingplanet.

D. P. Drob, J. T. Emmert, J. W. Meriwether, J. J. Makela, E. Doornbos, M. Conde, G. Hernandez, J. Noto, K. A. Zawdie, S. E. McDonald, J. D. Huba, and J. H. Klenzing. An update to the Horizontal Wind Model (HWM): The quiet time thermosphere. *Earth and Space Science*, 2(7):301–319, 2015. ISSN 23335084. doi: 10.1002/2014EA000089.

E. Mooij. *Re-entry Systems, Lecture Notes (2019-2020)*. Faculty of Aerospace Engineering, TU Delft, Delft, 2019.

ESA. Report for Assessment: Earth Explorer 10 Candidate Mission Daedalus. Technical report, European Space Agency, Noordwijk, The Netherlands, 11 2020.

J. M. Forbes. Dynamics of the Thermosphere. *Journal of the Meteorological Society of Japan. Ser II*, 85: 193–213, 2007. ISSN 0026-1165. doi: http://doi.org/10.2151/jmsj.85B.193.

J. M. Forbes and H. B. Garrett. Solar diurnal tide in the thermosphere. *Journal of the Atmospheric Sciences*, 33(11):2226–2241, 1976. ISSN 00224928. doi: 10.1175/1520-0469(1976)033<2226: SDTITT>2.0.CO;2.

J. M. Forbes, R. G. Roble, and C. G. Fesen. Acceleration, heating, and compositional mixing of the thermosphere due to upward propagating tides. *Journal of Geophysical Research: Space Physics*, 98 (A1):311–321, 1 1993. ISSN 0148-0227. doi: 10.1029/92ja00442.

J. M. Forbes, M. E. Hagan, S. Miyahara, Y. Miyoshi, and X. Zhang. Diurnal nonmigrating tides in the tropical lower thermosphere. *Earth, Planets and Space*, 55(7):419–426, 2003. ISSN 18805981. doi: 10.1186/BF03351775.

A. C. Fraser-Smith. Spectrum of the geomagnetic activity index Ap . *Journal of Geophysical Research*, 77(22):4209–4220, 8 1972. doi: 10.1029/ja077i022p04209. URL https://agupubs.onlinelibrary. wiley.com/doi/full/10.1029/JA077i022p04209https://agupubs.onlinelibrary.wiley.com/doi/abs/10. 1029/JA077i022p04209https://agupubs.onlinelibrary.wiley.com/doi/10.1029/JA077i022p04209.

J. Geul, E. Mooij, and R. Noomen. GOCE STATISTICAL RE-ENTRY PREDICTIONS. In *7th European Conference on Space Debris*, Delft, 4 2017.

J. Guo, W. Wan, J. M. Forbes, E. Sutton, R. S. Nerem, T. N. Woods, S. Bruinsma, and L. Liu. Effects of solar variability on thermosphere density from CHAMP accelerometer data. *Journal of Geophysical Research: Space Physics*, 112(A10), 2007. ISSN 21699402. doi: 10.1029/2007JA012409.

D. M. Hamby. A review of techniques for parameter sensitivity analysis of environmental models. *Environmental Monitoring and Assessment*, 32(2):135–154, 9 1994. ISSN 01676369. doi: 10.1007/BF00547132. URL https://link.springer.com/article/10.1007/BF00547132.

A. D. Hands, K. A. Ryden, N. P. Meredith, S. A. Glauert, and R. B. Horne. Radiation Effects on Satellites During Extreme Space Weather Events. *Space Weather*, 16(9):1216–1226, 2018. ISSN 15427390. doi: 10.1029/2018SW001913.

A. E. Hedin, B. B. Hinton, and G. A. Schmitt. Role of gas-surface interactions in the reduction of Ogo 6 neutral particle mass spectrometer data. *Journal of Geophysical Research*, 78(22):4651–4668, 8 1973. doi: 10.1029/ja078i022p04651. URL https://agupubs.onlinelibrary.wiley.com/doi/full/10.1029/ JA078i022p04651https://agupubs.onlinelibrary.wiley.com/doi/abs/10.1029/JA078i022p04651https: //agupubs.onlinelibrary.wiley.com/doi/10.1029/JA078i022p04651.

T. J. Immel, S. L. England, S. B. Mende, R. A. Heelis, C. R. Englert, J. Edelstein, H. U. Frey, E. J. Korpela, E. R. Taylor, W. W. Craig, S. E. Harris, M. Bester, G. S. Bust, G. Crowley, J. M. Forbes, J. C. Gérard, J. M. Harlander, J. D. Huba, B. Hubert, F. Kamalabadi, J. J. Makela, A. I. Maute, R. R. Meier, C. Raftery, P. Rochus, O. H. Siegmund, A. W. Stephan, G. R. Swenson, S. Frey, D. L. Hysell, A. Saito, K. A. Rider, and M. M. Sirk. The Ionospheric Connection Explorer Mission: Mission Goals and Design. *Space Science Reviews*, 214(1):13, 2018. ISSN 15729672. doi: 10.1007/s11214-017-0449-2.

M. Z. Jacobson. Fundamentals of atmospheric modeling second edition. In *Fundamentals of Atmospheric Modeling Second Edition*, chapter 2. Cambridge University Press, New York, 2 edition, 2005. ISBN 9781139165389. doi: 10.1017/CBO9781139165389.

M. Jones, J. M. Forbes, and F. Sassi. The Effects of Vertically Propagating Tides on the Mean Dynamical Structure of the Lower Thermosphere. *Journal of Geophysical Research: Space Physics*, 124(8):7202–7219, 8 2019. ISSN 21699402. doi: 10.1029/2019JA026934. URL https://onlinelibrary.wiley. com/doi/abs/10.1029/2019JA026934.

D. G. King-Hele and D. M. C. Walker. The effect of air drag on satellite orbits: Advances in 1687 and 1987. *Vistas in Astronomy*, 30(PART 3):269–289, 1 1987. ISSN 00836656. doi: 10.1016/0083-6656(87) 90006-7.

H. Klinkrad, B. Fritsche, T. Lips, and G. Koppenwallner. Re-Entry Prediction and On-Ground Risk Estimation. In *Space Debris*, pages 241–288. Springer Berlin Heidelberg, 2006. doi: 10.1007/3-540-37674-7-9. URL `http://link.springer.com/10.1007/3-540-37674-7_9`.

G. Koppenwallner. Energy accommodation coefficient and momentum transfer modeling. *Hyperschall Technologie Göttingen GmbH TN-08-11, Katlenburg Lindau, Germany*, 2009.

K. Koura and H. Matsumoto. Variable soft sphere molecular model for air species. *Physics of Fluids A*, 4(5):1083–1085, 5 1992. ISSN 08998213. doi: 10.1063/1.858262. URL `http://aip.scitation.org/doi/10.1063/1.858262`.

M. F. Larsen. Coqui 2: Mesospheric and lower thermospheric wind observations over Puerto Rico. *Geophysical Research Letters*, 27(4):445–448, 2000. ISSN 00948276. doi: 10.1029/1999GL010704.

M. F. Larsen. Winds and shears in the mesosphere and lower thermosphere: Results from four decades of chemical release wind measurements. *Journal of Geophysical Research: Space Physics*, 107(A8): 28–1, 2002. ISSN 21699402. doi: 10.1029/2001JA000218.

M. F. Larsen, A. B. Christensen, and C. D. Odom. Observations of unstable atmospheric shear layers in the lower E region in the post-midnight auroral oval. *Geophysical Research Letters*, 24(15):1915–1918, 1997. ISSN 00948276. doi: 10.1029/97GL01942.

M. F. Larsen, S. Fukao, M. Yamamoto, R. Tsunoda, K. Igarashi, and T. Ono. The SEEK Chemical Release Experiment: Observed neutral wind profile in a region of sporadic E. *Geophysical Research Letters*, 25(22):1789–1792, 1998. ISSN 0094-8276. doi: 10.1029/98gl00986.

M. F. Larsen, A. Z. Liu, R. L. Bishop, and J. H. Hecht. TOMEX: A comparison of lidar and sounding rocket chemical tracer wind measurements. *Geophysical Research Letters*, 30(7):3–6, 2003. ISSN 00948276. doi: 10.1029/2002GL015678.

J. Laštovička. Trends in the upper atmosphere and ionosphere: Recent progress. *Journal of Geophysical Research: Space Physics*, 118(6):3924–3935, 5 2013. ISSN 21699402. doi: 10.1002/jgra.50341. URL `http://doi.wiley.com/10.1002/jgra.50341`.

H. Liu and H. Lühr. Strong disturbance of the upper thermospheric density due to magnetic storms: CHAMP observations. *Journal of Geophysical Research: Space Physics*, 110(A9), 2005. ISSN 21699402. doi: 10.1029/2004JA010908.

D. H. Mac Manus, C. J. Rodger, M. Dalzell, A. W. Thomson, M. A. Clilverd, T. Petersen, M. M. Wolf, N. R. Thomson, and T. Divett. Long-term geomagnetically induced current observations in New Zealand: Earth return corrections and geomagnetic field driver. *Space Weather*, 15(8):1020–1038, 2017. ISSN 15427390. doi: 10.1002/2017SW001635.

G. March, E. N. Doornbos, and P. N. Visser. High-fidelity geometry models for improving the consistency of CHAMP, GRACE, GOCE and Swarm thermospheric density data sets. *Advances in Space Research*, 63(1):213–238, 1 2019. ISSN 18791948. doi: 10.1016/j.asr.2018.07.009. URL `https://doi.org/10.1016/j.asr.2018.07.009`.

F. A. Marcos and J. M. Forbes. Thermospheric winds from the satellite electrostatic triaxial accelerometer system. *Journal of Geophysical Research*, 90(A7):6543–6552, 1985. ISSN 0148-0227. doi: 10.1029/ja090ia07p06543.

A. Marín, I. B. Sebastiaõ, S. Tamrazian, D. Spencer, and A. Alexeenko. DSMC-SPARTA aerodynamic characterization of a deorbiting CubeSat. *AIP Conference Proceedings*, 2132(August):070024, 8 2019. ISSN 15517616. doi: 10.1063/1.5119578. URL `http://aip.scitation.org/doi/abs/10.1063/1.5119578`.

J. Marshall and R. A. Plumb. *Atmosphere, Ocean, and Climate Dynamics*. 2008. ISBN 9780125586917. doi: 10.1017/CBO9781107415324.004.

P. M. Mehta, A. Walker, C. A. McLaughlin, and J. Koller. Comparing physical drag coefficients computed using different gas-surface interaction models. *Journal of Spacecraft and Rockets*, 51(3):873–883, 2014. ISSN 15336794. doi: 10.2514/1.A32566.

P. M. Mehta, E. Minisci, M. Vasile, A. C. Walker, and M. Brown. An Open-source Hypersonic Aerodynamic And Aerothermodynamic Modeling Tool. *8th European Symposium on Aerothermodynamics for Space Vehicles*, (1):9, 2015.

K. Moe and M. M. Moe. Gas-surface interactions and satellite drag coefficients. *Planetary and Space Science*, 53(8):793–801, 2005. ISSN 00320633. doi: 10.1016/j.pss.2005.03.005.

M. M. Moe and K. Moe. The roles of kinetic theory and gas-surface interactions in measurements of upper-atmospheric density. *Planetary and Space Science*, 17(5):917–922, 5 1969. ISSN 00320633. doi: 10.1016/0032-0633(69)90097-X.

O. Montenbruck and E. Gill. *Satellite Orbits: Models, Methods, and Applications*, volume 55. Springer, 2 edition, 3 2002. doi: 10.1115/1.1451162.

W. J. Morokoff and A. Kersch. A comparison of scattering angle models. *Computers and Mathematics with Applications*, 35(1-2):155–164, 1 1998. ISSN 08981221. doi: 10.1016/s0898-1221(97)00265-4.

D. Müller, R. G. Marsden, O. C. St. Cyr, and H. R. Gilbert. Solar Orbiter: Exploring the Sun-Heliosphere Connection. *Solar Physics*, 285(1-2):25–70, 7 2013. ISSN 00380938. doi: 10.1007/s11207-012-0085-7.

S. Müller, H. Lühr, and S. Rentz. Solar and magnetospheric forcing of the low latitude thermospheric mass density as observed by CHAMP. *Annales Geophysicae*, 27(5):2087–2099, 2009. ISSN 09927689. doi: 10.5194/angeo-27-2087-2009.

D. Offermann and K. U. Grossmann. Thermospheric density and composition as determined by a mass spectrometer with cryo ion source. *Journal of Geophysical Research*, 78(34):8296–8304, 12 1973. doi: 10.1029/ja078i034p08296. URL `https://agupubs.onlinelibrary.wiley.com/doi/full/10.1029/JA078i034p08296`.

X. Pi, B. A. Iijima, and W. Lu. Effects of Ionospheric Scintillation on GNSS-Based Positioning. *Navigation, Journal of the Institute of Navigation*, 64(1):3–22, 2017. ISSN 00281522. doi: 10.1002/navi.182.

J. M. Picone, A. E. Hedin, D. P. Drob, and A. C. Aikin. NRLMSISE-00 empirical model of the atmosphere: Statistical comparisons and scientific issues. *Journal of Geophysical Research: Space Physics*, 107 (A12):1–16, 2002. ISSN 21699402. doi: 10.1029/2002JA009430.

J. M. Picone, J. T. Emmert, and J. L. Lean. Thermospheric densities derived from spacecraft orbits: Accurate processing of two-line element sets. *Journal of Geophysical Research: Space Physics*, 110 (A3):1–19, 2005. ISSN 21699402. doi: 10.1029/2004JA010585.

M. D. Pilinski, B. M. Argrow, and S. E. Palo. Semiempirical model for satellite energy-accommodation coefficients. *Journal of Spacecraft and Rockets*, 47(6):951–956, 2010. ISSN 15336794. doi: 10.2514/1.49330.

M. D. Pilinski, R. L. McNally, B. A. Bowman, S. E. Palo, J. M. Forbes, B. L. Davis, R. G. Moore, K. Kemble, C. Koehler, and B. Sanders. Comparative Analysis of Satellite Aerodynamics and Its Application to Space-Object Identification. *Journal of Spacecraft and Rockets*, 53(5):876–886, 9 2016. ISSN 0022-4650. doi: 10.2514/1.A33482. URL `https://arc.aiaa.org/doi/10.2514/1.A33482`.

A. Pulkkinen, E. Bernabeu, A. Thomson, A. Viljanen, R. Pirjola, D. Boteler, J. Eichner, P. J. Cilliers, D. Welling, N. P. Savani, R. S. Weigel, J. J. Love, C. Balch, C. M. Ngwira, G. Crowley, A. Schultz, R. Kataoka, B. Anderson, D. Fugate, J. J. Simpson, and M. MacAlester. Geomagnetically induced currents: Science, engineering, and applications readiness. *Space Weather*, 15(7):828–856, 2017. ISSN 15427390. doi: 10.1002/2016SW001501.

S. Rawashdeh, D. Jones, D. Erb, A. Karam, and J. E. Lumpp. Aerodynamic attitude stabilization for a ram-facing CubeSat. *Advances in the Astronautical Sciences*, 133(1):583–595, 2009. ISSN 00653438.

F. J. Regan and S. M. Anandakrishnan. *Dynamics of Atmospheric Re-Entry*. American Institute of Aeronautics and Astronautics, 2 edition, 1 1993. doi: 10.2514/4.861741.

A. D. Richmond, E. C. Ridley, and R. G. Roble. A thermosphere/ionosphere general circulation model with coupled electrodynamics. *Geophysical Research Letters*, 19(6):601–604, 3 1992. ISSN 19448007. doi: 10.1029/92GL00401. URL http://doi.wiley.com/10.1029/92GL00401.

A. J. Ridley, Y. Deng, and G. Tóth. The global ionosphere-thermosphere model. *Journal of Atmospheric and Solar-Terrestrial Physics*, 68(8):839–864, 2006. ISSN 13646826. doi: 10.1016/j.jastp.2006.01.008.

H. Rishbeth and R. G. Roble. Cooling of the upper atmosphere by enhanced greenhouse gases - modelling of thermospheric and ionospheric effects. *Planetary and Space Science*, 40(7):1011–1026, 1992. ISSN 00320633. doi: 10.1016/0032-0633(92)90141-A.

J. E. Salah and J. M. Holt. Midlatitude thermospheric winds from incoherent scatter radar and theory. *Radio Science*, 9(2):301–313, 2 1974. ISSN 00486604. doi: 10.1029/RS009i002p00301. URL http://doi.wiley.com/10.1029/RS009i002p00301.

H. Saltsburg, J. N. Smith, and M. Rogers. Fundamentals of Gas–Surface Interactions. In H. Saltsburg, J. N. Smith, and M. Rogers, editors, *Fundamentals of Gas–Surface Interactions*, San Diego, California, 1967. Elsevier. ISBN 978-1-4832-2901-0. doi: 10.1016/c2013-0-12148-4.

T. E. Sarris, E. R. Talaat, M. Palmroth, I. Dandouras, E. Armandillo, G. Kervalishvili, S. Buchert, D. Malaspina, A. Jaynes, N. Paschalidis, J. Sample, J. Halekas, S. Tourgaidis, V. Lappas, M. Clilverd, Q. Wu, I. Sandberg, A. Aikio, and P. Pirnaris. Daedalus: A Low-Flying Spacecraft for the Exploration of the Lower Thermosphere - Ionosphere. *Geoscientific Instrumentation, Methods and Data Systems Discussions*, 3:1–19, 2019. ISSN 2193-0872. doi: 10.5194/gi-2019-3.

L. Sentman. Free Molecule Flow Theory and its Application to the Determination of Aerodynamic Forces, 1961.

G. G. Shepherd. WINDII, the wind imaging interferometer on the upper atmosphere research satellite. *Journal of Geophysical Research*, 98(D6), 1993. ISSN 01480227. doi: 10.1117/12.60599.

G. G. Shepherd, G. Thuillier, Y. M. Cho, M. L. Duboin, W. F. Evans, W. A. Gault, C. Hersom, D. J. Kendall, C. Lathuillre, R. P. Lowe, I. C. McDade, Y. J. Rochon, M. G. Shepherd, B. H. Solheim, D. Y. Wang, and W. E. Ward. The wind imaging interferometer (WINDII) on the upper atmosphere research satellite: A 20 year perspective. *Reviews of Geophysics*, 50(2), 6 2012. ISSN 87551209. doi: 10.1029/2012RG000390.

M. Sinnhuber, H. Nieder, and N. Wieters. Energetic Particle Precipitation and the Chemistry of the Mesosphere/Lower Thermosphere. *Surveys in Geophysics*, 33(6):1281–1334, 11 2012. ISSN 01693298. doi: 10.1007/s10712-012-9201-3.

S. C. Solomon, L. Qian, and R. G. Roble. New 3-D simulations of climate change in the thermosphere. *Journal of Geophysical Research: Space Physics*, 120(3):2183–2193, 3 2015. ISSN 21699402. doi: 10.1002/2014JA020886.

N. W. Spencer, H. B. Niemann, and G. R. Carignan. The neutral-atmosphere temperature instrument. *Radio Science*, 8(4):287–296, 4 1973. ISSN 00486604. doi: 10.1029/RS008i004p00287. URL http://doi.wiley.com/10.1029/RS008i004p00287.

E. K. Sutton, J. M. Forbes, and R. S. Nerem. Global thermospheric neutral density and wind response to the severe 2003 geomagnetic storms from CHAMP accelerometer data. *Journal of Geophysical Research: Space Physics*, 110(A9), 2005. ISSN 21699402. doi: 10.1029/2004JA010985.

L. M. Toonen. Analysis of lower thermosphere in-situ wind data for the ESA Daedalus mission feasibility studies. Technical report, Royal Netherlands Meteorological Institute (KNMI), De Bilt, 2020a.

L. M. Toonen. Modelling lower thermospheric wind and its influence on satellite dynamics. Technical report, TU Delft, Aerospace Engineering faculty, 2020b.

L. D. Trichtchenko, L. V. Nikitina, A. P. Trishchenko, and L. Garand. Highly Elliptical Orbits for Arctic observations: Assessment of ionizing radiation. *Advances in Space Research*, 54(11):2398–2414, 2014. ISSN 18791948. doi: 10.1016/j.asr.2014.09.012. URL `http://dx.doi.org/10.1016/j.asr.2014.09.012`.

D. Turse, L. Adams, and C. Esser. Deployment System for Three Axis CubeSat Electric Field Instrument. *Proceedings of the 42nd Aerospace Mechanisms Symposium*, pages 213–220, 2016.

T. Visser. *Dynamics, Cross-wind from linear and angular satellite Thermosphere, The GOCE perspective on horizontal and vertical wind in the thermosphere.* PhD thesis, Delft University of Technology., Delft, 2019.

T. Visser, G. March, E. Doornbos, C. de Visser, and P. Visser. Horizontal and vertical thermospheric cross-wind from GOCE linear and angular accelerations. *Advances in Space Research*, 63(10):3139–3153, 2019a. ISSN 18791948. doi: 10.1016/j.asr.2019.01.030.

T. Visser, G. March, E. N. Doornbos, C. de Visser, and P. N. Visser. Characterization of thermospheric vertical wind activity at 225-295 km altitude using GOCE data and validation against Explorer missions. *JGR: Space Physics*, 124(6), 2019b.

K. F. Wakker. *Fundamentals of Astrodynamics.* Institutional Repository Library, Delft, 2015. ISBN 978-94-6186-419-2. URL `http://resolver.tudelft.nl/uuid:3fc91471-8e47-4215-af43-718740e6694e`.

J. Walsh, L. Berthoud, and C. Allen. Drag reduction through shape optimisation for satellites in Very Low Earth Orbit. *Acta Astronautica*, 179:105–121, 2 2021. ISSN 00945765. doi: 10.1016/j.actaastro.2020.09.018.

C. Xiong, C. Stolle, and H. Lühr. The Swarm satellite loss of GPS signal and its relation to ionospheric plasma irregularities. *Space Weather*, 14(8):563–577, 2016. ISSN 15427390. doi: 10.1002/2016SW001439.

J. H. Zoennchen, U. Nass, H. J. Fahr, and J. Goldstein. The response of the H geocorona between 3 and 8 Re to geomagnetic disturbances studied using TWINS stereo Lyman-α data. *Annales Geophysicae*, 35(1):171–179, 2017. ISSN 14320576. doi: 10.5194/angeo-35-171-2017.